CHARACTERIZATION OF AU, AU/GO AND AU/RGO SURFACES FOR CAROTID ENDOTHELIAL CELL PROLIFERATION BY ELECTRICAL IMPEDANCE SPECTROSCOPY METHOD

by

Fatma Gülden Şimşek

B.S., in Physics, Boğaziçi University, 2008

M.S., in Biomedical Engineering, Boğaziçi University, 2010

Submitted to the Institute of Biomedical Engineering

in partial fulfillment of the requirements

for the degree of

Doctor

of

Philosophy

Boğaziçi University

2020

CHARACTERIZATION OF AU, AU/GO AND AU/RGO SURFACES FOR CAROTID ENDOTHELIAL CELL PROLIFERATION BY ELECTRICAL IMPEDANCE SPECTROSCOPY METHOD

APPROVED BY:

Assoc. Prof. Dr. Bora Garipcan .....
(Thesis Advisor)

Prof. Dr. Yekta Ülgen .....
(Thesis Co-advisor)

Assoc. Prof. Dr. Özgür Kocatürk .....

Assoc. Prof. Dr. Duygu Ege .....

Assist. Prof. Dr. Hakan Solmaz .....

Prof. Dr. Lokman Uzun .....

DATE OF APPROVAL: 30 June 2020

ACKNOWLEDGMENTS

I would like to express my gratitude and appreciation to my graduate supervisor Prof. Dr. Yekta Ülgen, for his valuable support and guidance throughout my graduate studies.

It was a pleasure for me that Assoc. Prof. Dr. Bora Garipcan was my supervisor. He was always very helpful and thoughtful.

I also thank Assoc. Prof. Dr. Özgür Kocatürk for his support and advices throughout my studies.

I am grateful Assoc. Prof. Dr. Duygu Ege, Assist. Prof. Dr. Hakan Solmaz, Prof. Dr. Lokman Uzun for their participance in my thesis committee.

I should also thank Prof. Dr. Burak Güçlü for his valuable answers to some of my questions about the data processing. I would like to thank Ayse Sena Sarp for her endless and precious support. She was always there when I needed. I also thank to my friends, Ahu Türkoğlu, Ahmet Atasoy, Ahmet Talaş, Alp Özgün, Bengü Aktaş, Bige Vardar, Bora Büyüksaraç, Burcu Tunç, Didar Talat, Elif Kubat, Esin Karahan, Fatma Zehra Erkoç, Gamze Ateş, Hayriye Öztatlı, Murat Tümer, Muhammed Avşar, Nermin Topaloğlu, Osman Melih Can, Özgen Öztürk, Öznur Demir, Seda Dumlu, Sabra Rosetami, Sezin Eren, Uluç Pamuk and all the other friends, we shared so many memories in BME. I am specially very thankful to my family; my mother, my father and my brothers for their encouragement during my life. I finally and mostly thank to my husband for his patience and support during my studies.

And my little daughter, Berra. I love you so much.

ACADEMIC ETHICS AND INTEGRITY STATEMENT

I, Fatma Gülden Şimşek, hereby certify that I am aware of the Academic Ethics and Integrity Policy issued by the Council of Higher Education (YÖK) and I fully acknowledge all the consequences due to its violation by plagiarism or any other way.

Name :

Signature:

Date:

ABSTRACT

CHARACTERIZATION OF AU, AU/GO AND AU/RGO SURFACES FOR CAROTID ENDOTHELIAL CELL PROLIFERATION BY ELECTRICAL IMPEDANCE SPECTROSCOPY METHOD

Endothelium dysfunction may be the cause of cardiovascular diseases such as heart attack, aneurysm, or atherosclerosis. Thus understanding endothelial cell properties helps explaining the reasons and treatment of cardiovascular diseases. Electrical impedance spectroscopy (EIS) is a real-time tool for evaluation of cell behavior. In this dissertation, human carotid artery endothelial cell (HCtAEC) proliferation on graphene derivatives was analyzed through EIS, optical images, Alamar Blue cell viability test and cell staining. Gold (Au) layers were deposited on glass surfaces by using photo-lithographic technique and plasma enhanced chemical vapor deposition. Graphene oxide (GO) was immobilized on Au electrodes through self-assembly monolayers (Au/GO). Hydrazine vapor reduction process was performed in order to obtain reduced graphene oxide (rGO) surfaces (Au/rGO). Au, Au/GO and Au/rGO surfaces were examined through SEM images and water contact angle measurements. These coatings were performed on the electrodes used in EIS analysis. EIS analysis (100 Hz-1 MHz) was performed for HCtAECs cultured on the Au, Au/GO Au/rGO electrodes for 10 days. Results showed that GO and rGO coatings did not prevent neither the electrical measurements nor the cell proliferation. rGO had a positive effect on HCtAEC proliferation. The rate of increase of impedance change from Day 1 to Day 10 was nearly five-fold for all electrode surfaces. Alamar Blue assay performed to monitor cell proliferation rates between groups, and rGO has shown the highest Alamar Blue reduction value of $43.65 \pm 8.79\%$. Acridine orange/propidium iodide (AO/PI) staining showed that cell viability on electrodes was similar to tissue culture plate.

Keywords: Graphene Oxide, Reduced Graphene Oxide, Electrical Impedance Spectroscopy, Human Carotid Artery Endothelial Cell, Endothelialization

ÖZET

İNSAN KAROTİD ARTER DAMARI ENDOTEL HÜCRELERİNİN AU, AU/GO VE AU/RGO YÜZEYLERİNDE ÇOĞALMASININ ELEKTRİKSEL EMPEDANS SPEKTROSKOPİSİ İLE KARAKTERİZASYONU

Endotel fonksiyon bozuklukları; kalp krizi, anevrizma, ateroskleroz gibi birçok kalp ve damar hastalıklarına yol açabilmaktedir. Bu nedenle endotel hücrelerin özelliklerini anlamak; kalp damar rahatsızlıklarının sebeplerini açıklamak ve tedavisini gerçekleştirmek için gereklidir. Elektriksel empedans spektroskopisi hücre davranışlarını değerlendirmekte kullanılan bir ölçüm metodudur. Bu tezde, insan karotid arter endotel hücrelerinin grafen türevleri üzerinde davranışları elektriksel empedans spektroskopisi, optik görüntüleme, hücre canlılık testi ve hücre boyama teknikleriyle incelenmiştir. Fotolitografi ve plazma destekli kimyasal buhar depozisyon ile cam yüzeylere altın kaplama yapılmıstır. Grafen oksit altın yüzeylere kendiliğinden bağlanma metodu ile bağlanmıştır. Hidrazin buharı grafen oksitlerin indirgenmesinde kullanılmıştır. Au, Au/GO and Au/rGO yüzeyleri taramalı elektron mikroskobu, suyun temas açısı ölcümü ve elektriksel empedans analizi yöntemleriyle değerlendirilmiştir. İnsan karotid arter endotel hücrelerinin on gün boyunca Au, Au/GO ve Au/rGO yüzey elektrotları üzerindeki çoğalması elektriksel empedans spektroskopisi ile ölçülmüştür. Sonuçlar, grafen oksit ve indirgenmiş grafen oksitin elektriksel ölçümlere ve hücre canlılığına altına göre engel oluşturmadığını göstermiştir. Au/rGO yüzeyinin olumlu etkisi gözlenmiştir. Bütün elektrot yüzeylerinde, birinci günden onuncu güne hücre çoğalmasıyla empedans degişimi yaklasık 5 kat artmıştır. Au/rGO yüzeyler, %43.65±8.79 ile en yüksek Alamar Blue indirgenme sonucu vermiştir. AO/PI boyama analizine göre üçüncü günde hücre canlılığı tüm yüzeylerde ideal hücre kültür ortamına benzemektedir.

Anahtar Sözcükler: Grafen Oksit, İndirgenmiş grafen oksit, Elektriksel Empedans Spektroskopisi, Insan Karotid Arter Endotel Hücresi

TABLE OF CONTENTS

ACKNOWLEDGMENTS iii
ACADEMIC ETHICS AND INTEGRITY STATEMENT iv
ABSTRACT v
ÖZET vi
LIST OF FIGURES ix
LIST OF TABLES xvii
LIST OF SYMBOLS xviii
LIST OF ABBREVIATIONS xix
1. INTRODUCTION AND THEORY 1
1.1 Motivation, aim and outline of the thesis 1
1.2 Endothelialization in Cardiovascular Diseases 2
1.3 Graphene 5
1.3.1 Synthesis of Graphene 7
1.3.2 Graphene and Graphene Related Materials in Endothelialization 8
1.4 Impedance Spectroscopy 9
1.4.1 Basics of Electrical Impedance Spectroscopy 10
1.4.2 Electrical Properties of Biological Tissues 12
1.4.3 Electrical Equivalent Models of Biological Tissue 14
1.5 Graphical Representation of EIS 18
2. DESIGN AND CHARACTERIZATION OF EIS SENSORS 19
2.1 The Sensor Design 19
2.2 SAM formation on Au surface, GO immobilization, and reduction of GO 22
2.3 Surface Characterization 24
2.3.1 Scanning Electron Microscopy 24
2.3.2 Water Contact Angle Analysis 27
2.3.3 EIS for Surface Characterization 29
2.4 The Validation of the EIS Sensor C 30
2.5 Preliminary Cell Culture Studies 33
2.6 Conclusion 35

3. ANALYSIS FOR HUMAN CAROTID ARTERY ENDOTHELIAL CELL PROLIFERATION ON ELECTRODE SURFACES 39
3.1 Materials and Method 39
3.1.1 Cell Culture 39
3.1.2 Electrical Impedance Measurements 39
3.1.3 Optical Images of HCAtECs on Au, Au/GO and Au/rGO electrodes 41
3.1.4 Alamar Blue (AB) cell viability assay 41
3.1.5 Immunostaining with 4', 6-diamidino-2-phenylindole (DAPI) and F-actin 41
3.1.6 Acridine Orange (AO) and Propidium Iodide (PI) Staining for Cell Viability 42
3.2 Results for HCtAECs Proliferation on Au, Au/GO and Au/rGO Surfaces 43
3.2.1 EIS Analysis Results 43
3.2.2 Cell counting 52
3.2.3 Cell Viability Assay 58
3.2.4 AO/PI Staining 59
3.2.5 Fluorescent staining for nuclei and F-actin visualization of HCtAECs 60
3.3 Discussion 61
4. CONCLUSION AND FUTURE WORK 67
APPENDIX A. EXAMINING GRAPHENE FLAKES FOR PROCESSES BY SEM 68
REFERENCES 70

LIST OF FIGURES

Figure 1.1	An illustration showing the basic structure of an artery [1].	3
Figure 1.2	Human coronary artery endothelial cells a) in cell culture conditions, b) transfected with GFP plasmid DNA. Human carotid artery endothelial cell c) in cell culture conditions, d) immunostained for von Willebrand Factor (green), nuclei are stained with propidium iodide (PI) (red). Human dermal Lymphatic Microvascular Cells e) in cell culture conditions f) immunolabeled for CD31/platelet endothelial cell adhesion molecule-1 (green); nuclei are stained with PI (red) [2].	4
Figure 1.3	Graphene and its forms as in graphite, fullerene and carbon nanotubes [3].	6
Figure 1.4	The imaginary, Im(Z) and real, Re(Z) components of the electrical impedance, Z. ϕ is the phase-shift angle.	11
Figure 1.5	Simulation showing electrical field lines for low (up) and high frequencies (bottom). The Figure is from [4].	13
Figure 1.6	Frequency based spectra of conductivity and relative permittivity of biological tissue.	13
Figure 1.7	Electrical model by Cho et al for human mesenchymal stem cell. Re was the extracellular resistance, CPEm was the constant phase element for the cell membrane and CPEdl was for the electrode impedance. Rs was the spreading resistance. The Figure is reproduced from [5].	14
Figure 1.8	The schema of the cells on the gold electrode. The current pathways shown in solid line and dashed line were through the space between the electrode surface and the cell, through the space between the cells, respectively.	15

Figure 1.9 Cel was the capacitance for electrode-electrolyte interface, the resistance of the culture medium was Rbulk. The electrical equivalent of the cell mono-layer was represented a parallel combination of a capacitor and the cellular resistance Rcl. The Figure was reproduced from [6]. 15

Figure 1.10 Zsol was the impedance of the electrolyte between the cells (with capacitance Csol and resistance Rsol in parallel), Zc was the impedance of the cells (capacitance of the cell membrane, Cc, and the resistance, Rc, of the cell membrane in parallel) Zp was the polarization impedance (with capaticance, Cps, and resistance, Rps). Rbulk was the impedance of the cell culture medium. The Figure was reproduced from [7]. 16

Figure 1.11 The electrical equivalent model for Hela cells from [8]. Rgap stood for the resistance of the cell-substrate gap, Cgap was the capacitance of the cell-substrate gap. Rcell was the resistance of the gaps between the cells and Ccell was the capacitance of the cell membrane. At higher frequencies the current assumed to flow through the capacitive components of the cells and at lower frequencies through the resistive components of the cells [8]. 17

Figure 1.12 A simplified electrical model of biological tissue. Cdl was the charge double layer capacitance, Rc was the cell membrane resistance, Cc was the cell membrane capacitance. Rs was the solution resistance. The figure was reproduced from [9]. 17

Figure 1.13 Single cell electrical equivalent model. Re was the resistance of the device, Cc was the cell membrane capacitance, Rc was the resistance of the cytoplasm, Cdl and CPE were the double layer capacitance and the constant phase element for the solution, respectively [10]. 18

Figure 2.1 EIS sensor a) A and b) B with graphical representation for c) A with indicating geometrical parameters; diameter of the working electrode was 4800 μm. The width of the counter electrode was 2400 μm. The gap between working electrode and the counter electrode was 5200 μm and for d) B with working electrode width was 800 μm and the width of the counter electrode was 6900 μm. The gap between the working electrode and the counter electrode was 1750 μm at the top and 1000 μm at the sides. 20

Figure 2.2 EIS sensor C and electrode dimensions. Each sensory surface consisted of 8 wells. The diameter of the smaller working electrode was 2000 μm. The gap between the working electrode was 1000 μm and the maximum diameter of the counter electrode was 4870 μm (The Figure was used by Simsek et al in [11]). 21

Figure 2.3 The schema of photo-lithography process for EIS production consisting of a 200 nm gold (Au) layer on chromium (Cr) (60 nm coated on glass wafer. PR refers to AZ5214 photoresist (The Figure was used by Simsek et al in [11]). 21

Figure 2.4 EIS sensor C with a) ibidi sticky slides and b) nichrome wires connected to the contact pads through silver epoxy. 22

Figure 2.5 Schema showing the process of surface modification. (a) Cysteamine immobilization on the Au surface. (b) GO flakes attached to the surface through amine groups of cysteamine. (c) GO reduction through hydrazine vapor reduction process (Hydrazine vapor at 40 °C) (The Figure was used by Simsek et al in [11]). 23

Figure 2.6 SEM image of a) Au surface on glass wafer coated by soft lithography method, b) Au/Cys.HCl surface, $5X10^4$ magnification. Scale bars show 1 μm. 24

Figure 2.7 SEM image of GO with magnification a) $5x10^3$ magnification, scale bar shows 10 μm and b) $2X10^4$, scale bar shows 2 μm. 25

Figure 2.8 SEM image of a) Au/rGO-2hrs, b) Au/rGO-4hrs, c) Au/rGO-6hrs, d) Au/rGO-12hrs, e) Au/rGO-18hrs, f) Au/rGO-22hrs surfaces with 5X10^3 magnification. Scale bars show 10 μm. 25

Figure 2.9 SEM images from a) Au/GO, b)Au/rGO-2h, c)Au/rGO-22h surfaces, with 5X10^4 magnification. Scale bars show 1 μm. 26

Figure 2.10 Water droplet on a) Au, b) Au/Cys.HCl, c) Au/GO surfaces. 27

Figure 2.11 Water droplet on a) Au/rGO-2h, b) Au/rGO-4h, c) Au/rGO-6h, d) Au/rGO-12h, e) Au/rGO-18h, f) Au/rGO-22h surfaces. 28

Figure 2.12 WCA values measured for Au, Au/Cys.HCl, Au/GO, Au/rGO-2h, Au/rGO-4h, Au/rGO-6h, Au/rGO-12h, Au/rGO-18h, Au/rGO-22h. Bars represent the mean values and error bars are for the standard deviations. The contact angle measurement was performed using CAM, 100, USA (The Figure was used by Simsek et al in [11]). 28

Figure 2.13 The electrical impedance response of 0.1 M KCl solution containing 10 mM $K_3Fe(CN)_6$/ $K_4Fe(CN)_6$ measured with EIS Sensors A and B, between frequencies 100 Hz and 1 MHz is seen in a) Nyquist plot for EIS sensor A. b) Bode plot for EIS Sensor A. c) Nyquist plot for EIS sensor B. d) Bode plot for EIS sensor B. 29

Figure 2.14 Nyquist plot of 0.1 M KCl solution containing 10 mM $K_3Fe(CN)_6$/ $K_4Fe(CN)_6$ measured with EIS Sensor B with Au, Au/GO and Au/rGO surfaces. The measurement frequency range was from 100 Hz to 1 MHz. 30

Figure 2.15 Bode plots a) with Z b) with impedance phase angle of 0.1 M KCl solution containing 10 mM $K_3Fe(CN)_6/K_4Fe(CN)_6$ measured with EIS Sensor B with changing frequency. The measurement frequency range was from 100 Hz to 1 MHz. 30

Figure 2.16 Linear regression of resistance and resistivity value of KCl solution. Resistance values were calculated through impedance measurements obtained by the LCR meter. Resistivity values were calculated through conductivity measurements obtained with the conductivity meter. 31

Figure 2.17 Bode plots for HCAtECs growth medium measured with EIS sensory surfaces for Au, Au/GO and Au/rGO. Error bars represent the standard deviations from measurements from the wells of the same EIS C (n=7) (up) and the from wells of two different EIS C (n=14) (bottom). 33

Figure 2.18 Fibroblast cell line on EIS sensor B on day 1 (A) and on day 8 (B). Osteoblast cell line on day 7 (C) and on day 11 (D). 34

Figure 2.19 Z and Θ angle values for fibroblast (up-left), for osteoblast (middle-left) measured with EIS sensor B. Relative impedance change ΔZ_{NoCell} (%) and corrected phase angle (Θ'). 35

Figure 3.1 Experimental EIS set-up for measuring cell proliferation on EIS sensor. 40

Figure 3.2 Representative Bode plots of HCAtECs proliferating on Au, Au/GO and Au/rGO electrodes from no cell, day 1, and day 10. Error bars stand for multiple measurements from the same well of EIS C sensor. 44

Figure 3.3 Representative Bode plots (Z and Θ with respect to frequency) of HCAtECs proliferating on Au, Au/GO and Au/rGO electrodes from no cell, day 1, day 3, day 5, day 7 and day 10. Error bars stand for standard deviations (n=6). 45

Figure 3.4 Representative Bode plots (Resistance and reactance with respect to frequency)of HCAtECs proliferating on Au, Au/GO and Au/rGO electrodes from no cell, day 1, day 3, day 5, day 7 and day 10. Error bars stand for standard deviations (n=6). 46

Figure 3.5 Impedance measurements as a function of cell incubation periods for each type of electrode surface (Au, Au/GO, Au/rGO) from "No Cell" to Day 10 (n=6). Data points represent the mean values of Z, with standard deviations in (A) for Au, (C) for Au/GO and (E) for Au/rGO. The frequency scans were from 100 Hz to 1 MHz in the outer; from 1 kHz to 100 kHz in the inlet graph. Phase angle mean values with standard deviations in (B) for Au, in (D) for Au/GO and in (F) for Au/rGO (n=6). 47

Figure 3.6 Rate of change of impedance with respect to cell medium (ΔZ_{NoCell} (%)) for each type of electrode surfaces Au, Au/GO and Au/rGO; at 4 kHZ, 5 kHz, 20 kHz, 40 kHz, 200 kHz, 350 kHz and 1 MHz. Data presented show mean ± SEM (n= 12); p values are shown according to the Kruskal-Wallis and Dunn's test post hoc test and all other remaining pairwise comparisons are non-significant. 49

Figure 3.7 Rate of change of impedance change rates with respect to (ΔZ_{Day1} (%)) for each type of electrode surfaces Au, Au/GO and Au/rGO; at 4 kHZ, 5 kHz, 20 kHz, 40 kHz, 200 kHz, 350 kHz and 1 MHz. Data presented show mean ± SEM (n=12); p values are shown according to the Kruskal-Wallis and Dunn's test post hoc test and all other remaining pairwise comparisons are non-significant. 50

Figure 3.8 Corrected phase angles for each type electrode surfaces Au, Au/GO and Au/rGO at 4 kHZ, 5 kHz, 20 kHz, 40 kHz, 200 kHz, 350 kHz and 1 MHz. Data presented show mean ± SEM (n= 12); p values are shown according to the Kruskal-Wallis and Dunn's test post hoc test, all other remaining pairwise comparisons are non-significant. 51

Figure 3.9 Representative optical images taken by Nikon Eclipse LV150 microscope (5X) of HCtAEC from the Au, Au/GO and Au/rGO surfaces on day 1. The images are from the area between the large counter electrode and the small working electrode (left) and from the large counter electrode (right). Scale bars are 100 μm. 52

Figure 3.10 Representative optical images taken by Nikon Eclipse LV150 microscope (5X) of HCtAEC from the Au, Au/GO and Au/rGO surfaces on day 3. The images are from the area between the large counter electrode and the small working electrode (left) and from the large counter electrode (right). Scale bars are 100 μm. 53

Figure 3.11 Representative optical images taken by Nikon Eclipse LV150 microscope (5X) of HCtAEC from the Au, Au/GO and Au/rGO surfaces on day 5. The images are from the area between the large counter electrode and the small working electrode (left) and from the large counter electrode (right). Scale bars are 100 μm. 54

Figure 3.12 Representative optical images taken by Nikon Eclipse LV150 microscope (5X) of HCtAEC from the Au, Au/GO and Au/rGO surfaces on day 7. The images are from the area between the large counter electrode and the small working electrode (left) and from the large counter electrode (right). Scale bars are 100 μm. 55

Figure 3.13 Representative optical images taken by Nikon Eclipse LV150 microscope (5X) of HCtAEC from the Au, Au/GO and Au/rGO surfaces on day 10. The images are from the area between the large counter electrode and the small working electrode (left) and from the large counter electrode (right). Scale bars are 100 μm. 56

Figure 3.14 Cell counts from 0.01 cm^2 of the smaller electrode surface (n=14). Data show mean ± SD; *p<0.05, ns for non-significant according to the Kruskal-Wallis and Dunn's post hoc test. 57

Figure 3.15 AB reduction value for HCAtECs on Au (n=11), Au/GO (n=12) and Au/rGO surface (n=12) on day 10. Bars and error bars show mean ± SD; According to the Kruskal-wallis test and Dunn's test for multiple comparisons, significant difference between Au and Au/GO surface (p=0.0017), significant difference between Au and Au/rGO surface for cell viability (p=0.0001). ns: no significant difference between other groups. 58

Figure 3.16 Acridine (AO)/Propidium (PI) stained HCAtECs on Au, Au/GO, Au/rGO surfaces and TCP on day 3. The images were obtained by DMIL, Leica florescent microscope. Alive cells are in green and dead cells are in red. Scale bar is 200 μm. 59

Figure 3.17 The percentage of alive HCAtECs to all HCAtECs calculated through cell counts of the AO/PI stained HCAtECs on day 3 (n=2). 60

Figure 3.18 DAPI and F-actin staining for HCAtECs on Au, Au/GO and Au/rGO surfaces. The nuclei (blue) stained by DAPI and the filaments (green) by F-actin. Scale bar represents 200 μm. 60

Figure A.1 Treatment of graphene on gold surfaces by ultrasonication and oxygen plasma treatment. 68

Figure A.2 Graphene before and after sterilization for 10 min of UV light (up). Graphene before and after the cell culture seeding (bottom). 69

LIST OF TABLES

Table 1.1	Physical Properties of Graphene [12].	6
Table 2.1	Conductivity values of KCl solutions with varying molarities.	31
Table 2.2	Standard deviation of measured impedance (STD_Z (Ω)) and impedance phase angle (STD_Θ ($^\circ$)) from multiple wells of the same EIS C sensor (n=8).	32
Table 2.3	Standard deviation of measured impedance (STD_Z (Ω)) and impedance phase angle (STD_Θ ($^\circ$)) from multiple wells of the two EIS C sensors (n=16).	32

LIST OF SYMBOLS

Au	Gold
CO_2	Carbon dioxide
Cysteamine.HCl	Cysteamine hydro-chloride
Cr	Chrome
C	Capacitance
H_2O	Water
Hz	Hertz
KCl	Potassium Chloride
kHz	Kilohertz
MHz	Megahertz
$K_3Fe(CN)_6$	potassium ferricyanide
$K_4Fe(CN)_6$	potassium ferrocyanide
GO	Graphene oxide
μl	microliter
μm	micrometer
ml	mililiter
nm	nanometer
rGO	Reduced graphene oxide
R	Resistance
SiC	Silicon carbide
Z	Impedance
Z_CPE	Constant Phase Element
ΔZ_{NoCell} (%)	Change in impedance with respect to cell medium
ΔZ_{Day1} (%)	Change in impedance with respect to day 1
Θ'	Corrected phase angle

LIST OF ABBREVIATIONS

AB	Alamar Blue
AO	Acridine orange
AC	Alternating current
BSA	Bovine serum albumin
CVDs	Cardiovascular Diseases
CVD	Chemical vapor deposition
DAPI	4', 6-diamidino-2-phenylindole
EIS	Electrical impedance spectroscopy
ECIS	Electric cell-substrate impedance sensing
DC	Direct current
HCAtECs	Human carotid artery endothelial cells
PI	Propidium iodide
PR	Photoresist
SAM	Self assembly monolayer
SEM	Scanning Electron Microscopy
UV	Ultraviolet
WCA	Water contact angle

1. INTRODUCTION AND THEORY

1.1 Motivation, aim and outline of the thesis

Cardiovascular diseases (CVDs) have the largest portion (31%-17.7 millions people) of the overall causes of the death [13]. This number is expected to be 23.3 millions in 2030 [14]. Nearly half of the deaths in Turkey (47.7%) [15] are because of the CVDs. The most common CVDs are coronary heart diseases (7.3 millions of death) and stroke (6.2 millions of death). The main reason of these diseases is endothelium dysfunction. Endothelial cells are one of the basic components of blood vessels and play crucial role in endothelium functions. Endothelialization process thus has been studied in numerous studies from numerous aspects of the process such as developing bio-materials for stent coatings. Graphene and graphene related materials are promising for their potential as a bio-material. However there are contradictory results for their effects on endothelial cells, the being toxic causing cell damage, and positively increasing cell proliferation rate. Carotid artery is one of the arteries that is related to CVDs; its blockage leads stroke. The blockage of blood flow in carotid artery is called stenosis. Stenting procedure is performed in the treatment of stenosis. However, stent bio-compatibility still needs to be improved to avoid in-stent restenosis. Graphene related materials are barely studied as bio-materials for carotid artery stents. There are limited studies for carotid artery endothelial cell proliferation on graphene materials. This study aims to reveal the usability of graphene coatings in carotid artery endothelial cell proliferation.

EIS is a powerful tool for real-time monitoring of cell behaviour. A hypothesis is that real-time monitoring stent-restenosis will enhance treatment processes [16]. EIS can be promising for monitoring in-stent restenosis. To the best of our knowledge there is no study on electrical analysis of carotid artery endothelial cells.

In this thesis, the electrical behaviour of carotid artery endothelial cell proliferation on graphene based surfaces was searched.

In Chapter 1, endothelialization in CVDs is summarized. Since graphene oxide (GO) and reduced graphene oxide (rGO) were utilized in endothelialization process; basic theory of graphene related materials with its recent applications on endothelialization are considered. EIS, the method utilized for monitoring endothelial cells, is briefly explained, electrical equivalent models for biological tissues used in literature are listed.

In Chapter 2, processes for GO and rGO coating on Au surface and the results for the characterization of the coated surfaces are indicated. The characterization methods include scanning electron microscopy (SEM), water contact angle measurements (WCA) and electrical measurements. Also in this chapter, the production process of EIS sensor used in electrical measurements is given. The preliminary cell culture studies with fibroblast and osteoblast cell line are shown. The findings are discussed.

In Chapter 3, the methodology and results for human carotid artery endothelial cell (HCtAEC) proliferation from day 1 to day 10 by EIS, Alamar Blue (AB) cell viability assay, 4', 6-diamidino-2-phenylindole (DAPI) and F-actin immunostaining, cell count analysis from optical images and acridine orange/propidium iodide (AO/PI) staining were presented. The results of the measurements are explained and discussed.

In Chapter 4, the conclusion of the study with future directions is given.

1.2 Endothelialization in Cardiovascular Diseases

The wall of the blood vessel consists of three layers; tunica intima, tunica media and tunica adventitia (Figure 1.1). Anchored endothelium and the basal lamina constitute intima layer [17]. Basal lamina acts as a scaffold for the arteries. It is covered with endothelial cells at its side facing the blood (inner side) and with smooth muscle cells at the outer side. Tunica media layer contains smooth muscle cells in large amount; it also contains elastin and collagen [18]. Tunica media and tunica adventitia are seperated by external elastic lamina. Tunica media acts in adjustments to the os-

cillations and maintenance of the vascular tone [19]. Tunica adventitia, a collagenous structure, is the outermost layer of the blood vessel and contains fibroblasts, mast cells, nerve endings [20]. Tunica adventitia provides nutrients to its surrounding tissue through small blood vessels, that are called vasa vasorum [18]. Endothelium, consisting

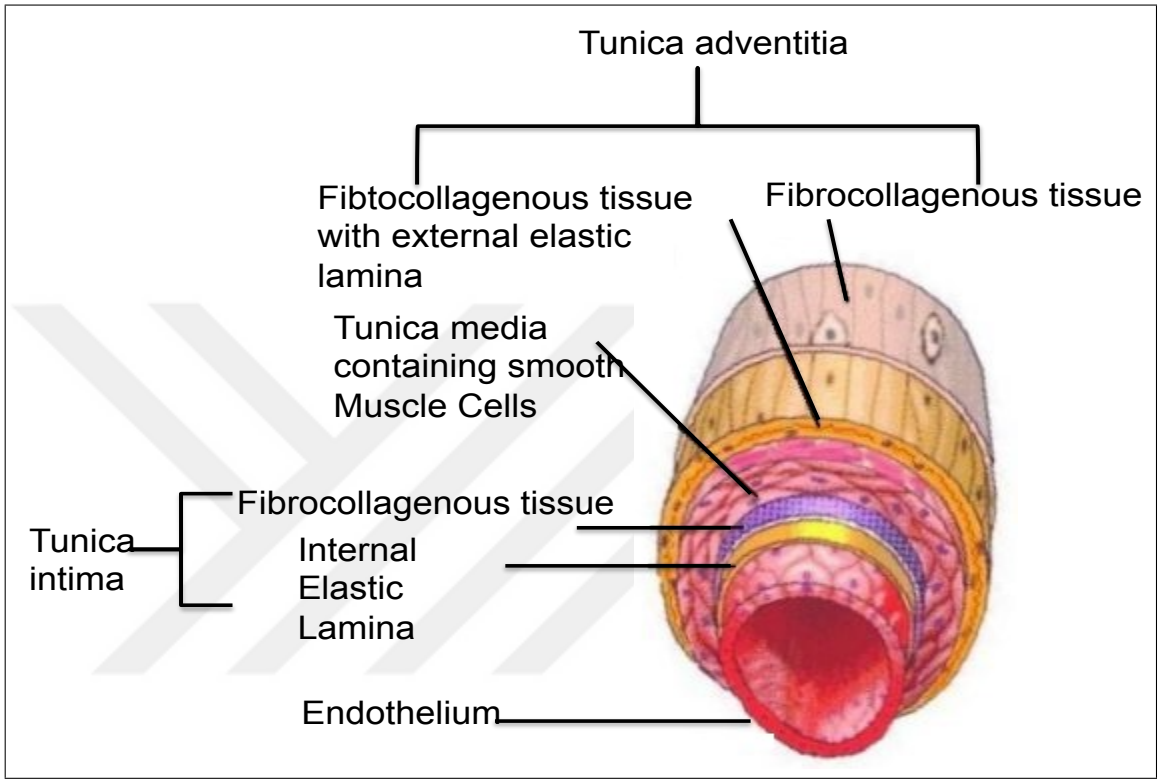

Figure 1.1 An illustration showing the basic structure of an artery [1].

of a mono-layer of endothelial cells, is the inner surface of the blood vessels and the lymphatic system. Endothelium not only plays a preeminent role in the regulation of vascular homeostasis, vascular tone, innate immunity, blood fluidity, thrombosis, fibrinolysis, angiogenesis, and inflammation [21], but also serves barrier function for the blood from surrounding tissue [22]. Endothelium dysfunctions lead to various diseases such as atherosclerosis, aneurysm, stroke, heart diseases, tumor growth, chronic kidney failure, insulin resistance, diabetes, viral infections [21]. Since endothelial dysfunction is vital for these common and serious diseases; endothelial cells are prominent in arterial functioning. Vascular implants such as by-pass grafts, heart valves and stents are used for the treatment of these diseases. The implants have to be bio-compatible. Endothelialization is the key factor in determining bio-compatibility. Researches on endothelial cell have performed widely in numerous aspects [23, 24]. The morphology

of endothelial cell varies according to its location in the vascular tree, but in general terms, it has a thickness of 0.1-10 μm, 10-30 μm width and 50-70 μm length [17]. Figure 1.2 shows the three examples of endothelial cells in the vascular system; human coronary artery endothelial cells, human carotid artery endothelial cells and human dermal lymphatic micro-vascular endothelial cells. Atherosclerosis is mostly the un-

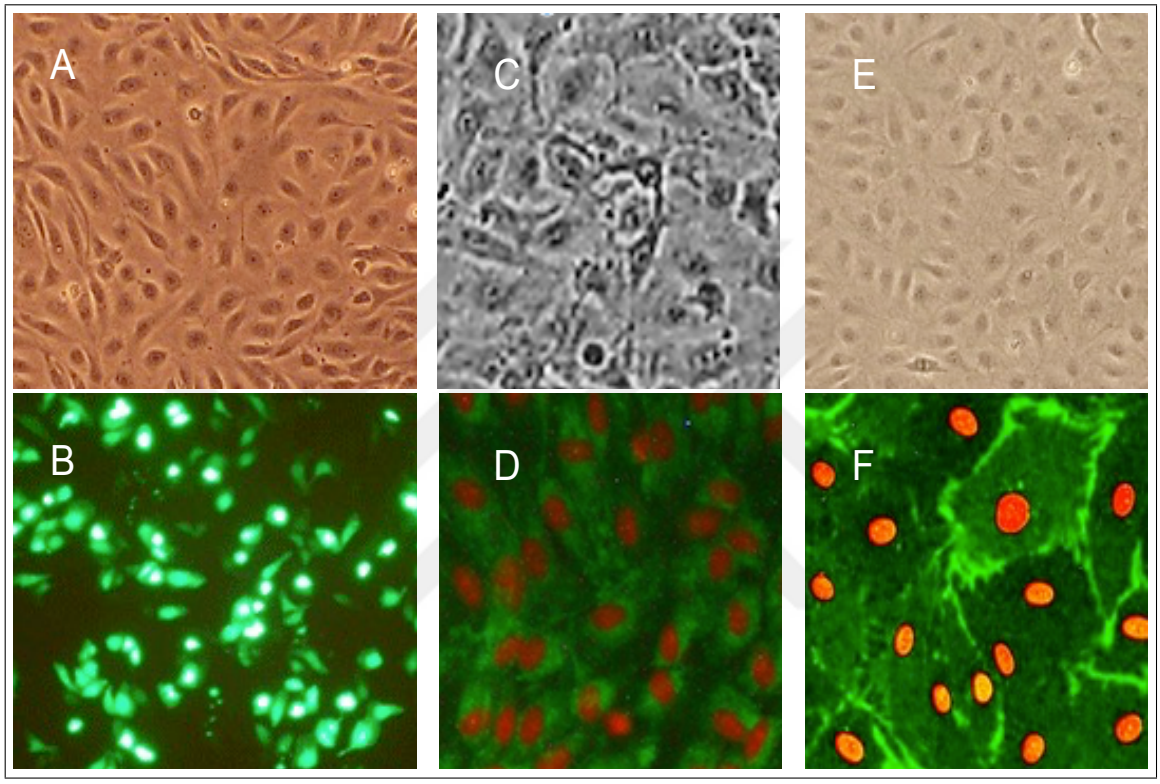

Figure 1.2 Human coronary artery endothelial cells a) in cell culture conditions, b) transfected with GFP plasmid DNA. Human carotid artery endothelial cell c) in cell culture conditions, d) immunostained for von Willebrand Factor (green), nuclei are stained with propidium iodide (PI) (red). Human dermal Lymphatic Microvascular Cells e) in cell culture conditions f) immunolabeled for CD31/platelet endothelial cell adhesion molecule-1 (green); nuclei are stained with PI (red) [2].

derlying reason of the CVDs [20]. Atherosclerosis is the occlusion of the blood vessel, blocking the blood flow [25]. Stent deployment is a percutaneous coronary intervention commonly used in reopening of the occluded blood vessel [26]. The endothelial cell behaviour on stent is crucial. Stent endothelialization is a key process for its biocompatibility. Thus improving stent surface for endothelialization has been widely studied [27–31]. When atherosclerosis exists in carotid artery, occlusion of carotid artery cell may lead to stroke. Stenting procedure can also be utilized in carotid artery intervention. Although, the very first stent material are stainless steel, other materials

such as nickel-titanium (Ni-Ti) (nitinol), cobalt-chrome (Co-Cr) have been utilized in clinics for carotid artery [32]. Researches for titanium, platin-iridium [33], tantalum, magnesium [34] as stent material has been continuing [35]. The re-occlusion of the blood vessel after stent implantation, which is called in-stent-restenosis still a problem and studies are continuing for its inhibition. Stent endothelialization is the key step for preventing in-stent restenosis. There are studies for improving stent endothelialization through coating the stent metal with organic or inorganic molecules [36], modifying stent surface with laser applications [37], varying stent geometry [38, 39]. Graphene based molecules have also been utilized in enhancing endothelialization [40–43]. In this thesis, GO and rGO molecules were studied in their contribution to the carotid artery endothelial cell proliferation.

1.3 Graphene

Graphene is sp2 hybridized carbon atoms constituted in hexagonal lattice forming honeycomb structure. Carbon is a fundamental element for life, existing abundantly in the nature. The flexibility of its binding structures gives diversity to carbon in its physical properties. Graphite consists of sp2 hybridized carbon layers; each layer is called graphene [44]. Graphene layer has a 2D structure and one-atom-thickness, due to the planar form of sp2 hybridization. Graphene can form carbon nanotubes (1D) when it is rolled. It can form fullerenes (0D) when pentagonal structures formed at the edges resulting a ball shape. When it is stacked, it forms graphite, which is the multi-layered graphene. These structures are seen in Figure 1.3 [3]. Graphene is widely used in science and technology such as in energy storage [45], energy production [46], catalysis [47], batteries [48], opto-electronics, solar cells, photovaltaics [49], water filtration [50], biomedical applications [51] including drug delivery [52], antibacterial activity [53], tumor therapy [54], anti-thrombogenic activity [55], endothelialization [56] etc. The reason of its wide applicability is that graphene exhibits unique electrical, optical, mechanical and thermal properties such as high electrical conductivity, high elasticity and stiffness, high mechanical strength and transparency [12]. The basic physical properties are listed in Table 1.1. Graphene based molecules can be listed as; GO [57],

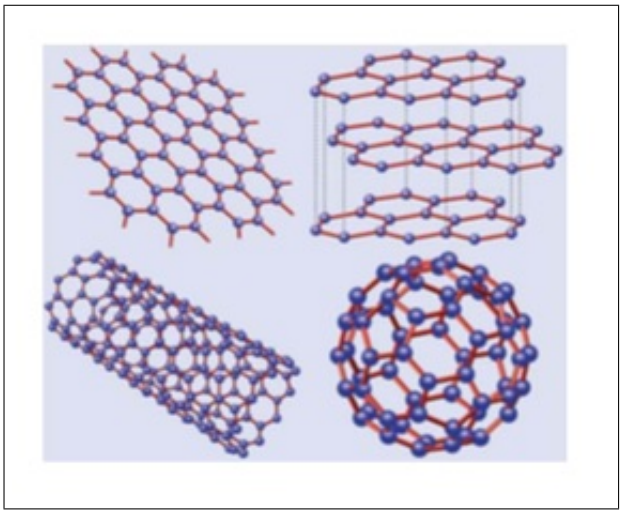

Figure 1.3 Graphene and its forms as in graphite, fullerene and carbon nanotubes [3].

rGO [58], graphene quantum dots [59], graphene nanoribbons [3], graphene fluoride (fluorographene) [60], and the composites with other molecules such as Au/GO, Au/rGO, Au/pristine graphene, ZnO/rGO, $/TiO_2$/rGO, Cu/rGO, NiO/graphene etc [61].

Table 1.1
Physical Properties of Graphene [12].

Property	Value
Band gap	Zero
Charger carrier mobility	$\approx$ 200 000 $cm^2/V.s$
Specific surface area	$\approx$ 2530 m^2/g
Tensile strength	$\approx$ 1100 GPa
Thermal conductivity	$\approx$ 5000 W/m.K
Transparency	$\approx$ 97.4 % GPa
Young's modulus	$\approx$ 1 TPa

The outstanding physical properties stem from the sp2 hybridization of the graphene [62]. In sp2 hybridization s, px, py orbitals form hybridized states and form sigma bonds. The remaining pz orbital which is perpendicular to the planar plane, forms pi bonds [63]. The planar plane is more stable and gives graphene its high conductivity [64]. Through the plane the orbitals form strong bonds which makes the graphene stiff, whereas through the perpendicular direction, i.e through the layers, the

weak van der Waals bonds give graphene its softness [59].

1.3.1 Synthesis of Graphene

There are several methods for the synthesis of graphene. Mechanical exfoliation is the method used by Novoselov and Geim [65], who won the Nobel prize winner for not only building graphene flake on $_2$ substrate but also determining its electrical properties. The synthesis method are categorized as top down and bottom up approaches. Top down methods are; mechanical exfoliation, chemical exfoliation, chemical synthesis, unzipping of carbon nanotubes, arc discharge. Bottom up methods are; epitaxial growth on silicon carbide (SiC), chemical vapor deposition (CVD), plasma enhanced chemical vapor deposition (PECVD), prolysis [64]. Mechanical exfoliation is the very first method used for graphene synthesis. Exfoliation of graphite is the repetitive peeling process in order to overcome the van der Waals bonding forces. In mechanical exfoliation these forces are broken by mechanical energy and in chemical exfoliation by chemical energy [66]. Mechanical exfoliation required much labor work thus it is not available for mass production. It is rather preferred to study the physical properties of the graphene [64]. The disadvantage for chemical exfoliation is the cost of ionic solutions used in the process. In CVD, carbon containing gases are pyrolyzed by heating and then graphene layers are deposited on substrate materials using carrier gases. Although CVD can produce larger sized flakes, it has small production scale [63]. In CVD process, the difficulty in maintaining required environment for the production, such as high temperature, ultra high vacuum environment is a disadvantage. Another disadvantage is the intense labor required in isolating the graphene flakes form the substrate which graphene is deposited on. Arc discharge is the direct current flow through graphene electrodes to obtain the flakes. Another top-down method is unzipping carbon nanotubes in order to obtain the flakes. Chemical solutions [67], laser ablation [68] and plasma etching [69] can be used for unzipping process. Epitaxial growth of graphene on SiC is performed in ultrahigh vacuum chamber by heating the SiC to high temperatures. Since the sublimation temperature of carbon is higher than that of silicon, silicon sublimes at around 1500 °C, graphene layers remains on the

surface [70]. Exfoliation of graphite oxide is more easy than that of graphite because oxygen groups increase the gap between the layers. Thus, another method to obtain graphene is by reducing GO. GO can be obtained through oxidation (forms graphite oxide) and ultrasonication of graphite, which is called Hummer's method. Resulting GO molecules are reduced in order to achieve graphene-like molecule, which is called as reduced graphene oxide (rGO). Oxidized form of graphene, GO, is more hydrophilic and acts as an insulator (sp2 hybridization is disrupted by functional groups) whereas graphene is a good conductor. Thus by reduction of GO, electrical properties of graphene is rendered by removing oxygen groups and recovering aromatic double bonds. Nevertheless, the pure graphene properties can not thoroughly achieved due to the limitations of the reduction processes and the defects occurring during the oxidation of graphite oxide. However this defected property renders rGO its promising use in sensors [71].

1.3.2 Graphene and Graphene Related Materials in Endothelialization

As various applications of graphene related materials, they were also utilized for their contribution to endothelial cell behaviour. Pan et al, used heparin loaded GO coatings on titanium surface. Decreased surface hydrophilicity by GO further reduced with heparin [56]. Their results showed that GO enhanced adherence and proliferation of endothelial cell compared to bare titanium. Since endothelialization is crucial in stent bi-compatibility, any material that enhances endothelialization process can be considered as a good candidate for stent material. Platelet aggregation and smooth muscle cell adhesion are also parameters for indicating the applicability biomaterial on stent surface. Ge et al tested these parameters for docetaxel loaded GO coating on stainless steel surface and revealed that the complex inhibited thrombosis and smooth muscle cell proliferation [42]. Podila et al studied the graphene coating on nitinol surface and detected increased rat aortic smooth muscle and endothelial cell proliferation [43]. Cardenas et al coated stainless steel surface with reduced GO by drop casting and analyzed the composite for human umbilical vein endothelial cell (HUVEC) viability. They did not detect any significant toxicity of the rGO [41]. Zhou

et al utilized GO complex on polyethersulfone and detected increased human HUVEC proliferation [55]. In another study, Yun et al showed increased HUVEC proliferation with GO and rGO coated glass wafers compared to the cover slips [72]. These are some of the examples revealing the positive effects of graphene and its derivatives to the endothelialization. However, there are also contradictory results in the literature showing the toxicity of GO and rGO to endothelial cells. Das et al added GO and rGO flakes into the cell medium of the umbilical vascular endothelial cells. Both GO and rGO decreased the cell viability and cell adhesion rates, rGO being less toxic compared to the GO [73]. Lim et al also detected GO toxicity to the HUVECs when incubated the cells with GO containing cell medium [74]. The incubation of HUVECs in few layered graphene caused in reactive oxygen species formation, damage of cellular components such as lipids, proteins, DNA and subsequently decrease in cell viability [75]. Similar results reported by another group that 25 and 50 μg/ml of GO triggers cellular mechanisms like reactive oxidative stress causing anti-angiogenesis, i.e; failure in endothelial cell proliferation [76]. The difference of these contradictory results is that the graphene-related materials ameliorate endothelial cell proliferation when the cells are seeded on graphene and/or graphene composite coated surfaces, whereas if the flakes are added into the cell medium (rather than coating on the surface which cells adhere) they can be toxic and cause failure in cellular integrity and decrease in cell proliferation rates. The main reason for this seems to be the concentration level of graphene related material. The concentration level of graphene related materials interacting with the cells is critical for their contribution to cellular mechanism; high level of concentrations of graphene can be more toxic [77].

1.4 Impedance Spectroscopy

EIS is a powerful and non-invasive tool to monitor electrical properties and interfaces with the electrolyte of any material [78]. The material can be liquid, solid, ionic, semiconductors and dielectric and even a single cell [79]. In 1940s, Wallace Henry Coulter declared the principles for measuring cell volume by electrical measurements. He then patented Coulter Counter; a resistance based measurement at direct current

(DC) for cell volume analysis [80]. Later on AC measurement technique speeded up and became a powerful tool in biosensor analysis. Giaever and Keese pioneered this era with their work in 1984 and called the method as electrical cell-substrate impedance sensing (ECIS) afterwards [81]. They monitored cell adhesion on gold electrodes by applying AC voltage and measuring resulting impedance. For electrochemical analysis there are two types of measurement techniques: The faradic and non-faradaic forms of electrical analysis [82]. In faradaic EIS, redox probe is used and the existence of cells on the electrode impedes the redox process on the electrodes resulting increase in impedance values [83]. Faradaic EIS measurements are highly sensitive but lack the repeatability of the measurements due to the flow of ions in the solution. On the other hand non-faradaic EIS; which is the case for ECIS systems, utilizes the cell adherence on the electrode surface impeding the current flow [84]. This form of impedance measurement also enables more detailed modeling of the cell behavior [85].

1.4.1 Basics of Electrical Impedance Spectroscopy

The characterization of any material can be performed by various techniques such as optical, mechanical, chemical, electrically, or magnetic [86]. In electrical characterization, any physical property of the system or the material is transformed into the electrical domain. Each system responds in a unique manner to the applied electrical signal. Through the electrical measurements, modeling information about the system is obtained [87]. Electrical impedance (Z) is the ability of material for hindering electrical current through it. In electrochemical impedance, small AC voltage is applied and the current response is measured. The applied AC electrical potential is in the form:

$$\mathbf{V(t) = Vm \cdot (2\pi f \cdot t)} \tag{1.1}$$

where V(t) is the time dependent voltage, Vm the maximum value of the voltage and f is the frequency in Hertz. The resulting current is:

$$\mathbf{I(t) = Im \cdot (2\pi f \cdot t + \phi)} \tag{1.2}$$

Im is the maximum value of the current and ϕ is the phase difference between the current and the voltage. For purely resistant components, ϕ is equal to zero. The complex impedance Z is the ratio of the applied voltage to the resulting current in Eq. 1.3:

$$\mathbf{Z(t)} = \frac{\mathbf{V(t)}}{\mathbf{I(t)}} \tag{1.3}$$

Imaginary and real part of the impedance are $X = Im(Z)$ and $R = Re(Z)$, respectively. Z can be written in form

$$\mathbf{Z(t)} = \mathbf{Re(Z)} + j\mathbf{Im(Z))} = \mathbf{R} + j\mathbf{X} \tag{1.4}$$

where $j^2 = -1$.In polar coordinates, with |Z| is the magnitude of, Z can be expressed as:

$$\mathbf{Z(t)} = |\mathbf{Z}|\mathbf{e}^{\mathbf{j}\phi} = |\mathbf{Z}|(\mathbf{cos}\phi + \mathbf{jsin}\phi) \tag{1.5}$$

and

$$|\mathbf{Z}| = \sqrt{\mathbf{R^2} + \mathbf{X^2}} \tag{1.6}$$

$$\phi = \mathbf{arctan}(\frac{\mathbf{X}}{\mathbf{R}}) \tag{1.7}$$

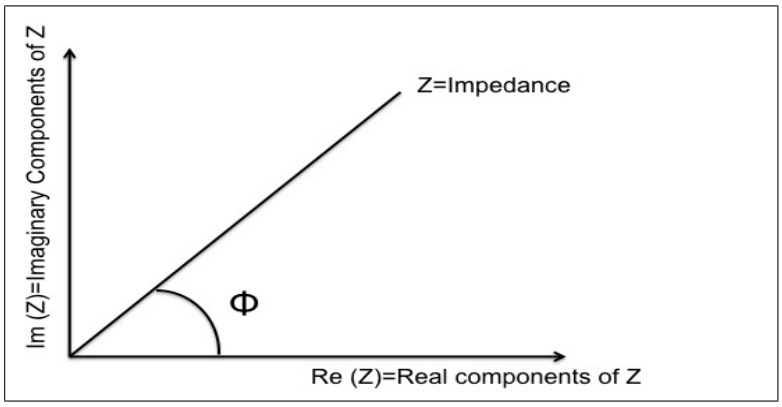

Figure 1.4 The imaginary, Im(Z) and real, Re(Z) components of the electrical impedance, Z. ϕ is the phase-shift angle.

1.4.2 Electrical Properties of Biological Tissues

Biological tissues and human body have been characterized by their electrical characteristics through electrical measurements [88, 89]. Tissues and biological cells with applied electrical signal behave both as a conductor and an insulator. The conductive behaviour of the biological tissue stems from the ionic compound of the tissue such as intra-cellular fluids. The cell membrane and polar components of cells such as proteins are related to the dielectric properties of tissue. As it will be seen in the next section of this chapter, biological cells are modeled with resistive (R) and capacitive (C) components. Due to its capacitive components such as cell membrane, biological tissue has a time-dependent behaviour. Thus, EIS is more powerful for monitoring cell behaviour rather than the direct current analysis. For example, when AC currents applied in lower frequencies, the current flows through the cells. At low frequencies capacitive reactance is high, thus the current can not pass through the cell membrane. However, When the frequency increases, the capacitive reactance decreases and the cell membrane allows the current flow through it. A simulation study in the literature shows the electrical field distribution for cells adhered on electrodes (Figure 1.5). The frequency-dependent behaviour of the biological tissue were analyzed in three different dispersion regions as seen in Figure 1.6 [90].

Alpha (α) dispersion occurs between the frequencies 1 Hz and 100 kHz [91]. Although the mechanisms behind the alpha dispersion are not clear, conductance through the gaps of the cellular membrane allowing ionic flow, double-layer cellular membrane and the ionic content of the environment are suggested reasons by Schwan in [90]. Beta (β) dispersion region, from 100 kHz to 1 MHz, is related to the cellular structure of the biological materials. At frequencies above 10 GHz, gamma (γ) dispersion region is characterized by the water, protein and salt content of suspension of the cells and the biological tissue.

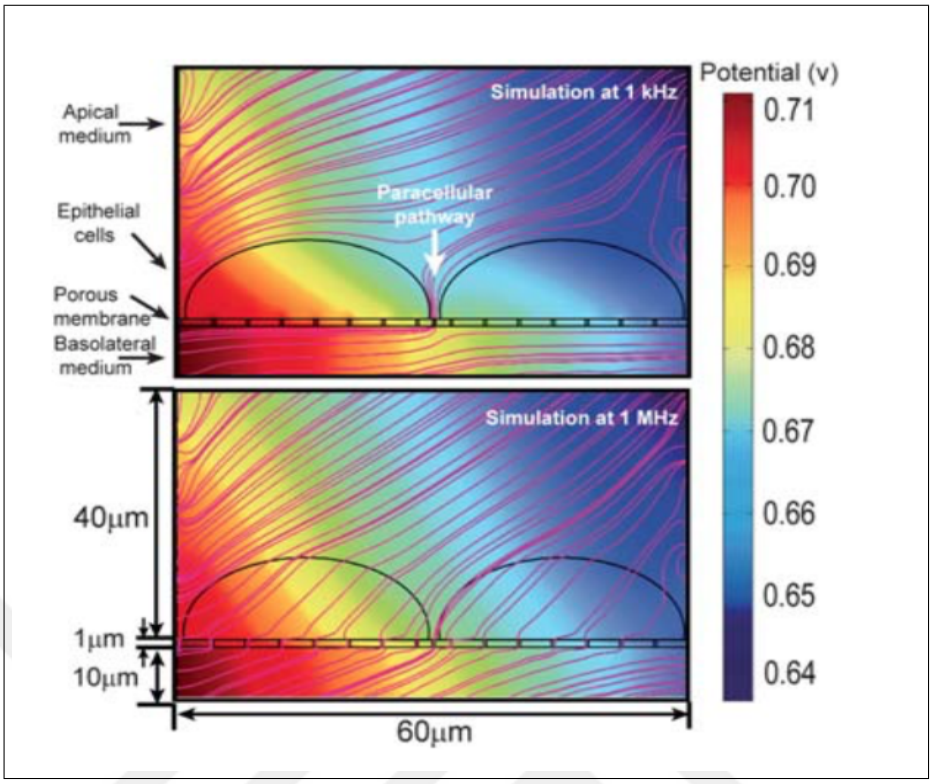

Figure 1.5 Simulation showing electrical field lines for low (up) and high frequencies (bottom). The Figure is from [4].

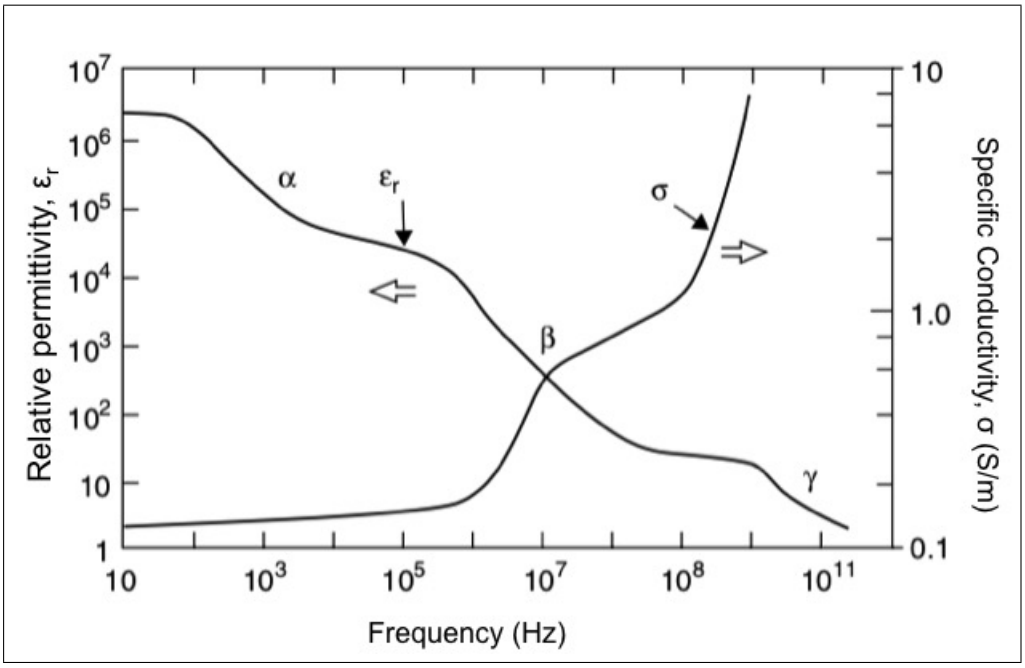

Figure 1.6 Frequency based spectra of conductivity and relative permittivity of biological tissue.

1.4.3 Electrical Equivalent Models of Biological Tissue

In non-faradaic electrical measurements of biological cells; electrode-electrolyte polarization, the cell interior and the cell membrane, distance between the cells and the substrate and distance between the cells are the main parameters used in electrical equivalent models [5–7, 81]. Electrode polarization impedance is generally modeled as parallel combination of a resistance and capacitance. Since the capacitance is not ideal when the biological cells adhere and proliferate on the electrode surface, a constant phase element is preferred in the models as seen in Eq. 1.8.

$$\mathbf{Z_{CPE} = Q^{-1} * (jw)^n} \tag{1.8}$$

where Q is the magnitude with unit $S.sn/cm^2$, w the angular frequency and n ($0 \leq n \leq 1$) is a constant describing inhomogenities; n=1 when the Z_{CPE} element is a pure capacitor. The cell membrane capacitance and the electrode-electrolyte capacitance were modeled with constant phase elements due to their non-ideal behaviour [40]. Cho et al modeled the growth of human mesenchymal stem cell on gold electrodes by constant phase element for the electrode impedance (CPEdl), the cell layer impedance (a parallel combination of a cell membrane constant phase element (CPEm) and extracellular resistance) and a resistance due to the spread of the cell (Figure 1.7) [5]. The pioneers

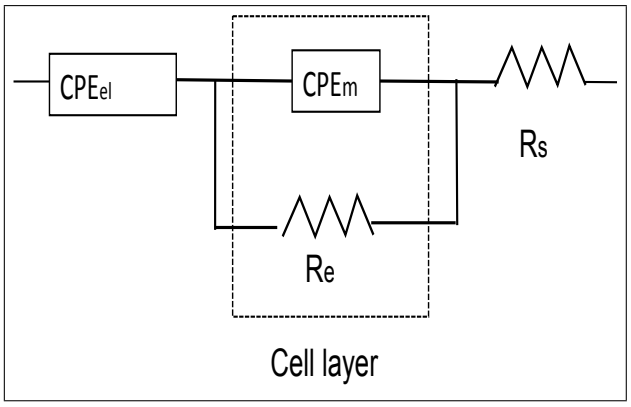

Figure 1.7 Electrical model by Cho et al for human mesenchymal stem cell. Re was the extracellular resistance, CPEm was the constant phase element for the cell membrane and CPEdl was for the electrode impedance. Rs was the spreading resistance. The Figure is reproduced from [5].

of the ECIS study, Giaever and Keese in 1984 monitored the electrical response of the fibroblast cell behaviour on the gold electrodes to the 0.1 V AC signal applied at 4 kHz.

They evaporated gold electrodes on the bottom of polystyrene dishes [81]. They later measured the micro-motion of the fibroblast cells in AC signal and modeled the current pathways as in Figure 1.8 [92]. Wegener et al. utilized ECIS method to measure the

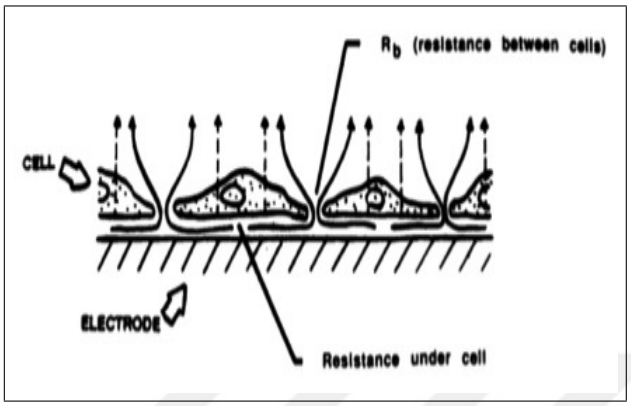

Figure 1.8 The schema of the cells on the gold electrode. The current pathways shown in solid line and dashed line were through the space between the electrode surface and the cell, through the space between the cells, respectively.

trans-endothelial and trans-epithelial resistances (TER). They showed the advantages of the ECIS in measuring TER by comparing their results with the conventional TER measurement method. The advantages were the availability to collect data from larger area and at normal cell culture conditions. They modeled the TER in ECIS analysis as in Figure 1.9 [6]. Goda in his study, in 2005, proposed a model similar to the

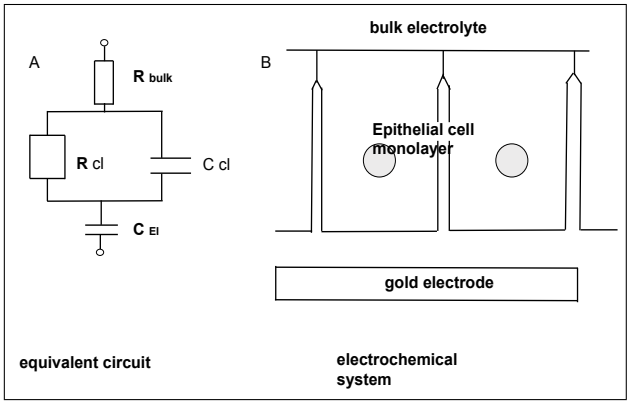

Figure 1.9 Cel was the capacitance for electrode-electrolyte interface, the resistance of the culture medium was Rbulk. The electrical equivalent of the cell mono-layer was represented a parallel combination of a capacitor and the cellular resistance Rcl. The Figure was reproduced from [6].

literature containing polarization impedance Zp, cell medium resistance, Rbulk, and cellular impedance, Zc. He also added to the model the impedance of the electrolyte

between the cells, Zsol as a parallel combination of Rsol and Csol, corresponding to the resistance between the cells and the capacitance between the cells, respectively (Figure 1.10) [7]. They studied the electrical contributions of the cell-to-cell distance (A) and the cell-substrate distance (h). Zp was given as a function of h and Rbulk was a function of A. Qiu et al also modeled cell-substrate gap resistance connected in parallel to the cellular capacitance [93]. In most models for cells spreading on the electrodes,

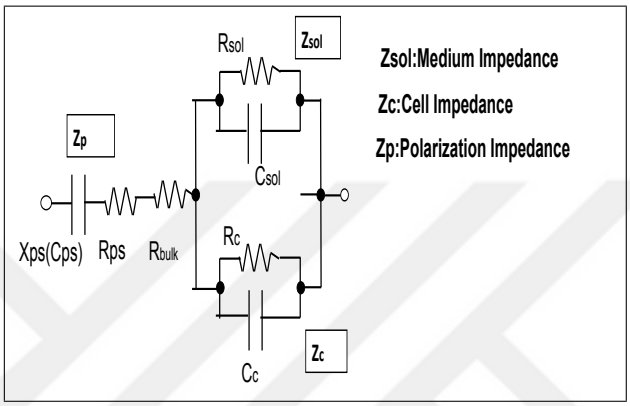

Figure 1.10 Zsol was the impedance of the electrolyte between the cells (with capacitance Csol and resistance Rsol in parallel), Zc was the impedance of the cells (capacitance of the cell membrane, Cc, and the resistance, Rc, of the cell membrane in parallel) Zp was the polarization impedance (with capaticance, Cps, and resistance, Rps). Rbulk was the impedance of the cell culture medium. The Figure was reproduced from [7].

the resistance of the gap between the cell and the substrate were used. It was named as cellular resistance, gap resistance or seal resistance. T. Anh-Nguyen et al. modeled MCF-7 breast cancer cells by cellular impedance in series with resistance of cell culture medium and electrode impedance. Cellular impedance was modeled as seal resistance in parallel to the the cell membrane resistance and capacitance, [94]. Wang et al modeled the cell-subsrate gap impedance in series to the cell impedance [8]. For the lower frequencies they simplified the model as the current flew through the resistances of the cell and for higher frequencies the current flow was through the capacitive components of the cells (Figure 1.11). As seen from above, there exist variations in the electrical models for biological tissues. The reasons are the variations in the measurement set-up, in the electrode geometry and material, and the cell type. However, the models can be generalized in the form shown in Figure 1.12 [9, 95]. The models mentioned above are for the cell mono-layer growing and spreading on the electrode surfaces. In impedance analysis of a single cell, rather than cell mono-layer spreading on the elec-

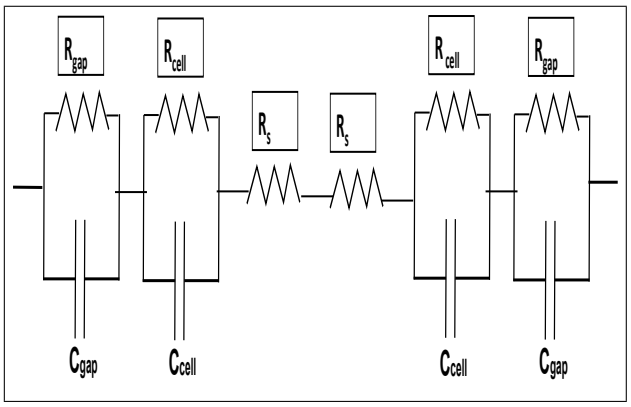

Figure 1.11 The electrical equivalent model for Hela cells from [8]. Rgap stood for the resistance of the cell-substrate gap, Cgap was the capacitance of the cell-substrate gap. Rcell was the resistance of the gaps between the cells and Ccell was the capacitance of the cell membrane. At higher frequencies the current assumed to flow through the capacitive components of the cells and at lower frequencies through the resistive components of the cells [8].

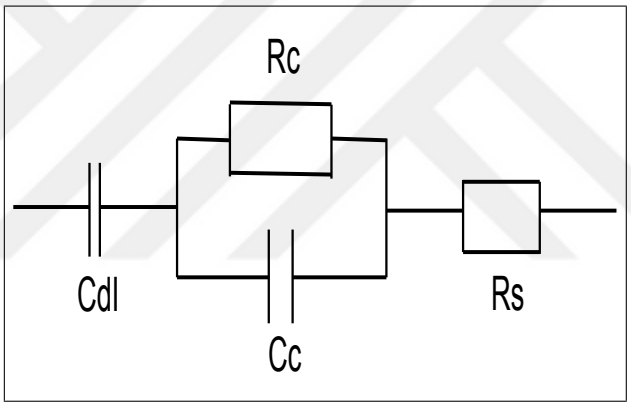

Figure 1.12 A simplified electrical model of biological tissue. Cdl was the charge double layer capacitance, Rc was the cell membrane resistance, Cc was the cell membrane capacitance. Rs was the solution resistance. The figure was reproduced from [9].

trodes, another model was proposed. For a single cell trapped by dielectrophoresis, J.-L. Hong et al proposed a different model, where the resistance of the cytoplasm was connected to the cell membrane capacitance, in series. The parallel path for the current flow was the double layer capacitance and the constant phase element of the solution as in Figure 1.13. [10]. In most of the ECIS studies, the electrical model may vary; impedance normalization with cell growth medium is necessary. The normalized impedance is calculated as in Eq. 1.9:

$$\mathbf{NormalizedZ} = \frac{\mathbf{Z_{cell}} - \mathbf{Z_{Nocell}}}{\mathbf{Z_{Nocell}}} * \mathbf{100} \tag{1.9}$$

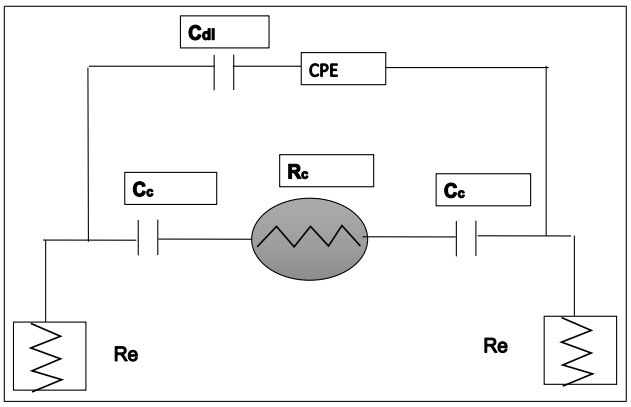

Figure 1.13 Single cell electrical equivalent model. Re was the resistance of the device, Cc was the cell membrane capacitance, Rc was the resistance of the cytoplasm, Cdl and CPE were the double layer capacitance and the constant phase element for the solution, respectively [10].

1.5 Graphical Representation of EIS

Graphical methods are used in the interpretation of impedance data regardless of the electrical models [96]. The Nyquist plot, Bode plots and the Cole-Cole circles are the common graph models in EIS. A typical Nyquist graph shows the imaginary and the real components of the impedance. Bode plots are the representation impedance value with respect to frequency. Impedance value can be Z, the impedance phase angle, the normalized impedance magnitude, the corrected phase angle, the real component of the impedance and the imaginary component of the impedance. Cole-cole plots represent the real and the imaginary components of the complex capacitance or complex permittivity with respect to each other [95].

2. DESIGN AND CHARACTERIZATION OF EIS SENSORS

Preliminary studies and the electrode characterization were performed with electrodes called EIS Sensor A, EIS sensor B and EIS sensor C. GO coating and reduction of GO were performed and analyzed through electrical, optical and water contact analysis. The preliminary cell culture studies were performed by L929 cell line and osteoblast cell line. Electrical characteristics of sensors were measured through redox probe, potassium chloride (KCl) solution and cell culture medium and results are presented as Cole plot and Bode plots. The Cell factor analysis were performed by measuring the electrical conductivity of the KCl with changing density.

2.1 The Sensor Design

Photo-lithography technique was used to produce the Au surface electrodes for further use as an EIS sensor. The geometry of the sensor A and B were constructed using Adobe Illustrator program 2.1. The geometry of the sensor C was designed in the Layout Editor program. The mask of sensor C was produced at UNAM, Bilkent. EIS Sensor C consisted of a large electrode and a smaller circular working electrode with a diameter of 2000 μm. The gap between the working electrode and the sensing electrode was 1000 μm. The geometrical design is seen in Figure 2.2. The working area for cell seeding and for measurements with redox solution was 1 cm^2. Each sensor consisted of eight working areas, i.e; sensory surfaces.

Borofloat 33100 mm (University Wafers, model ID: 2012) was used as glass wafer. The thickness of the glass was 1000 μm. The cleaning process of the glass wafers were sonication in ultrasonic bath with acetone, ethanol, and (deionized) dI H_2O for 5 min each. Ti-prime MicroChemicals GmbH, Germany) was coated onto the glass wafers using the spin coater Brewer Science Cee 200 CBX (USA). The spin rate was 5000 rpm for 50 s. Following, the substrate was baked at 120° C for 2 min. After

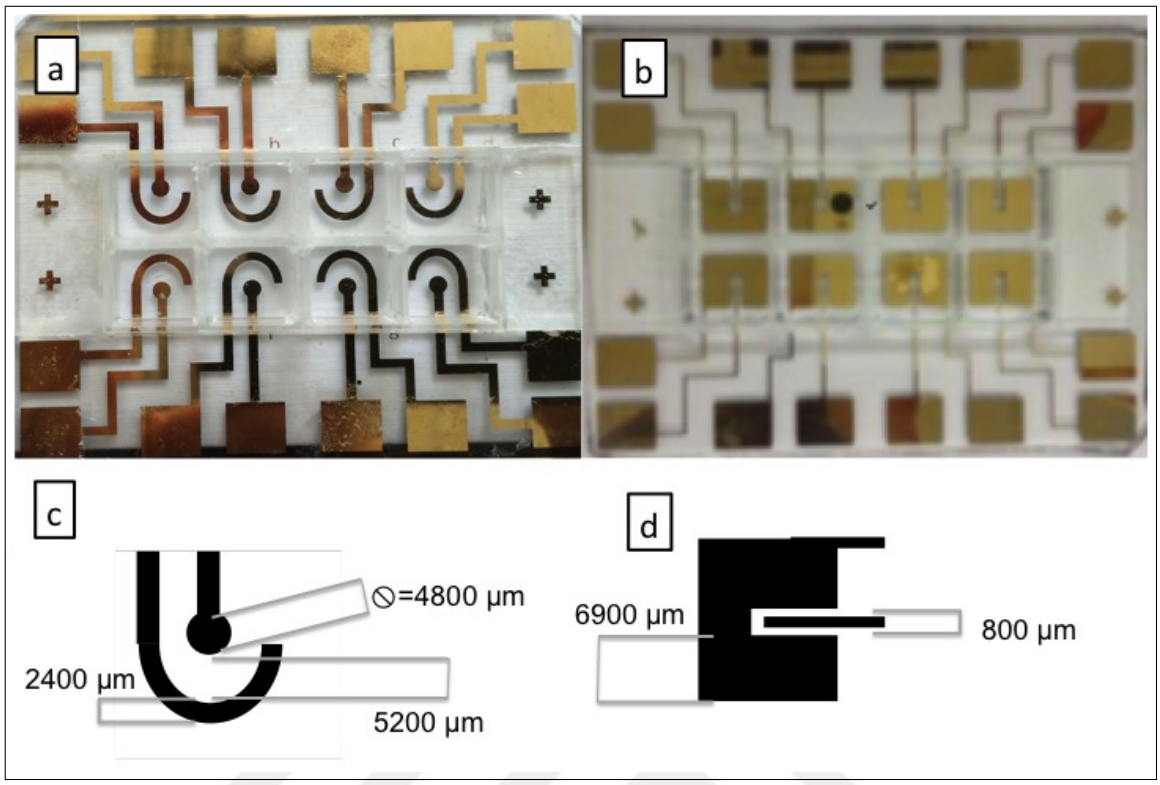

Figure 2.1 EIS sensor a) A and b) B with graphical representation for c) A with indicating geometrical parameters; diameter of the working electrode was 4800 μm. The width of the counter electrode was 2400 μm. The gap between working electrode and the counter electrode was 5200 μm and for d) B with working electrode width was 800 μm and the width of the counter electrode was 6900 μm. The gap between the working electrode and the counter electrode was 1750 μm at the top and 1000 μm at the sides.

allowing the substrate to cool for 3 min, photo-resist (PR) AZ 5214 (MicroChemicals GmbH, Germany) was coated on the surface by spin coating with a spin rate of 4000 rpm, for 40 s. The wafer was baked at 110°C for 50 s before mask alignment. The substrate was exposed to ultraviolet light (UV) of density of 40 mJ/cm^2 through the mask. Post bake was performed at 120°C for 2 s. For image reversal, the substrate was irradiated 200 mJ/cm^2 UV light without mask. The PR was developed by stirring the substrate at 100 ml aqueous solution of AZ400 K (MicroChemicals GmbH, Germany) (4:1) for 70 s. Bruker Dektak XT profile meter was used to measure the thickness of the PR 1200 $\pm$ 20 nm. As a last step for the photo-lithography, the substrate was washed thoroughly with dI H_2O and dried under N_2. By plasma-enhanced vapor deposition (Vaksis, TR), 200 nm of Au was coated on substrate following the formation of 60 nm of Cr layer. The argon gas low rate was 20 sscm. Cr was used to adhere Au on the glass. To obtain the electrode geometry, PR was dissolved in acetone for 8 min. The

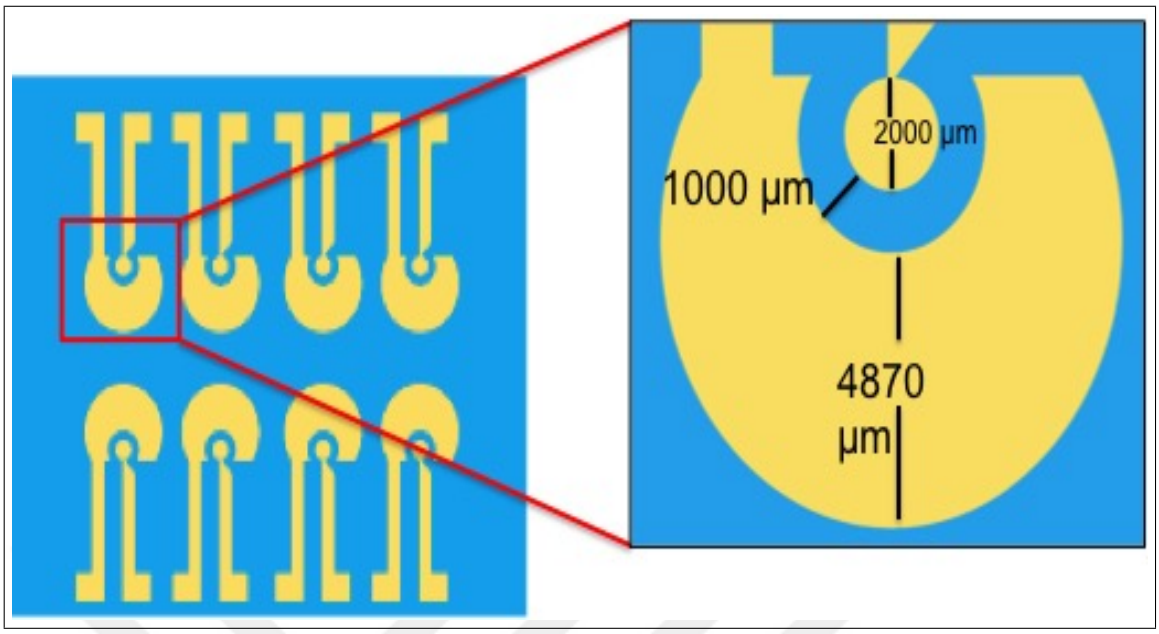

Figure 2.2 EIS sensor C and electrode dimensions. Each sensory surface consisted of 8 wells. The diameter of the smaller working electrode was 2000 μm. The gap between the working electrode was 1000 μm and the maximum diameter of the counter electrode was 4870 μm (The Figure was used by Simsek et al in [11]).

steps are shown in a schema seen in Figure 2.3. The electrode is dried and the working

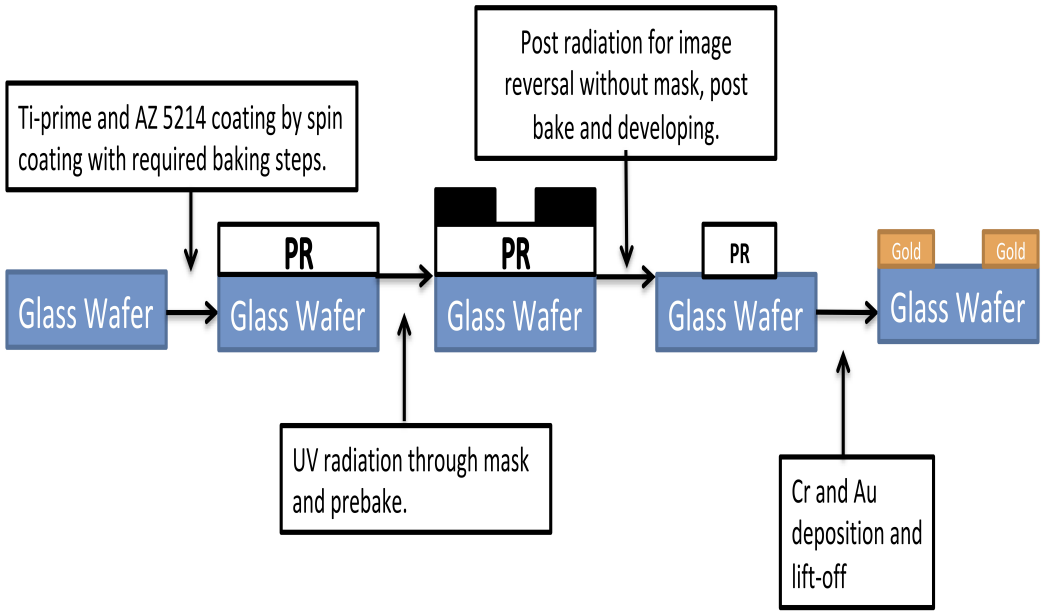

Figure 2.3 The schema of photo-lithography process for EIS production consisting of a 200 nm gold (Au) layer on chromium (Cr) (60 nm coated on glass wafer. PR refers to AZ5214 photoresist (The Figure was used by Simsek et al in [11]).

area of the electrodes for cell seeding are covered with ibidi 8 well sticky slides (ibidi

GmbH, cat no. 80828) as seen in Figure 2.4. In order to connect to EIS sensor to the instrument, nichrome wires were adhered to the connection pads using silver epoxy (SRA:40-3900) as seen in Figure 2.4.

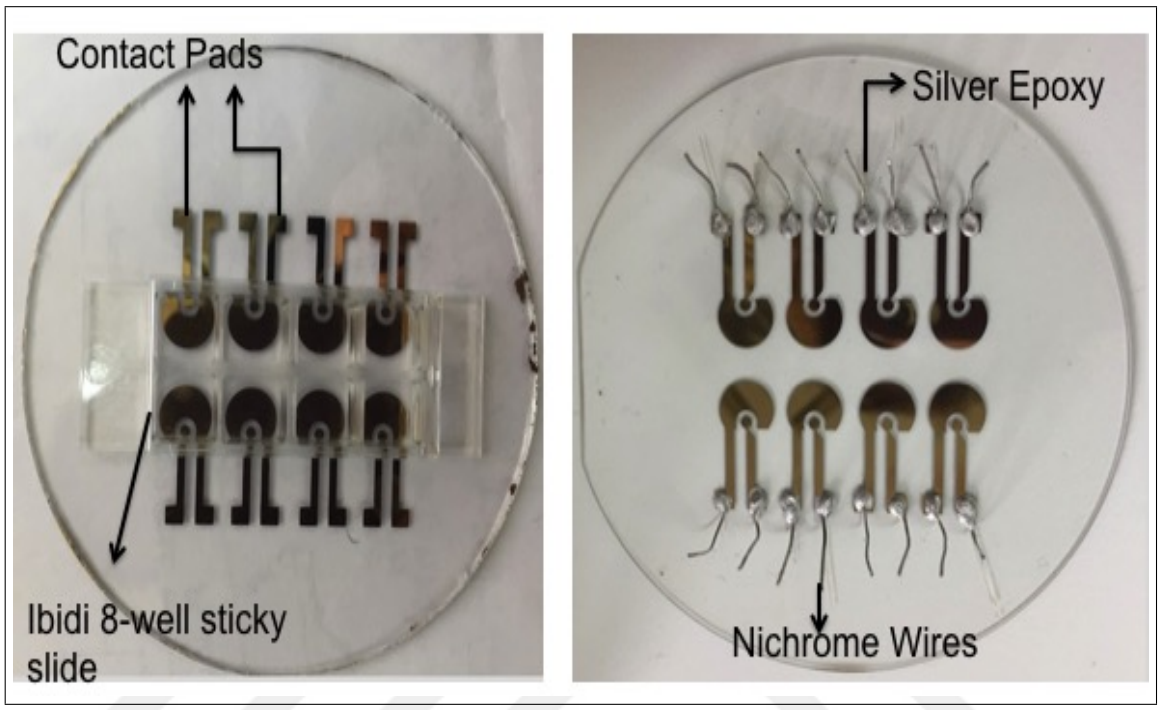

Figure 2.4 EIS sensor C with a) ibidi sticky slides and b) nichrome wires connected to the contact pads through silver epoxy.

2.2 SAM formation on Au surface, GO immobilization, and reduction of GO

Self assembly mono-layer (SAM) method was used for GO immobilization on Au surface. Hydrazine vapor reduction was performed in order to obtain rGO surfaces. Au surfaces coated on the glass wafer were used as substrate material for GO coating. The substrates were cleaned by UV-ozone treatment for 10 min [97]. In order to remove oxygen molecules from the surface and to stabilize it, the substrates were incubated in ethanol for 10 min [98, 99]. Following ethanol incubation, the substrates were cleaned with ethanol and dI H_2O and then incubated in 10 mM of Cysteamine.HCl (M6500, Sigma-Aldrich Inc., USA.) solution in ethanol for 4 h. The self assembled

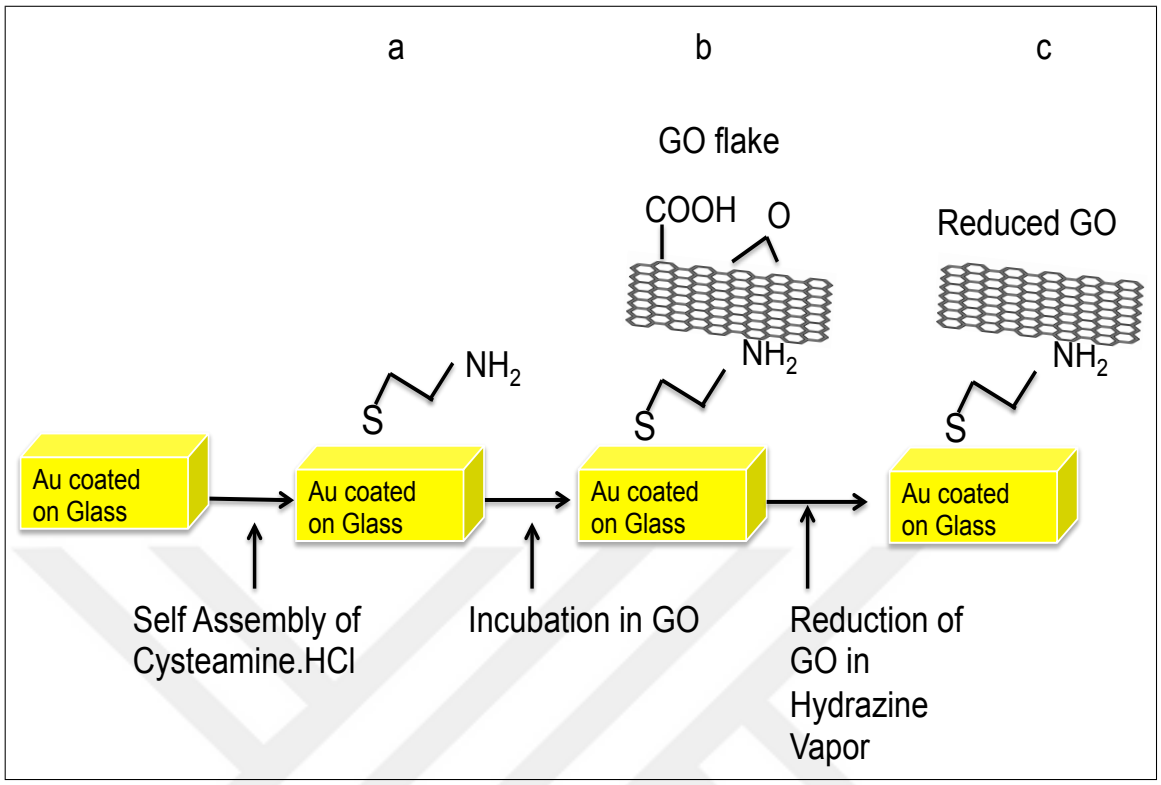

Figure 2.5 Schema showing the process of surface modification. (a) Cysteamine immobilization on the Au surface. (b) GO flakes attached to the surface through amine groups of cysteamine. (c) GO reduction through hydrazine vapor reduction process (Hydrazine vapor at 40 °C) (The Figure was used by Simsek et al in [11]).

cysteamine (Cys) on the Au surface was the linker molecule between Au and GO [100]. 0.5 mg/ml aqueous GO (2 mg/ml, Sigma- Aldrich Inc., USA) solution was sonicated for 15 min in order to form graphene flakes. The immobilization of GO on the Au surface through cysteamine molecule was achieved by incubating the substrates in 0.5 mg/ml sonicated aqueous GO solution for 1 h. Following the rinsing, Au/GO surfaces were dried with N2 gas. As the reduction process, exposing GO to hydrazine vapor was chosen [101]. The substrates were incubated in hydrazine monohydrate vapor (95% purity, Sigma-Aldrich). Au/GO surfaces were left in a sealed chamber with hydrazine monohydrate to obtain Au/rGO surfaces. The chamber was placed on a hot plate at 40°C temperature. To achieve gradual reduction steps, the substrates were left in the chamber for increasing time intervals, from 2 to 22 h. The steps for modification are shown in Figure 2.5.

2.3 Surface Characterization

The characterization of the surfaces were performed through SEM, water contact angle (WCA) measurements and EIS analysis.

2.3.1 Scanning Electron Microscopy

The SEM images were obtained by Philips XL30 ESEMFEG/EDAX at Boğaziçi University Advanced Technologies Research & Development Center. Au and Au/Cys.HCl surfaces are shown in Figure 2.6.

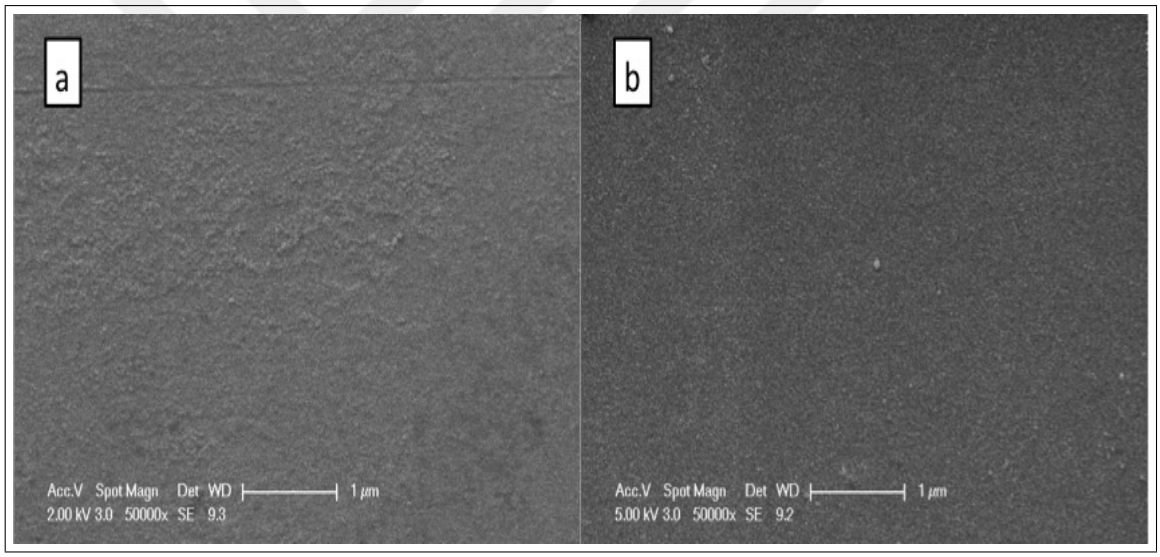

Figure 2.6 SEM image of a) Au surface on glass wafer coated by soft lithography method, b) Au/Cys.HCl surface, $5X10^4$ magnification. Scale bars show 1 μm.

The morphology of the flakes in GO surfaces seen in Figure 2.7 show that GO flakes had been achieved (Figure 2.7b with $2X10^4$ magnification) and the flakes uniformly distributed through the surface with no aggregation (Figure 2.7a).

The reduction was performed by incubating the Au/GO samples under the hydrazine vapor for gradually increasing time duration, Au/rGO-2hrs, Au/rGO-4hrs, Au/rGO-6hrs, Au/rGO-12hrs, Au/rGO-18hrs, Au/rGO-22 hrs are seen with $5X10^3$

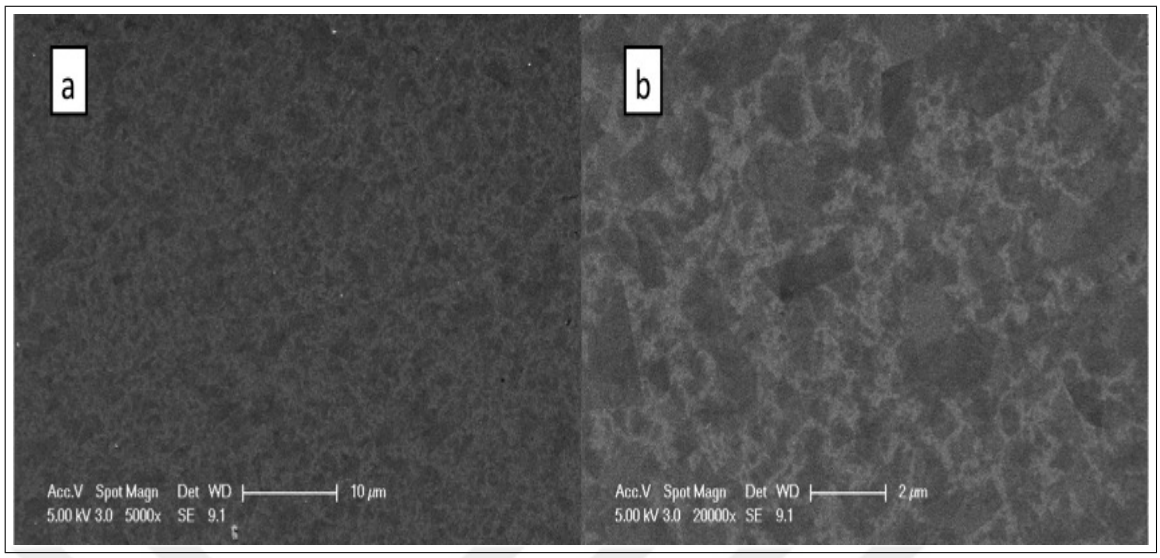

Figure 2.7 SEM image of GO with magnification a) $5x10^3$ magnification, scale bar shows 10 μm and b) $2X10^4$, scale bar shows 2 μm.

magnification in Figure 2.8. It is seen that the reduction process did not cause any visible damage on the surface.

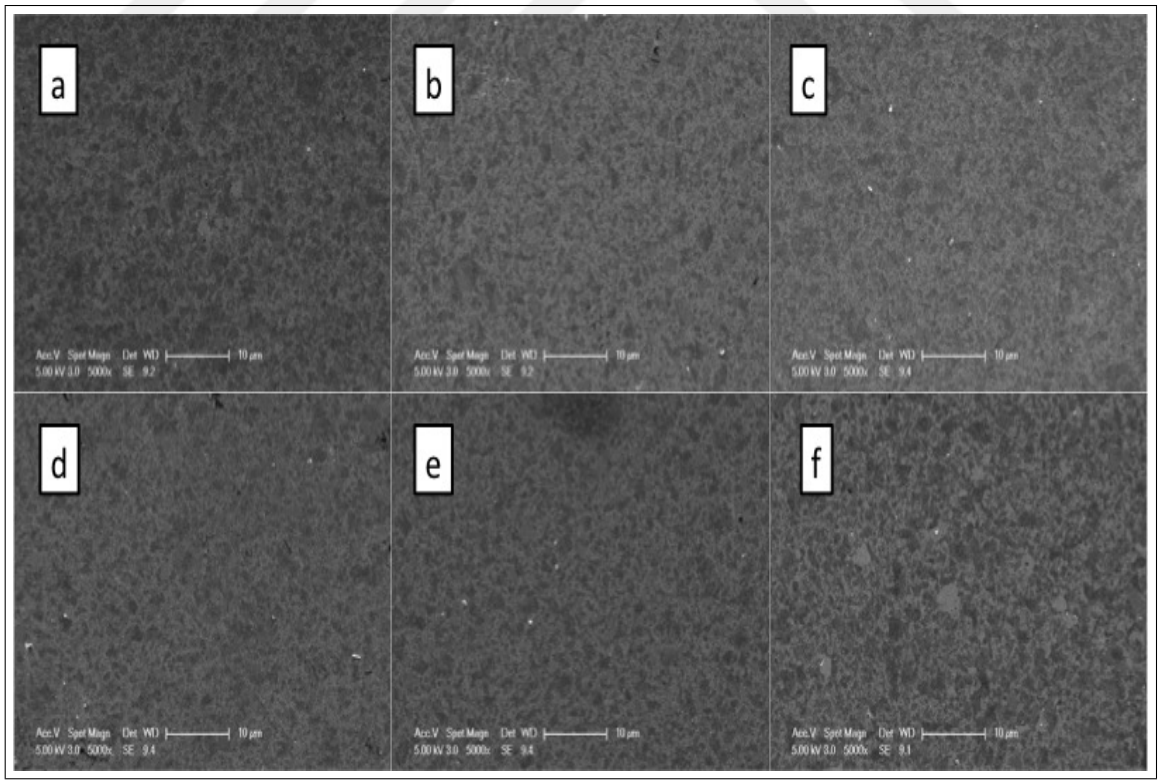

Figure 2.8 SEM image of a) Au/rGO-2hrs, b) Au/rGO-4hrs, c) Au/rGO-6hrs, d) Au/rGO-12hrs, e) Au/rGO-18hrs, f) Au/rGO-22hrs surfaces with $5X10^3$ magnification. Scale bars show 10 μm.

In order to compare the conditions of the flakes visually before and after reduction process; Au/GO, Au/rGO-2h and Au/rGO-22 h are displayed in Figure 2.9 with a magnification of $5X10^4$.

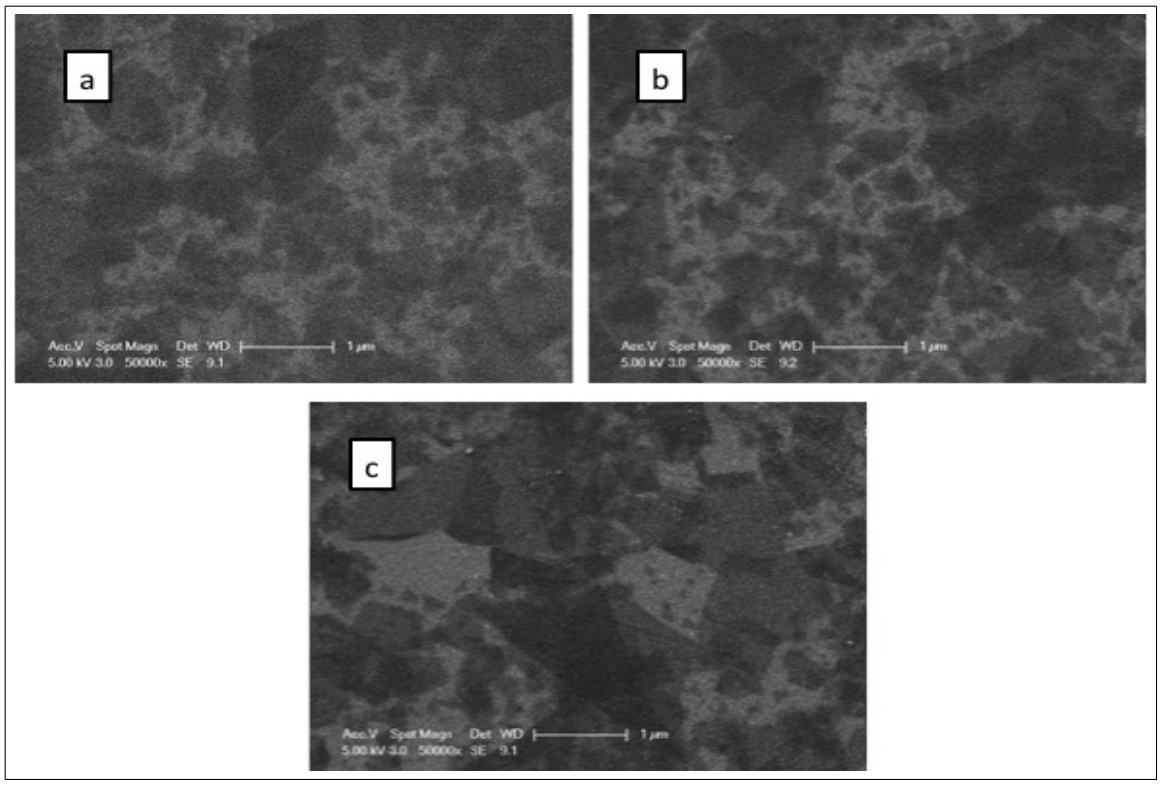

Figure 2.9 SEM images from a) Au/GO, b)Au/rGO-2h, c)Au/rGO-22h surfaces, with $5X10^4$ magnification. Scale bars show 1 μm.

2.3.2 Water Contact Angle Analysis

The knowledge about the hydrophilicity and the hydrophobicity of the Au, Au/GO and Au/rGO surfaces were obtained by water contact angle analysis (WCA). The WCA measurements were performed by CAM 100, KSV at Chemistry Department, Boğaziçi University. The representative water droplets on Au, Au/Cys.Hcl, Au/GO surfaces are seen in Figure 2.10 and on Au/rGO-2hrs, Au/rGO-4hrs, Au/rGO-6hrs, Au/rGO-12hrs, Au/rGO-18hrs, Au/rGO-22 surfaces in Figure 2.11.

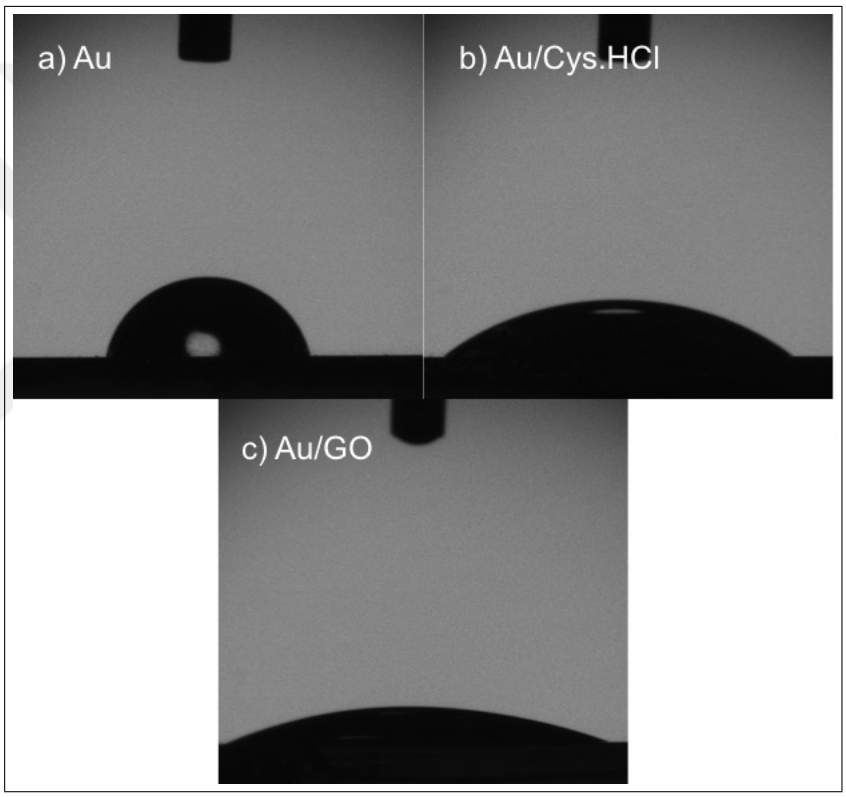

Figure 2.10 Water droplet on a) Au, b) Au/Cys.HCl, c) Au/GO surfaces.

Water contact angle measurements from surfaces Au, Au/Cys.HCl, Au/GO, Au/rGO-2h, Au/rGO-4h, Au/rGO-6h, Au/rGO-12h, Au/rGO-18h, Au/rGO-22h are presented with mean values and standard deviations in Figure 2.12 Au surface had a relatively hydrophobic nature. In our study we obtained a WCA value of $69.75° \pm 10.03°$ (n=7) for Au; which is similar to the values present in the literature [102]. After the formation of the self-assembly of cysteamine HCl molecule on the gold surface, the WCA value was reduced to $53.06° \pm 8.76°$ (n=7) [103]. GO immobilization decreased

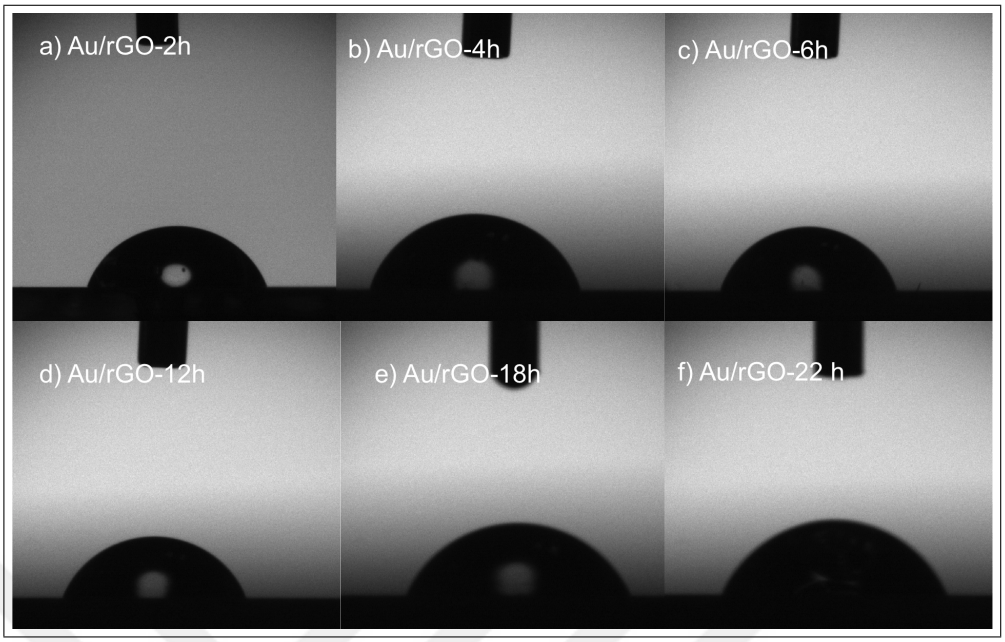

Figure 2.11 Water droplet on a) Au/rGO-2h, b) Au/rGO-4h, c) Au/rGO-6h, d) Au/rGO-12h, e) Au/rGO-18h, f) Au/rGO-22h surfaces.

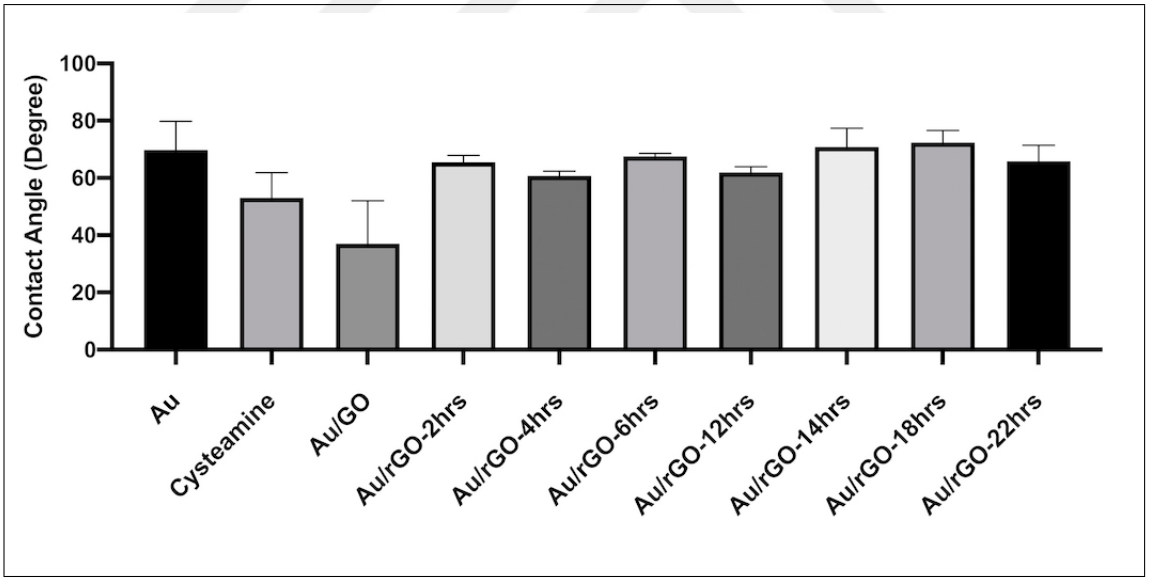

Figure 2.12 WCA values measured for Au, Au/Cys.HCl, Au/GO, Au/rGO-2h, Au/rGO-4h, Au/rGO-6h, Au/rGO-12h, Au/rGO-18h, Au/rGO-22h. Bars represent the mean values and error bars are for the standard deviations. The contact angle measurement was performed using CAM, 100, USA (The Figure was used by Simsek et al in [11]).

the contact angle to $35.99° \pm 15.04°$ (n=7) [104], resulting in a relatively hydrophilic surface. 2h reduction process increased the hydrophobicity of the surface corresponding to an angle $65.50° \pm 2.42°$ (n=7) [41]. Since there was no significant difference in water

contact angle value with incubation time, shorter duration was preferred. Thus, for carotid artery endothelial cell experiments Au/rGO-2h surfaces was chosen.

2.3.3 EIS for Surface Characterization

The EIS sensors A and B were used in order to measure the electrical response of the Au, Au/GO and Au/rGO surfaces. Redox probe, which is 0.1 M KCl solution containing 10 mM $K_3Fe(CN)_6/K_4Fe(CN)_6$, was used as the measurement solution. The Nyquist plots and Bode plots for Au and Au/GO surfaces with the Z and the impedance phase angle are seen in Figure 2.13. The EIS sensor B was used in order

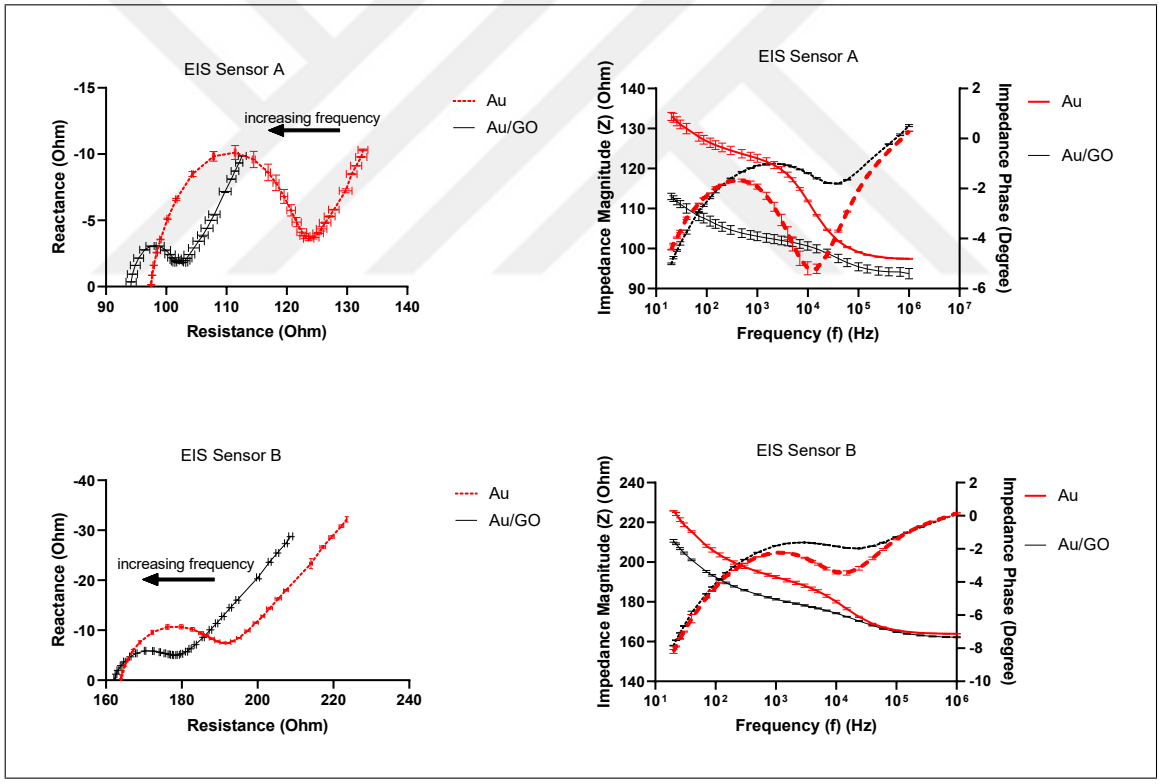

Figure 2.13 The electrical impedance response of 0.1 M KCl solution containing 10 mM $K_3Fe(CN)_6/K_4Fe(CN)_6$ measured with EIS Sensors A and B, between frequencies 100 Hz and 1 MHz is seen in a) Nyquist plot for EIS sensor A. b) Bode plot for EIS Sensor A. c) Nyquist plot for EIS sensor B. d) Bode plot for EIS sensor B.

to compare the electrical responses of Au, Au/GO and Au/rGO surfaces. For the Au, Au/GO and Au/rGO; Figure 2.14 shows the Nyquist plot and Figure 2.15 shows the Bode plots.

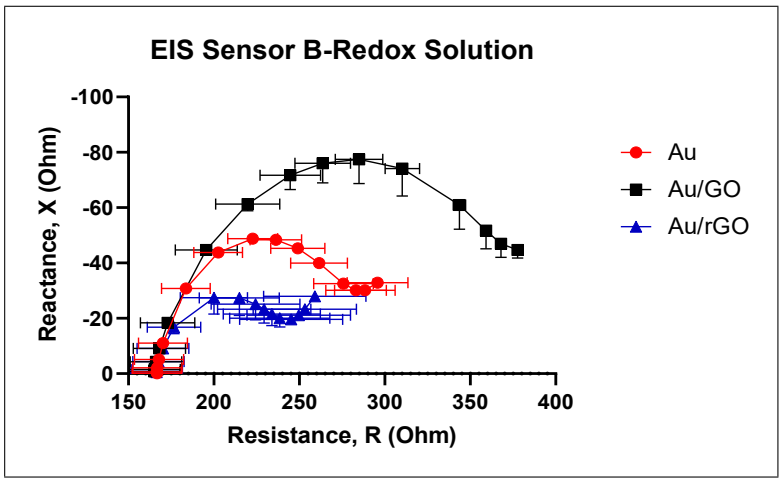

Figure 2.14 Nyquist plot of 0.1 M KCl solution containing 10 mM $K_3Fe(CN)_6$/ $K_4Fe(CN)_6$ measured with EIS Sensor B with Au, Au/GO and Au/rGO surfaces. The measurement frequency range was from 100 Hz to 1 MHz.

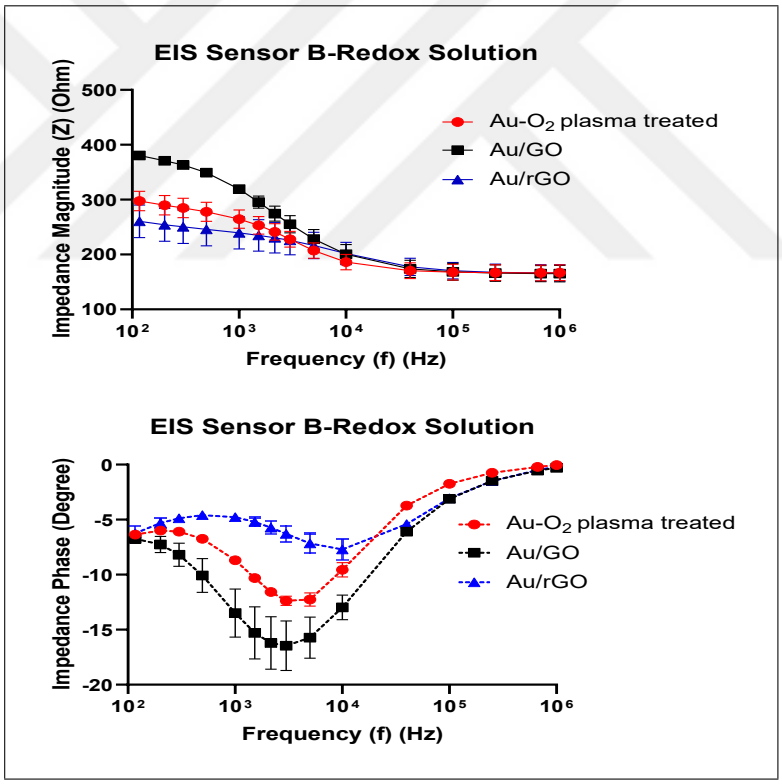

Figure 2.15 Bode plots a) with Z b) with impedance phase angle of 0.1 M KCl solution containing 10 mM $K_3Fe(CN)_6/K_4Fe(CN)_6$ measured with EIS Sensor B with changing frequency. The measurement frequency range was from 100 Hz to 1 MHz.

2.4 The Validation of the EIS Sensor C

The cell factor analysis were performed for varying concentrations of KCl solutions with EIS sensor C. The KCl concentrations of solutions used in the measurements

are listed in Table 2.1. The cell factor analysis were performed by dividing the measured impedance to the measured resistivity of the KCl solution. The resistivity of the solution was calculated through the conductivity measurements by conductivity meter. The impedance measured at 40 kHz frequency was used for the analysis shown in Figure 2.16.

Table 2.1
Conductivity values of KCl solutions with varying molarities.

Molarity (M)	Conductivity (mS/m)
0.1	12.1
0.05	6.15
0.025	3.25

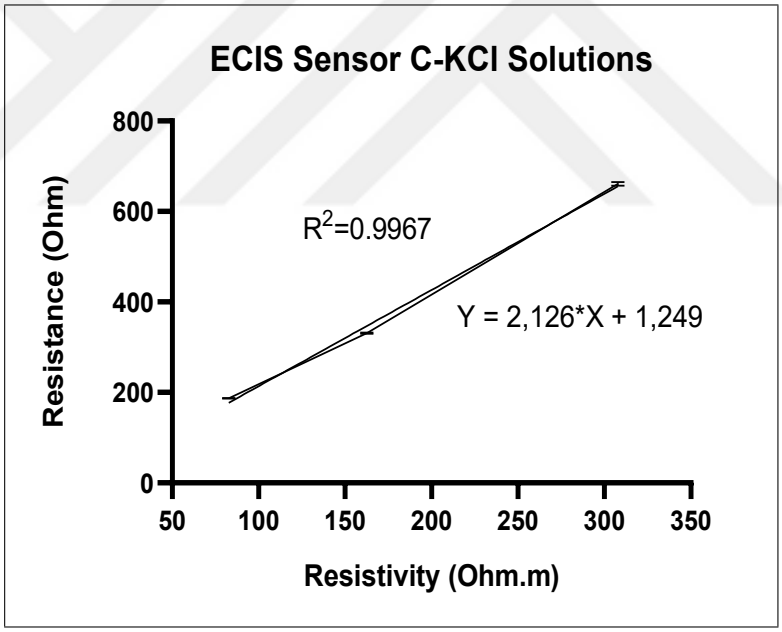

Figure 2.16 Linear regression of resistance and resistivity value of KCl solution. Resistance values were calculated through impedance measurements obtained by the LCR meter. Resistivity values were calculated through conductivity measurements obtained with the conductivity meter.

Measurement repeatability of the EIS sensor C was tested through the cell culture medium only measurements. The measurement was performed at 5 mV excitation voltage, within the frequency range from 100 Hz to 1 MHz (Figure 2.17). The standard deviations of Z and Θ values from multiple wells of the same chip (n=8) and from multiple wells of two chips (n=16) are seen in Table 2.2 and Table 2.3, respectively.

Table 2.2
Standard deviation of measured impedance (STD_Z (Ω)) and impedance phase angle (STD_Θ ($^\circ$)) from multiple wells of the same EIS C sensor (n=8).

	Multiple wells of the same chip					
	Au		Au/GO		Au/rGO	
Frequency	$STD_Z(\Omega)$	$STD_\Theta(^\circ)$	$STD_Z(\Omega)$	$STD_\Theta(^\circ)$	) $STD_Z(\Omega)$	$STD_\Theta(^\circ)$
1 kHz	7.24	0.82	4.21	0.94	25.61	2.90
4 kHz	3.83	0.44	0.90	0.48	18.84	0.69
5 kHz	3.65	0.39	0.91	0.41	17.49	0.72
10 kHz	3.30	0.26	0.98	0.26	14.13	0.93
20 kHz	3.09	0.17	1.05	0.17	11.57	1.00
40 kHz	2.97	0.11	1.13	0.12	9.70	0.99
100 kHz	2.91	0.06	1.21	0.07	7.75	0.94
200 kHz	2.79	0.04	1.24	0.04	6.48	0.89
350 kHz	2.76	0.03	1.28	0.03	5.66	0.84
1 MHz	2.75	0.03	1.27	0.03	4.23	0.67

Table 2.3
Standard deviation of measured impedance (STD_Z (Ω)) and impedance phase angle (STD_Θ ($^\circ$)) from multiple wells of the two EIS C sensors (n=16).

	Multiple wells of two chips					
	Au		Au/GO		Au/rGO	
Frequency	$STD_Z(\Omega)$	$STD_\Theta(^\circ)$	$STD_Z(\Omega)$	$STD_\Theta(^\circ)$	$STD_Z(\Omega)$)	$STD_\Theta(^\circ)$
1 kHz	7.75	1.34	18.75	3.40	24.61	2.58
4 kHz	3.40	0.73	2.95	2.08	15.03	1.32
5 kHz	3.21	0.64	2.22	1.82	13.87	1.24
10 kHz	2.89	0.41	1.29	1.15	11.06	1.09
20 kHz	2.72	0.24	1.40	0.66	8.99	0.99
40 kHz	2.61	0.13	1.54	0.32	7.50	0.88
100 kHz	2.51	0.08	1.51	0.08	6.02	0.76
200 kHz	2.41	0.07	1.42	0.08	5.11	0.67
350 kHz	2.37	0.08	1.37	0.10	4.59	0.61
1 MHz	2.36	0.14	1.28	0.10	3.72	0.47

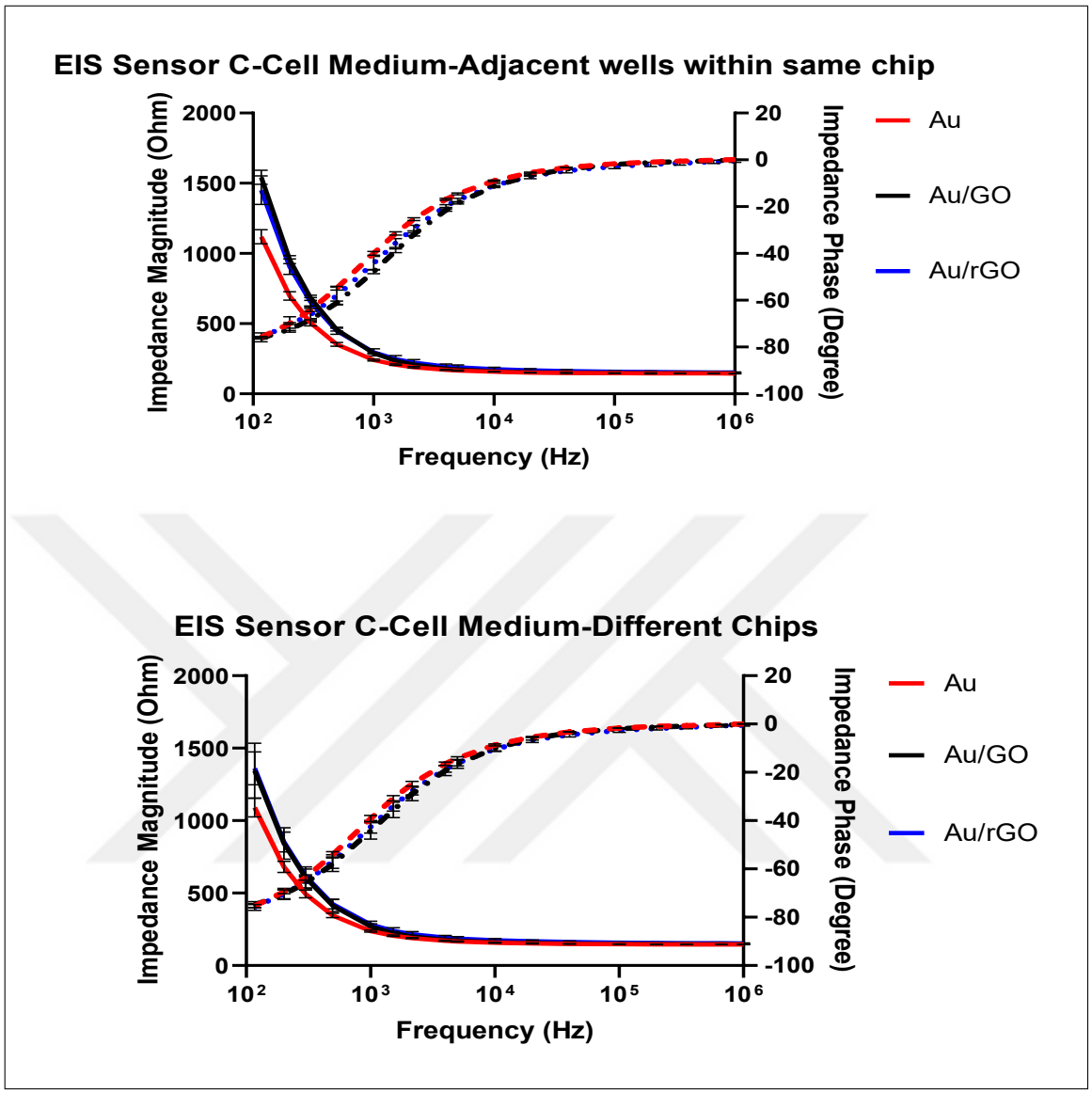

Figure 2.17 Bode plots for HCAtECs growth medium measured with EIS sensory surfaces for Au, Au/GO and Au/rGO. Error bars represent the standard deviations from measurements from the wells of the same EIS C (n=7) (up) and the from wells of two different EIS C (n=14) (bottom).

2.5 Preliminary Cell Culture Studies

EIS sensors A and B were used in order to test the measurement quality. L929 cell line and osteoblast cell line were used in the preliminary electrical analysis of cell proliferation 2.18. Figure 2.19 shows the fibroblast and osteoblast behaviour on EIS sensor B and HCtAECs behaviour on EIS sensor C. The normalization for impedance magnitude (Z) was calculated as in 2.1. The normalized value of Z is referred as relative change in impedance magnitude with respect to "No cell" condition as the

cells proliferate.

$$\mathbf{\Delta Z_{Day_x}}\% = \frac{\mathbf{Z_{cell_{Day_x}}} - \mathbf{Z_{Nocell}}}{\mathbf{Z_{Nocell}}} * \mathbf{100} \tag{2.1}$$

The phase angle correction was performed by subtracting the phase angle of the cell medium from that of following experimental day. The equation is 2.2.

$$\theta' = \theta_{\mathbf{Day_x}} - \theta_{\mathbf{Nocell}} \tag{2.2}$$

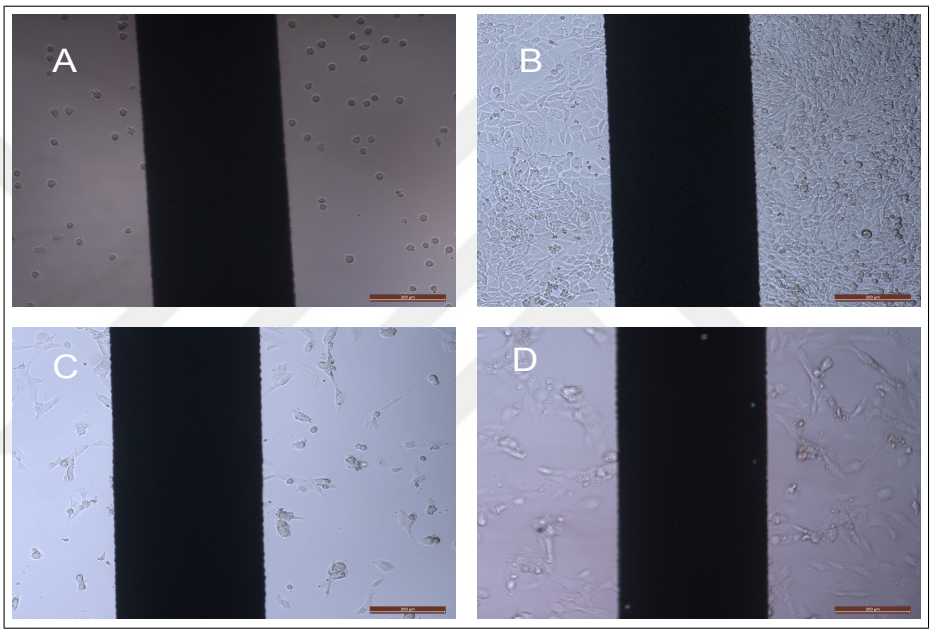

Figure 2.18 Fibroblast cell line on EIS sensor B on day 1 (A) and on day 8 (B). Osteoblast cell line on day 7 (C) and on day 11 (D).

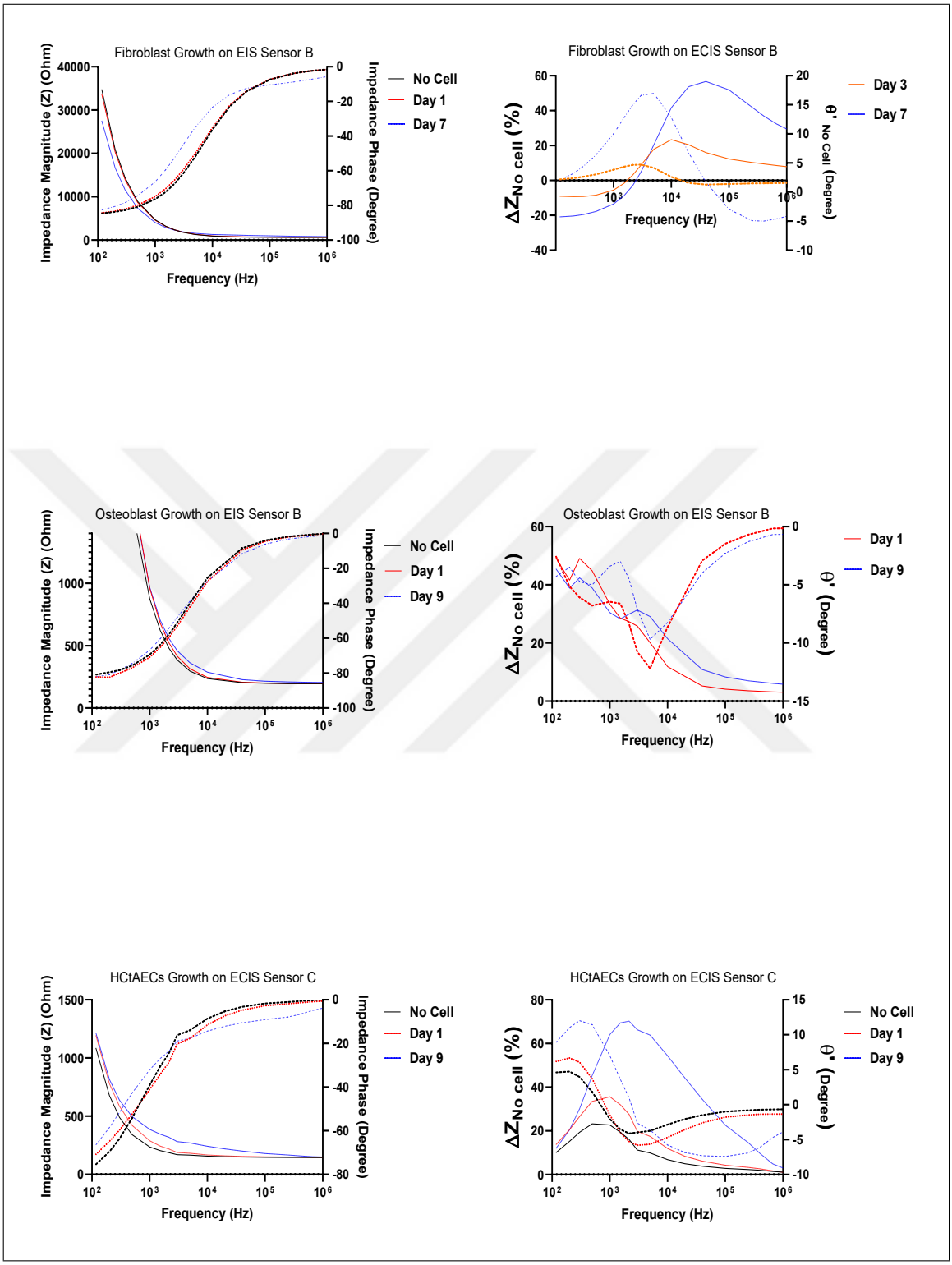

Figure 2.19 Z and Θ angle values for fibroblast (up-left), for osteoblast (middle-left) measured with EIS sensor B. Relative impedance change ΔZ_{NoCell} (%) and corrected phase angle (Θ').

2.6 Conclusion

The surface characterization through SEM images and WCA analysis verified that the modification was achieved. The WCA results consistent with the literature

and the SEM images, showed the presence of GO and rGO molecules on the Au surface. The results showed that gold surface had a hydrophobic nature. In an early study, gold evaporated on glass and sealed in a chamber had a water contact angle value of 90, then decreased to 10 with UV irradiation, then increased to 70 after 10 min of ethanol incubation. UV/ozone treatment removes organic contamination and oxidises the Au surface. Following, ethanol incubation reduces the gold oxide [98]. Those results are consistent with the thesis findings.

In our experiments, the contact angle value of rGO surface was measured to be similar to that of the gold, where GO had a lower contact angle value, i.e; more hydrophilic. This is a known fact that the GO is more hydrophilic than rGO, which is a form more similar to the graphene itself as mentioned in Chapter 1. The reason for the increase in the contact angle after the reduction process may be attributed to the reduction in oxygen functional groups that are high energy level-binding sites [12]. Thus by reducing the GO, the surface energy was lowered. Robinson et al studied the effect of reduction level to the surface chemistry of the rGO. They showed that the increase in exposure time to hydrazine vapor decreased the high-energy binding sites [71]. In this thesis, although incubation time did not significantly alter the water contact angle results, there was a slight increase with incubation time. SEM images of GO coated Au surface and rGO showed the uniform distribution of the flakes. The curtain-like structure confirms the flake formation. There was no visible aggregation of the flakes. For electrical contributions of GO and rGO coated Au and bare Au electrodes, frequency dependent measurements were performed. To characterize electrical impedance of the three electrode surfaces used (Au, Au/GO and Au/rGO), the redox solution, 0.1 M KCl solution containing 10 mM $K_3Fe(CN)_6/K_4Fe(CN)_6$ was used as the measurement solution. This is the redox probe used commonly in the literature for electrode characterizations [105, 106]. Results showed that at lower frequencies the electrical impedance of Au was larger than the Au/GO (Figure 2.13). In order to compare electrical characteristics of Au/rGO, EIS sensor B was used after O_2 plasma treatment (Figure 2.14 and Figure 2.15). O_2 plasma reduced the impedance value of gold surface. (The surface also became highly hydrophilic with O_2 plasma treatment, not shown in here). Thus Au/GO had larger impedance value than Au-O_2 plasma

treated electrode. Au/rGO had the lowest impedance value. These results are consistent with the literature since rGO has lower impedance values (higher conductivity) compared to GO; Xu et al showed that rGO was more conductive than GO (300 to 105 fold depending on the reduction process) [101]. The reason of higher impedance values of Au/GO surface is because oxidized components of the GO surface decrease the electrical conductivity, as mentioned in Chapter 1. Another study by Zong and coworkers showed that GO coating on Au surface increased impedance values and the reduction of GO rendered a decrease in impedance [107, 108]. However these electrode characteristics contribute to the electrical measurements at lower frequencies. The impedance values decrease with increasing frequency and both the impedance and phase angle converged to similar values for Au, Au/GO and Au/rGO surface; the converged value is supposed to be the resistance of the cell culture medium. At higher frequencies, the electrode impedance vanishes and the electrical characteristics of the solution or analyte dominates. Electrical characteristics of the electrodes were shown in the literature with redox solutions [109]. However cell proliferation measurements were performed in cell growth medium. The Bode plots of cell culture medium measured with EIS sensor C showed no significant difference in the magnitude and distribution of Z and Θ (Figure 2.17). The cell culture medium is the solution in which "No cell" measurements were performed. In addition to the similar electrical response of Au, Au/GO and Au/rGO with cell culture medium, any possible variations due to electrode surface can be eliminated with normalization process. Normalization with respect to cell medium is a common step in EIS analysis for cell behaviour [94]. Also in order to stabilize the surfaces, the electrodes were incubated in the growth medium for 24 hours and then the medium was changed prior to "No cell" measurement. Lastly, in our study, we performed statistical analysis at frequencies, above 4 kHz, the ranges used in the literature for impedance monitoring of cells [81, 94, 110, 111]. Above this frequency range the electrode polarization impedance vanishes. The sensor reproducibility were examined through standard deviations for Au electrode surface on EIS sensor C. The measurements were performed from all eight wells of the same sensor and from sixteen wells of the two different sensor with cell medium. In Table 2.2 and Table 2.3, the standard deviations show that the electrical response of the sensors are similar to each other for cell medium. Thus, the measured impedance changes would be regarded

as because of the cell adhesion and proliferation at larger frequencies. In a recent study, three-dimensional conformation of graphene was used as an interface for the EIS measurements. Although the graphene had contribution to their electrical model, they analyzed the results with change in impedance from the previous measurement day [112].

The preliminary cell culture studies with EIS sensors A, B and C verified the systems availability for monitoring cell behaviour in constructed experimental set-up (Figure 2.19). There was significant increase in impedance with cells on the electrode.

3. ANALYSIS FOR HUMAN CAROTID ARTERY ENDOTHELIAL CELL PROLIFERATION ON ELECTRODE SURFACES

3.1 Materials and Method

3.1.1 Cell Culture

HCtAEC (Cell Applications Inc., CA-USA) were seeded in T25 cell culture flasks (Corning, USA) and allowed for growing under the conditions of 5 % CO_2 and 95 % air at 37.0 °C. Human Meso-Endo Growth Medium (212-500, Cell Applications Inc., CA-USA) was used as cell growth medium as suggested in the protocol [113]. The medium was refreshed every other day until the cells achieved confluence. Prior the cell seeding, the EIS sensors were sterilized by rinsing with 70% ethanol and then by exposing to UV light for 30 min. In order to seed the cells onto the EIS sensors, they were trypsinized with 0.25 % trypsin-EDTA solution (Sigma, St. Louis, MO, USA). 5000 HCtAECs, between passages 5-8 were seeded in each well in 300 μl growth medium.

3.1.2 Electrical Impedance Measurements

Impedance spectroscopy analysis was performed with an HP 4284A LCR meter. The connections between surface electrodes and the LCR meter were achieved through Kelvin clips. The experimental set-up is seen in Figure 3.1. The measurements were performed between frequencies 100 Hz and 1 MHz, at 5 mV excitation voltage. Z and phase angle values were recorded in the measurements. Three consecutive measurements were performed for each well. The average of three measurements were used in the analysis. After the sterilization process of the EIS sensor, 300 μl of cell medium was added on each electrode. The sensors were placed in the incubator and incubated

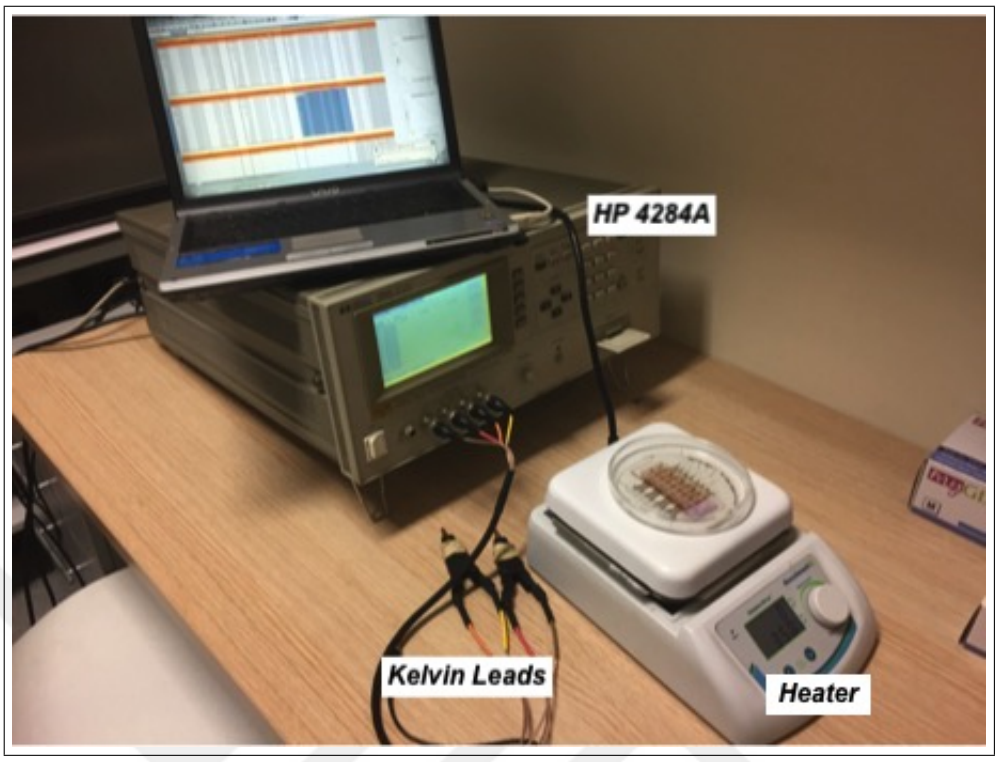

Figure 3.1 Experimental EIS set-up for measuring cell proliferation on EIS sensor.

for a day prior to the measurements. In the electrode fabrication processes, consecutive 70 % ethanol washes and UV light for sterilization may cause variations in the surface electrical properties. In order to stabilize the surfaces, one day incubation in cell medium was performed. After the incubation process, the cell medium was aspirated and 300 μl fresh medium was added into each well. Initially, electrical measurements were performed for the medium only, which was then used in calculating the electrical parameters. The medium only measurements were referred to as "No cell" conditions. Following the no cell measurements, the cell medium was aspirated and then, the cells were seeded on each well, in a 300 μl cell culture medium. The electrodes were then placed in the incubator and the cells let for adhesion for overnight. The next day, prior to electrical measurements, the medium was aspirated and 300 μl fresh medium was added on each well. The measurements were repeated on day 3, day 5, day 7, day 9 and day 10 of the experiment, each time by refreshing the medium. In order to eliminate temperature effects on the electrical measurements and keep cells at incubation temperature, electrode plates were kept on a hot plate at 36.0°C and the room set to 24.0 °C. The temperature was checked using the Raytek thermometer.

3.1.3 Optical Images of HCAtECs on Au, Au/GO and Au/rGO electrodes

The cells were imaged under a Nikon Eclipse LV150 microscope and HIROX on day 1, day 3, day 5, and day 10. For counting analysis, a specific area was chosen on the working electrode of each well. The reason is that, the contribution of a small working electrode on the electrical signal was expected to be higher, compared to counter electrode. 12 samples for each electrode surfaces were used for cell count analysis. The ImageJ program was used to manually count the cells from images.

3.1.4 Alamar Blue (AB) cell viability assay

In order to determine cell viability, AB assay (Bio- Rad, Inc.) was performed to examine the cell viability on Au, Au/GO, and Au/rGO surfaces. As testing protocol suggested, 10% of the cell culture medium, which was 30 μl, AB solution was added onto the EIS sensors containing cell media. 30 μl of AB solution was also added into 300 μl of cell medium which is placed in tissue culture plate (TCP) for calculation of AB reduction value. The sensors and the cell medium with AB solution containing medium were then placed in a humidified environment of 5 % CO_2 and 95 % air, at 37.0 °C and incubated for 3.5 h. After the incubation period, 100 μl of the AB containing cell culture medium from each sample including the control was transferred to the 96-well plates. Absorbance was measured with 100 μl volume samples, at 570 nm and 595 nm wavelengths, by using a microplate reader (Bio-Rad Mark, Microplate Reader, USA).

3.1.5 Immunostaining with 4', 6-diamidino-2-phenylindole (DAPI) and F-actin

At the last day of the cell incubation period, day 10, immunostaining with DAPI (Thermo Fisher Scientific) and Alexa Fluor 488 Dye (Invitrogen) were used. Since the dyes are toxic, the cells need to be fixed prior to staining. As a first step of the fixation

process, the cell medium was removed and washed twice with PBS. Then, 100 μl of 4 para-formaldehyde solution in PBS with a pH level of 7.3 were added onto it and incubated with the adherent cells, for 10 min. The incubation of the samples was on a gentle shaker at room temperature. The fixing solution was then removed and the samples further washed twice with PBS. Later, 100 μl of 0.1 % TritonX solution in PBS was added onto the samples, and the samples were incubated for 5 min. The samples were then rinsed again with PBS twice, prior to the incubation with 100 μl of 1 % bovine serum albumin (BSA) in PBS with 0.1 % Tween 20. As a last step of fixation, the samples washed with PBS twice. For staining, the fixed cells were stained with Alexa Fluor 488 and DAPI [114,115]. The staining solution of Alexa fluor 488 (100 μl), prepared with 15 μl of phallotoxin per milliliter of 1 % BSA solution in PBS, was added to the fixed cells. After the incubation of the dye added samples at room temperature for 20 min in the dark, on a gentle shaker, the staining solution was aspirated. Then, rinsing samples twice with PBS was performed. The cells were stained with DAPI. DAPI stock solution was prepared prior to the experiment. DAPI was dissolved in methanol according to the manufacturer's protocol. 2.1 μl solution in methanol was diluted with 100 μl of PBS. In order to obtain staining solution, this stock solution was again diluted 1:1000 in PBS. 100 μl of DAPI staining solution was added onto the cells and incubated for 3 min, in the dark, on a gentle shaker. DAPI solution was then removed and the samples were washed with PBS twice. The stained cells in 100 μl of PBS were then imaged under a fluorescence microscope (DMIL, Leica, Germany) with blue filter for F-actin and violet filter for DAPI.

3.1.6 Acridine Orange (AO) and Propidium Iodide (PI) Staining for Cell Viability

AO and PI are dyes that bind to nucleic acid. AO can penetrate through both the living cells and dead cells whereas PI can only enter dead cells. AO stains all cells and generates a green fluorescence. For the staining protocol, 1 μl stock solution was dissolved in 1 ml PBS solution. The stock solution was 5 mg/ml AO in ethanol and 3 mg/ml PI in ethanol. On day 3 of the incubation, 1 μl of staining solution was added on

HCAEtCs. The samples were gently shaked and than the staining solution aspirated. Since dyes are toxic to cells, each sample was stained prior to imaging. Fluorescent images were obtained by using Leica fluorescence microscope (DMIL, Leica, Germany) using green filter.

3.2 Results for HCtAECs Proliferation on Au, Au/GO and Au/rGO Surfaces

3.2.1 EIS Analysis Results

The electrical measurements, i.e. EIS analyses were performed with 5 mV AC excitation voltage, between frequencies 100 Hz and 1 MHz for monitoring the behavior of the HCtAECs cultured on sensory surfaces. Results are shown with Bode plots of Z, Θ, corrected phase angle and normalized impedance with respect to cell medium and day 1. Normalized impedance parameters were calculated to compare the electrical characteristics of the cells on Au, Au/GO, Au/rGO and electrodes. These normalized values were interpreted as the relative changes in impedance. Relative impedance changes with respect to cell medium (i.e., no cell condition (ΔZ_{NoCell} (%)) were calculated from Eq. 2.1. On the other hand, relative changes in impedance with respect to Day 1 (ΔZ_{Day_1} (%)) was calculated from Eq. 3.1:

$$\mathbf{\Delta Z_{Day_1}} = \frac{\mathbf{Z_{cell_{Dayx}} - Z_{Day1}}}{\mathbf{Z_{Day1}}} * \mathbf{100} \tag{3.1}$$

A typical example for electrical response of HCtAECs proliferation on Au, Au/GO and Au/rGO electrodes is seen in Figure 3.2. Impedance characteristics of HCtAECs on Au, Au/GO, Au/rGO surfaces from two different wells from day 1 to day 10 are seen in Figures 3.3 and 3.4. Results showed that, as the cells proliferate on the electrode, Z increased, as expected. The mean Z and the phase angle of six wells are presented in Figure 3.5.

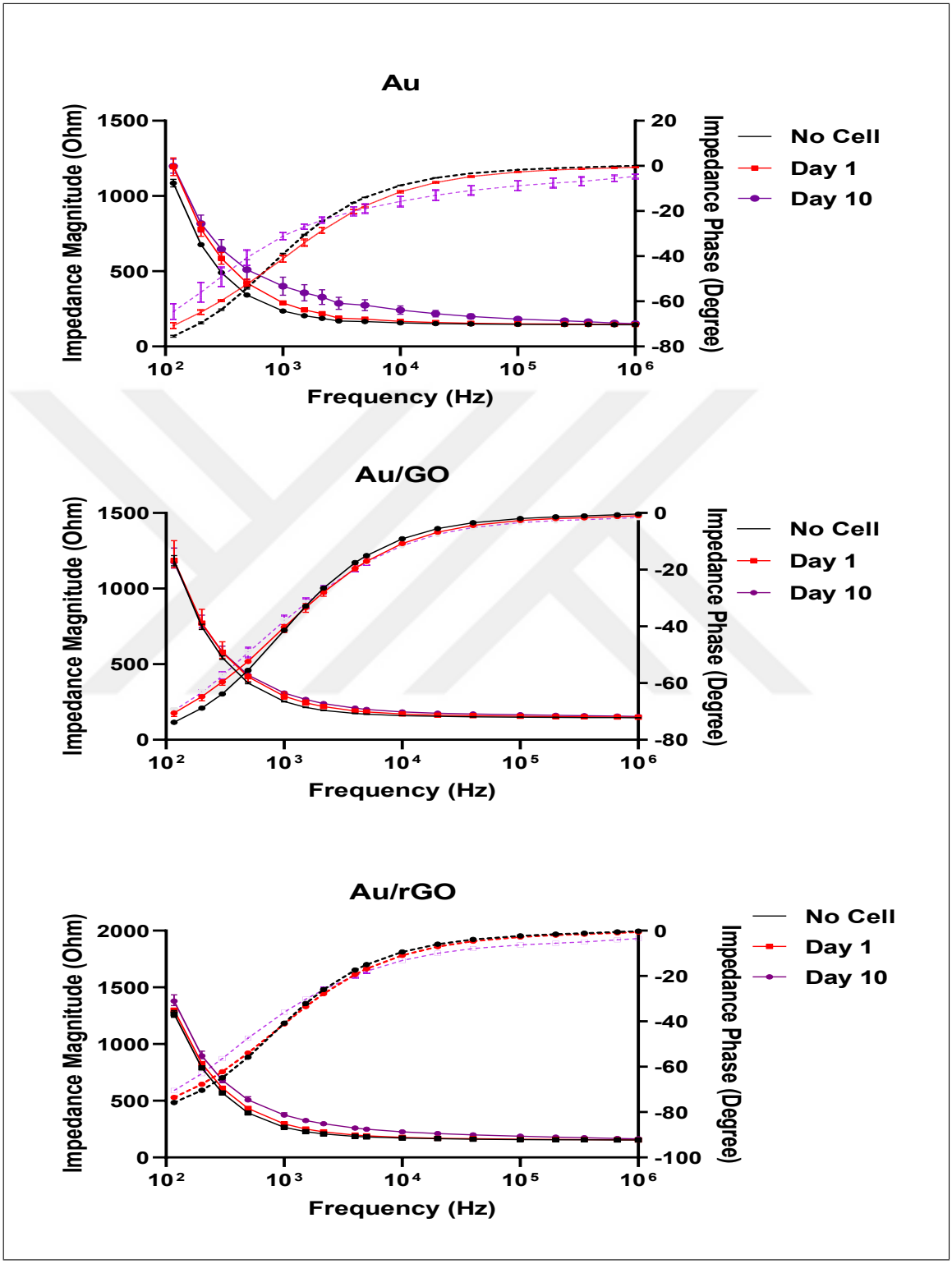

Figure 3.2 Representative Bode plots of HCAtECs proliferating on Au, Au/GO and Au/rGO electrodes from no cell, day 1, and day 10. Error bars stand for multiple measurements from the same well of EIS C sensor.

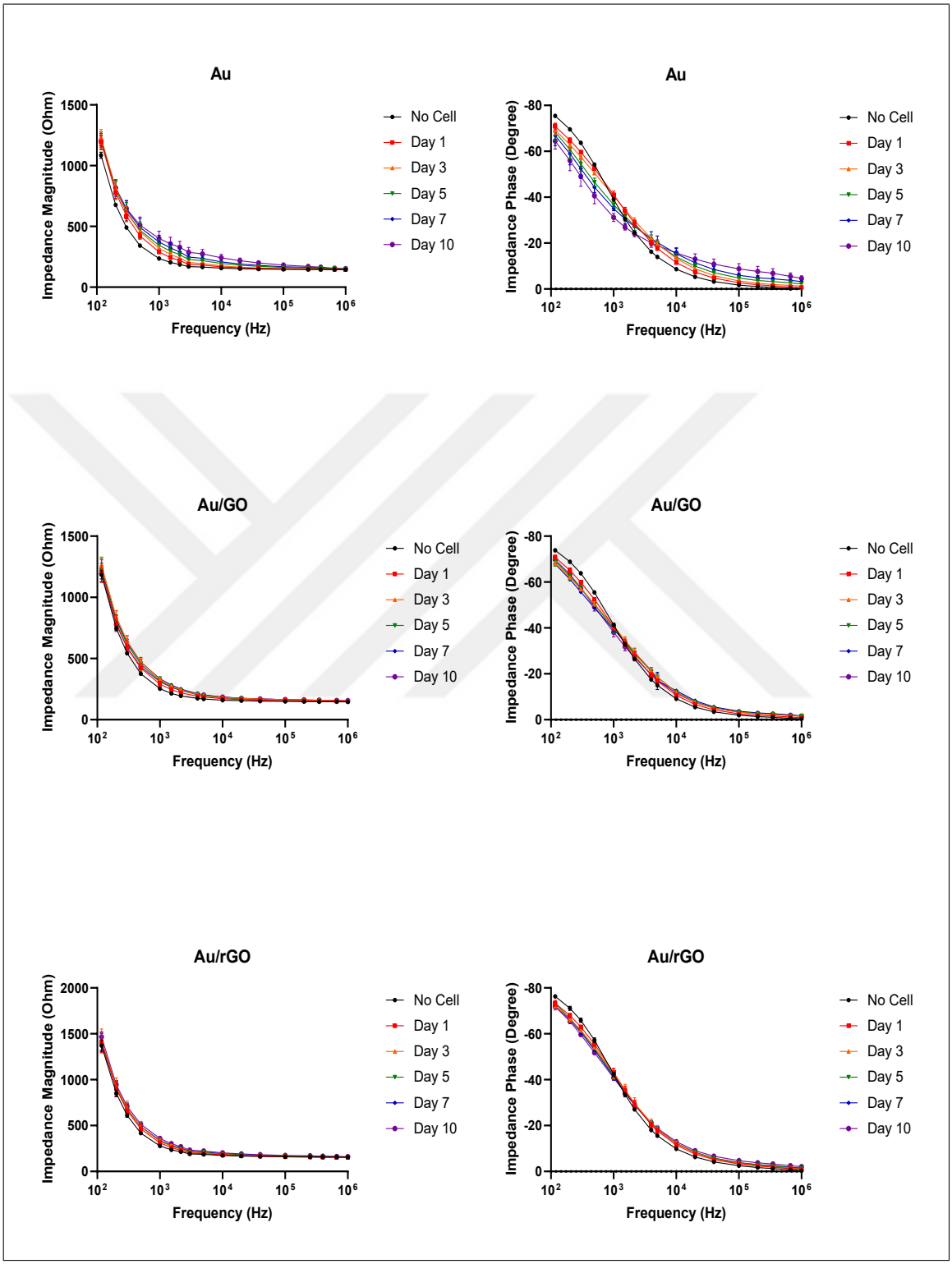

Figure 3.3 Representative Bode plots (Z and Θ with respect to frequency) of HCAtECs proliferating on Au, Au/GO and Au/rGO electrodes from no cell, day 1, day 3, day 5, day 7 and day 10. Error bars stand for standard deviations (n=6).

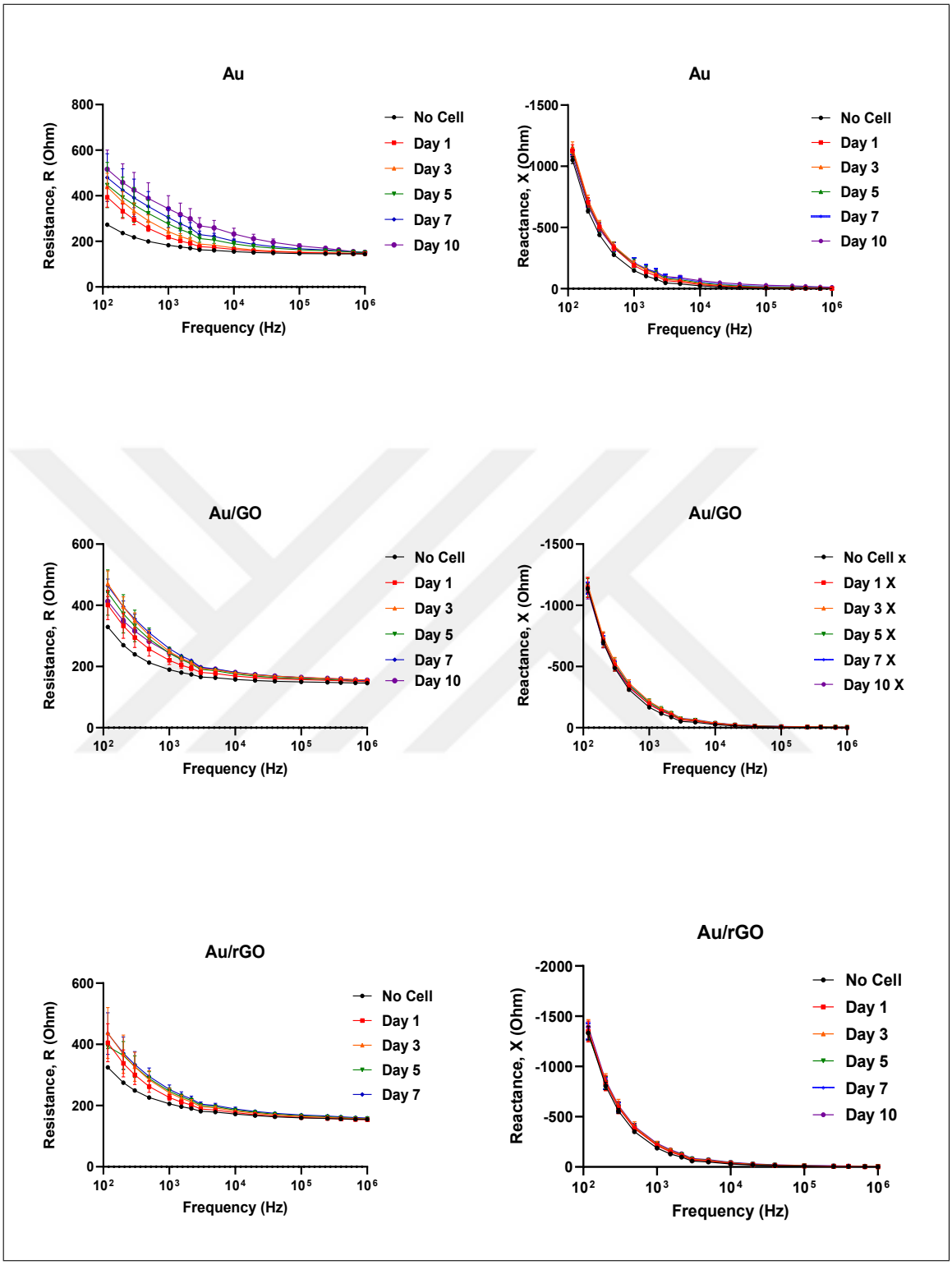

Figure 3.4 Representative Bode plots (Resistance and reactance with respect to frequency)of HCAtECs proliferating on Au, Au/GO and Au/rGO electrodes from no cell, day 1, day 3, day 5, day 7 and day 10. Error bars stand for standard deviations (n=6).

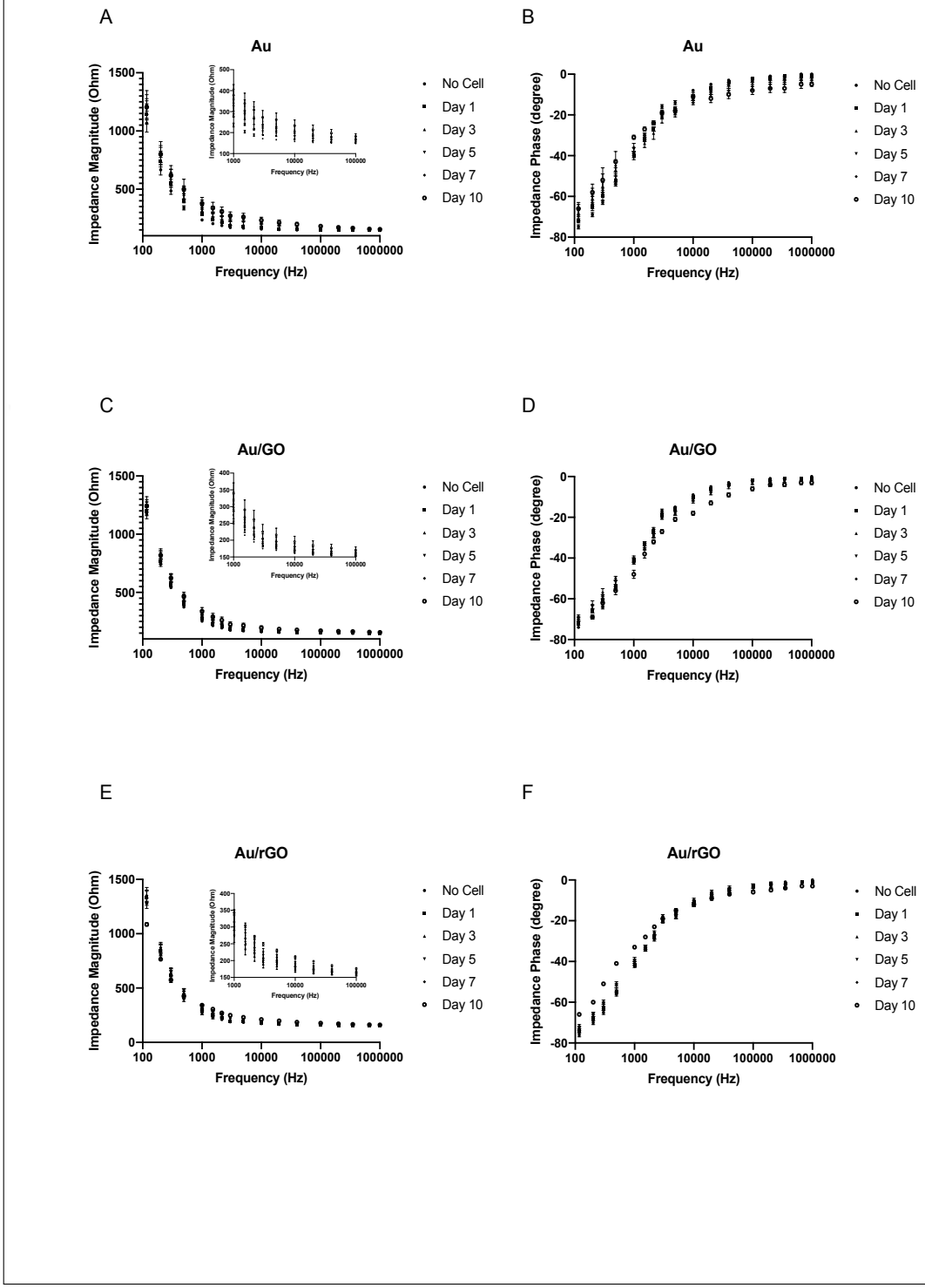

Figure 3.5 Impedance measurements as a function of cell incubation periods for each type of electrode surface (Au, Au/GO, Au/rGO) from "No Cell" to Day 10 (n=6). Data points represent the mean values of Z, with standard deviations in (A) for Au, (C) for Au/GO and (E) for Au/rGO. The frequency scans were from 100 Hz to 1 MHz in the outer; from 1 kHz to 100 kHz in the inlet graph. Phase angle mean values with standard deviations in (B) for Au, in (D) for Au/GO and in (F) for Au/rGO (n=6).

Statistical analyses were performed for the corrected phase angle (Θ'), impedance change rates from no cell (ΔZ_{NoCell} (%)) and from day 1 (ΔZ_{Day1} (%)). GraphPad Prism version, GraphPad Software, La Jolla California USA, (www.graphpad.com) was used for statistical comparisons. Kruskal wallis and Dunn's post hoc test were performed for all comparisons. The ΔZ_{NoCell} (%) for frequencies 4 kHz, 5 kHz, 20 kHz, 40 kHz, 100 kHz, 200 kHz, 350 kHz and 1 MHz with statistical results are shown in Figure 3.6. ΔZ_{Day1} (%) graphs for Au, Au/GO and Au/rGO surfaces are shown in Figure 3.7 with statistical results. Θ' values were used in the analysis as described in Eq. 2.2. The corrected phase angle graphs for frequencies 4 kHz, 5 kHz, 20 kHz, 40 kHz, 100 kHz, 200 kHz, 350 kHz, 1 MHz are shown in Figure 3.8; with statistical results.

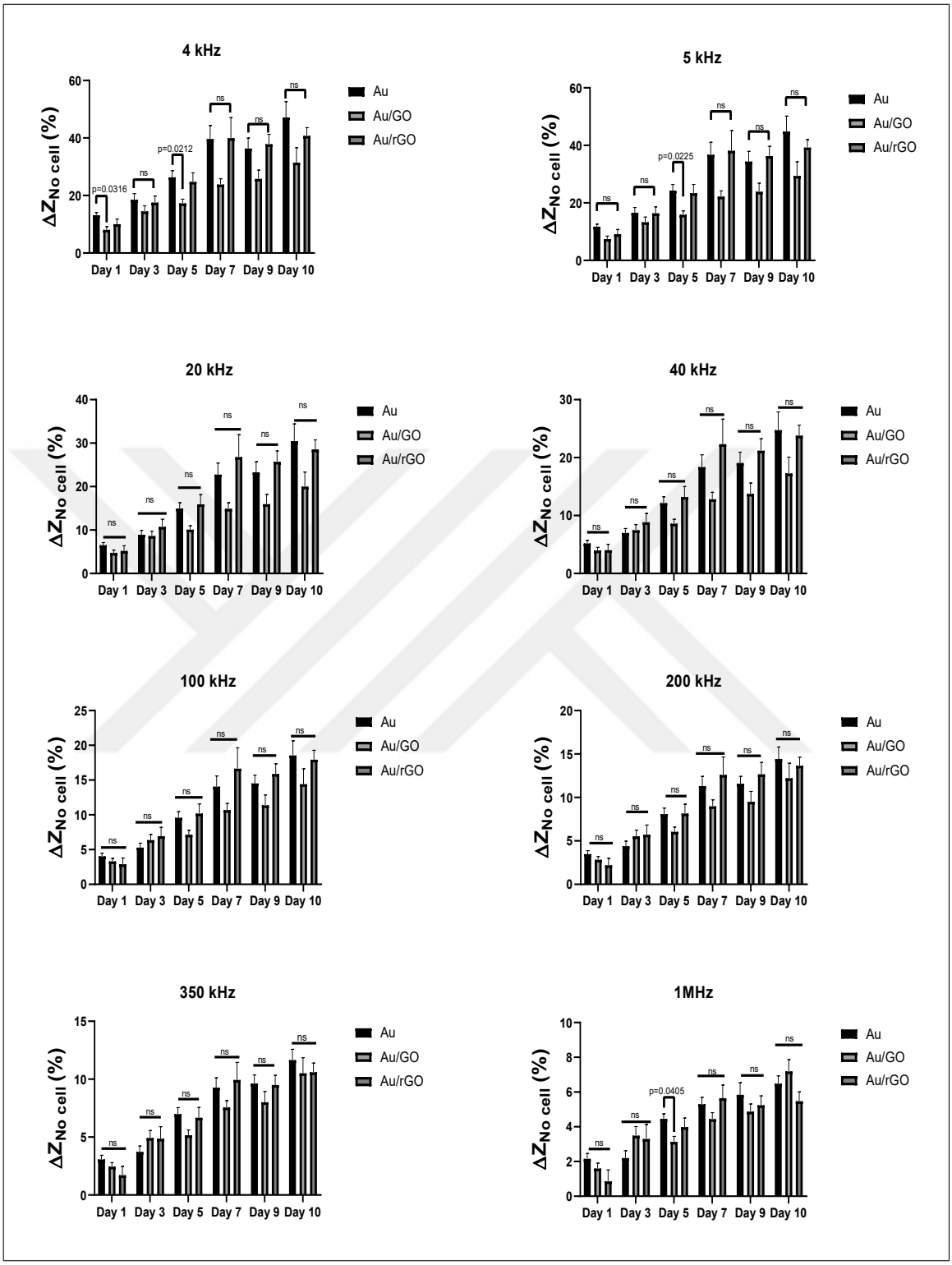

Figure 3.6 Rate of change of impedance with respect to cell medium (ΔZ_{NoCell} (%)) for each type of electrode surfaces Au, Au/GO and Au/rGO; at 4 kHZ, 5 kHz, 20 kHz, 40 kHz, 200 kHz, 350 kHz and 1 MHz. Data presented show mean ± SEM (n= 12); p values are shown according to the Kruskal-Wallis and Dunn's test post hoc test and all other remaining pairwise comparisons are non-significant.

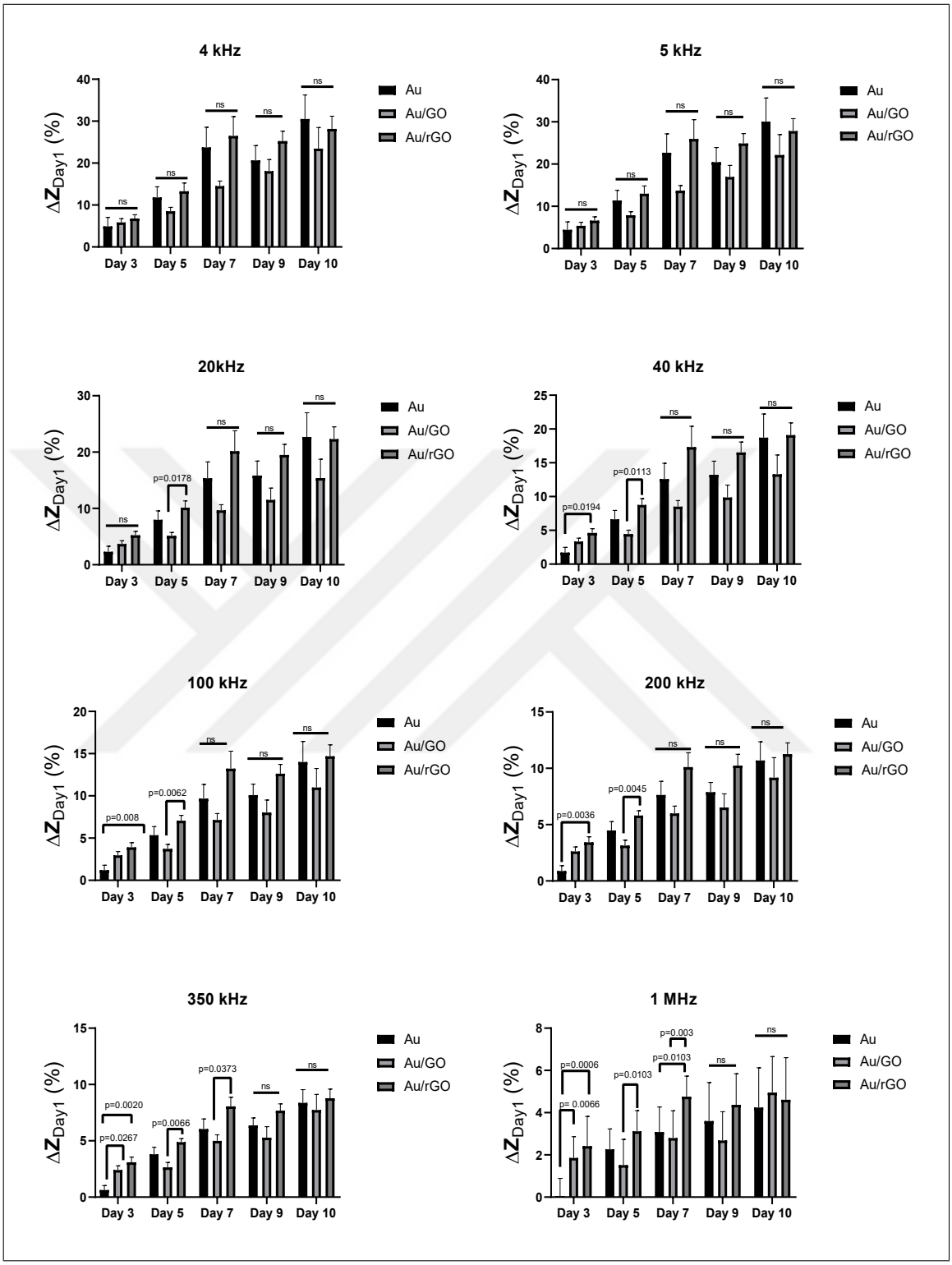

Figure 3.7 Rate of change of impedance change rates with respect to (ΔZ_{Day1} (%)) for each type of electrode surfaces Au, Au/GO and Au/rGO; at 4 kHZ, 5 kHz, 20 kHz, 40 kHz, 200 kHz, 350 kHz and 1 MHz. Data presented show mean ± SEM (n=12); p values are shown according to the Kruskal-Wallis and Dunn's test post hoc test and all other remaining pairwise comparisons are non-significant.

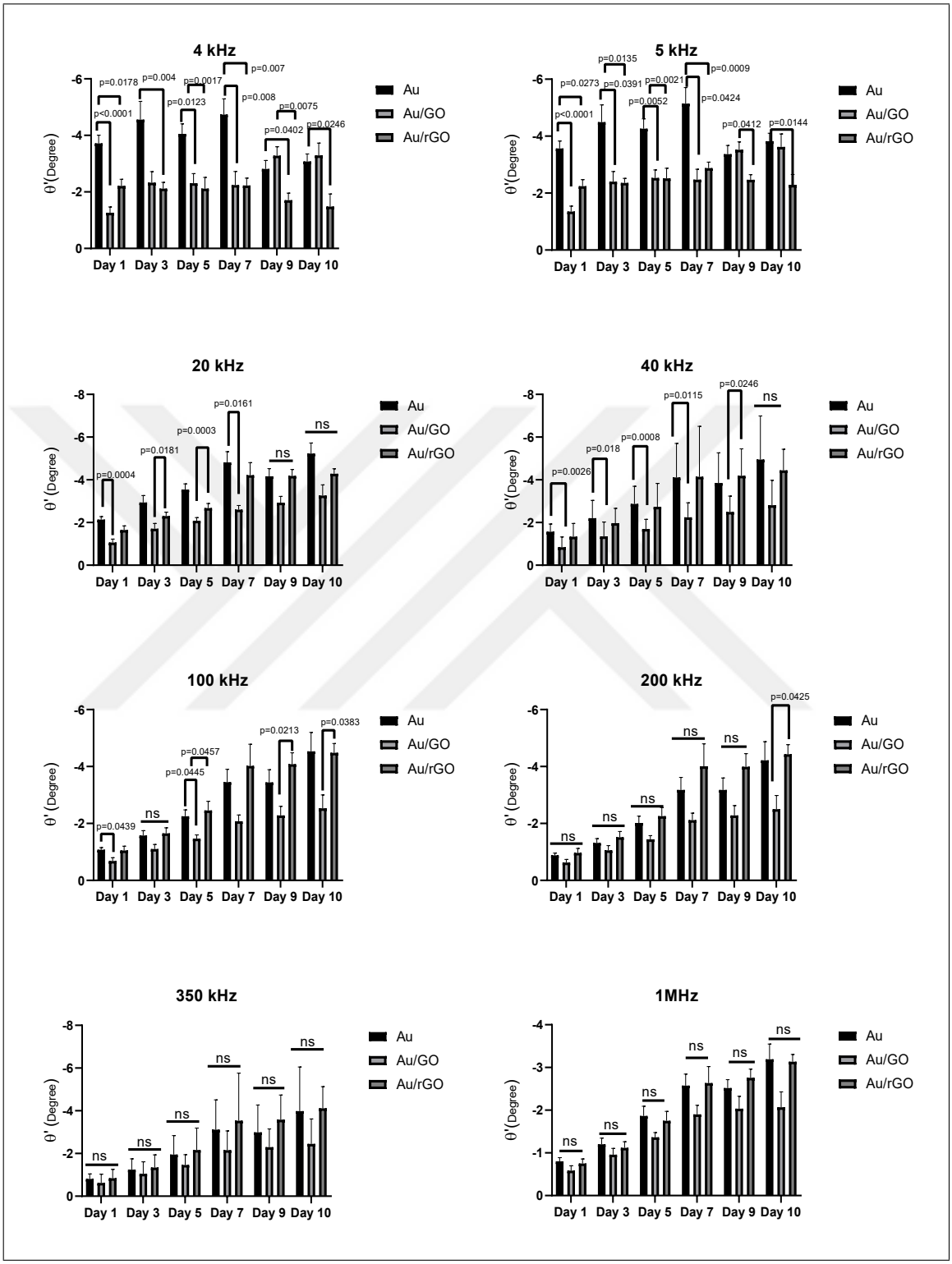

Figure 3.8 Corrected phase angles for each type electrode surfaces Au, Au/GO and Au/rGO at 4 kHZ, 5 kHz, 20 kHz, 40 kHz, 200 kHz, 350 kHz and 1 MHz. Data presented show mean ± SEM (n= 12); p values are shown according to the Kruskal-Wallis and Dunn's test post hoc test, all other remaining pairwise comparisons are non-significant.

3.2.2 Cell counting

Optical images of cells throughout the experiment, taken by Nikon Eclipse LV500 microscope and Hirox 3D digital microscope KH-8700. The cell counts were performed through the images. ImageJ software was used for manual counting of cells. The images were obtained on Day 1, Day 3, Day 5, Day 7 and Day 10, as presented in Figures 3.9, 3.10, 3.11, 3.12 and 3.13 . For each day and for each group, 14 images were analyzed. The cell count analysis is displayed in Figure 3.14: an increase in the population of cells is observed from the 1st day until the 10th day.

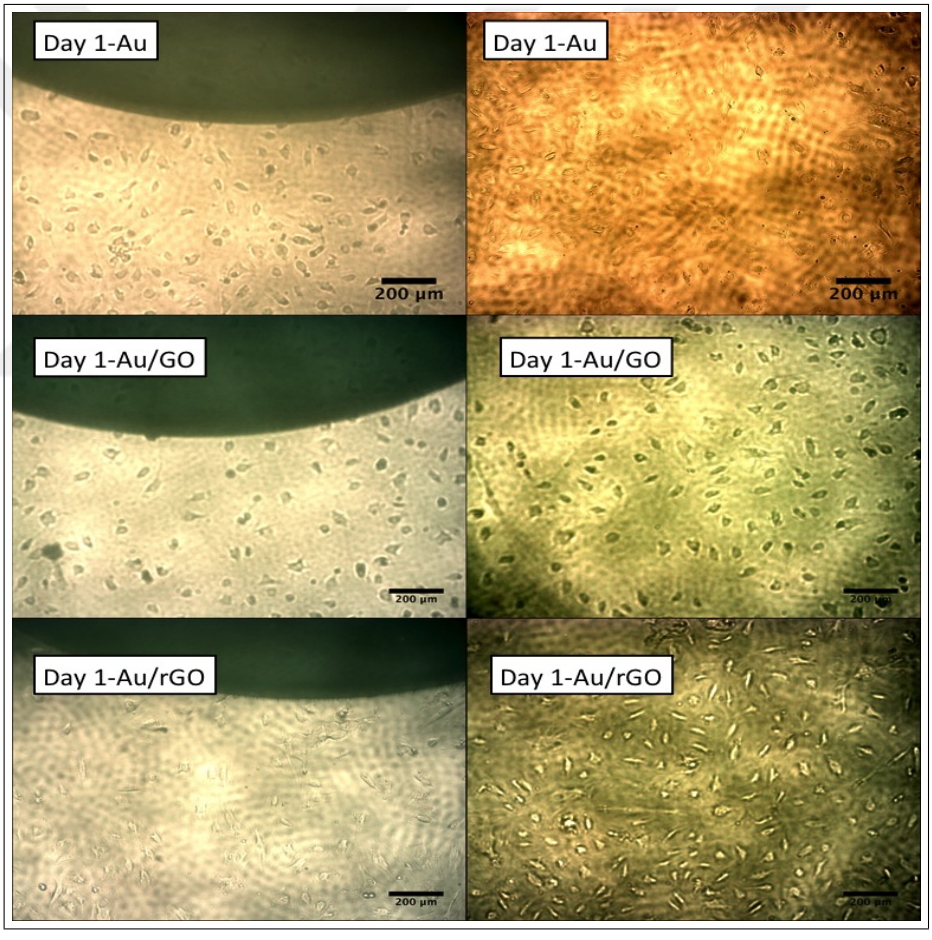

Figure 3.9 Representative optical images taken by Nikon Eclipse LV150 microscope (5X) of HCtAEC from the Au, Au/GO and Au/rGO surfaces on day 1. The images are from the area between the large counter electrode and the small working electrode (left) and from the large counter electrode (right). Scale bars are 100 μm.

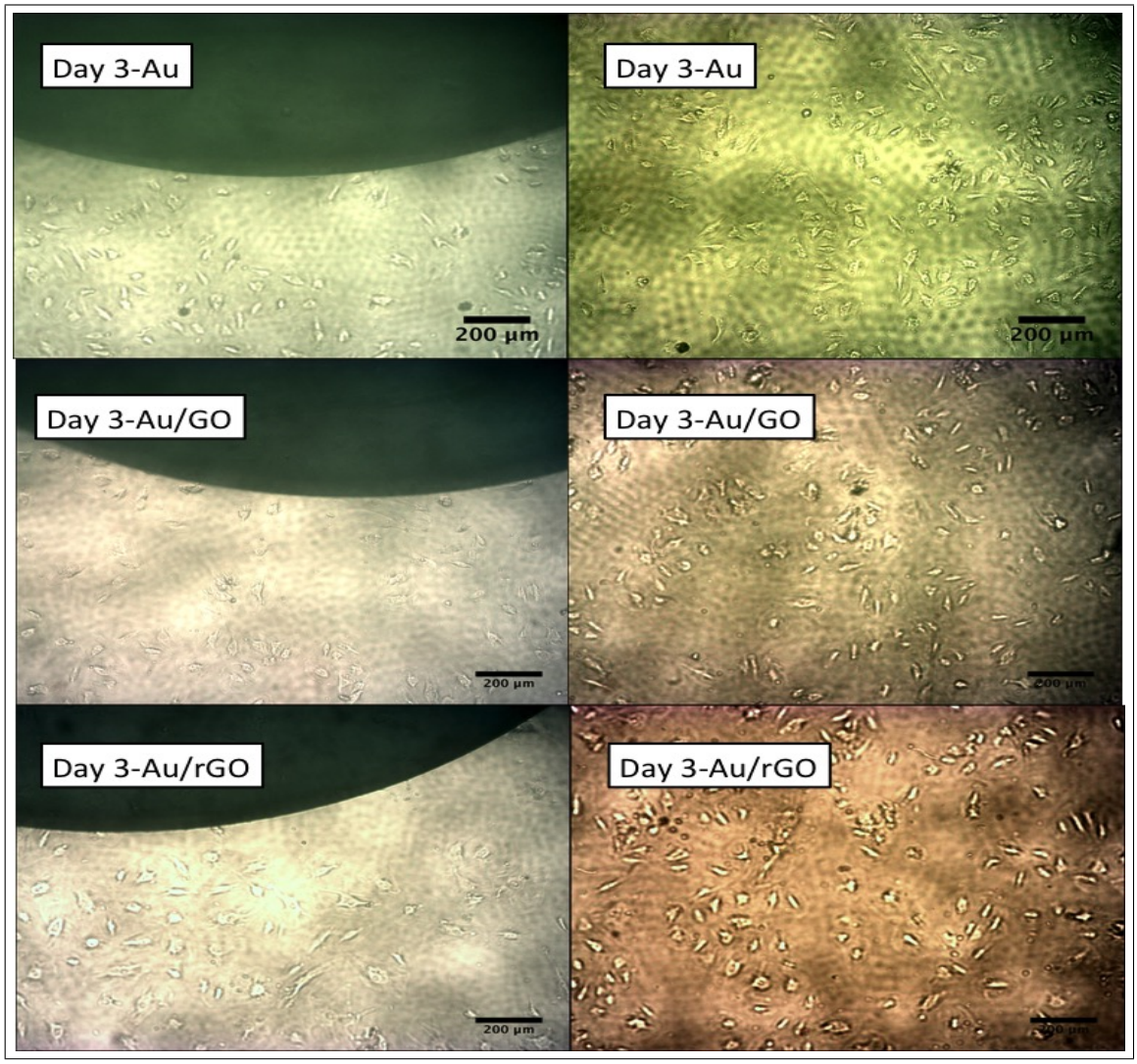

Figure 3.10 Representative optical images taken by Nikon Eclipse LV150 microscope (5X) of HC-tAEC from the Au, Au/GO and Au/rGO surfaces on day 3. The images are from the area between the large counter electrode and the small working electrode (left) and from the large counter electrode (right). Scale bars are 100 μm.

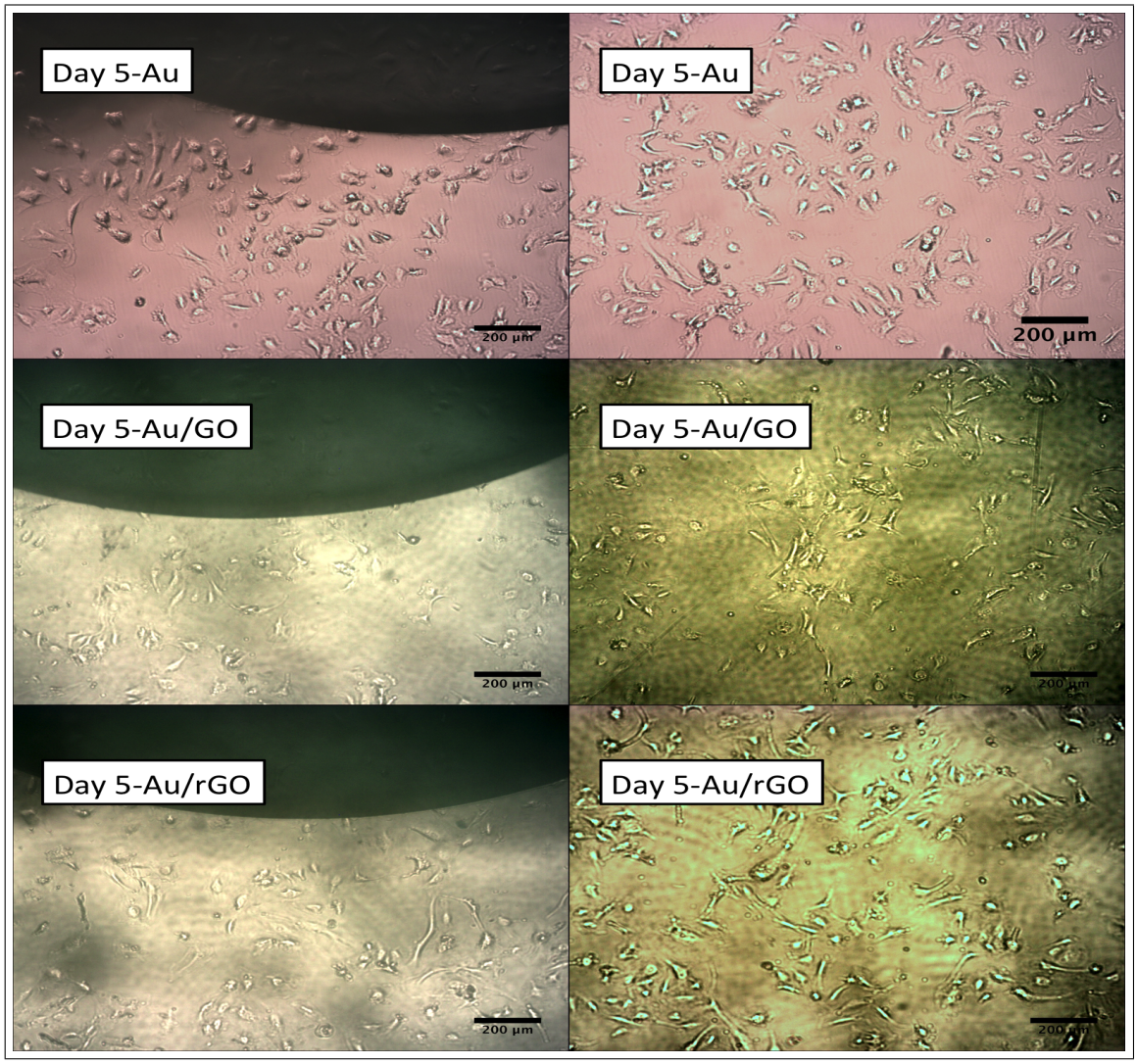

Figure 3.11 Representative optical images taken by Nikon Eclipse LV150 microscope (5X) of HC-tAEC from the Au, Au/GO and Au/rGO surfaces on day 5. The images are from the area between the large counter electrode and the small working electrode (left) and from the large counter electrode (right). Scale bars are 100 μm.

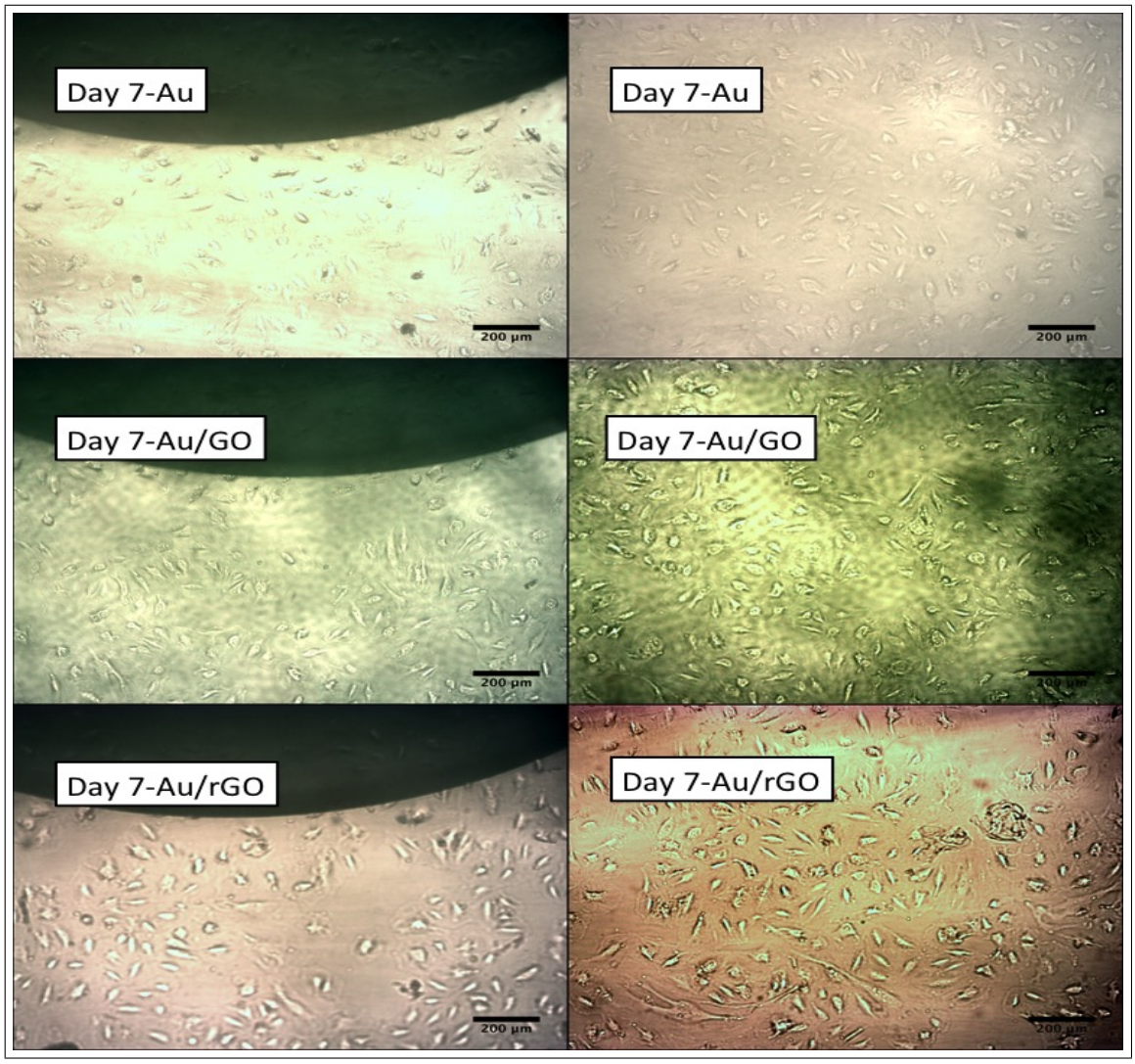

Figure 3.12 Representative optical images taken by Nikon Eclipse LV150 microscope (5X) of HC-tAEC from the Au, Au/GO and Au/rGO surfaces on day 7. The images are from the area between the large counter electrode and the small working electrode (left) and from the large counter electrode (right). Scale bars are 100 μm.

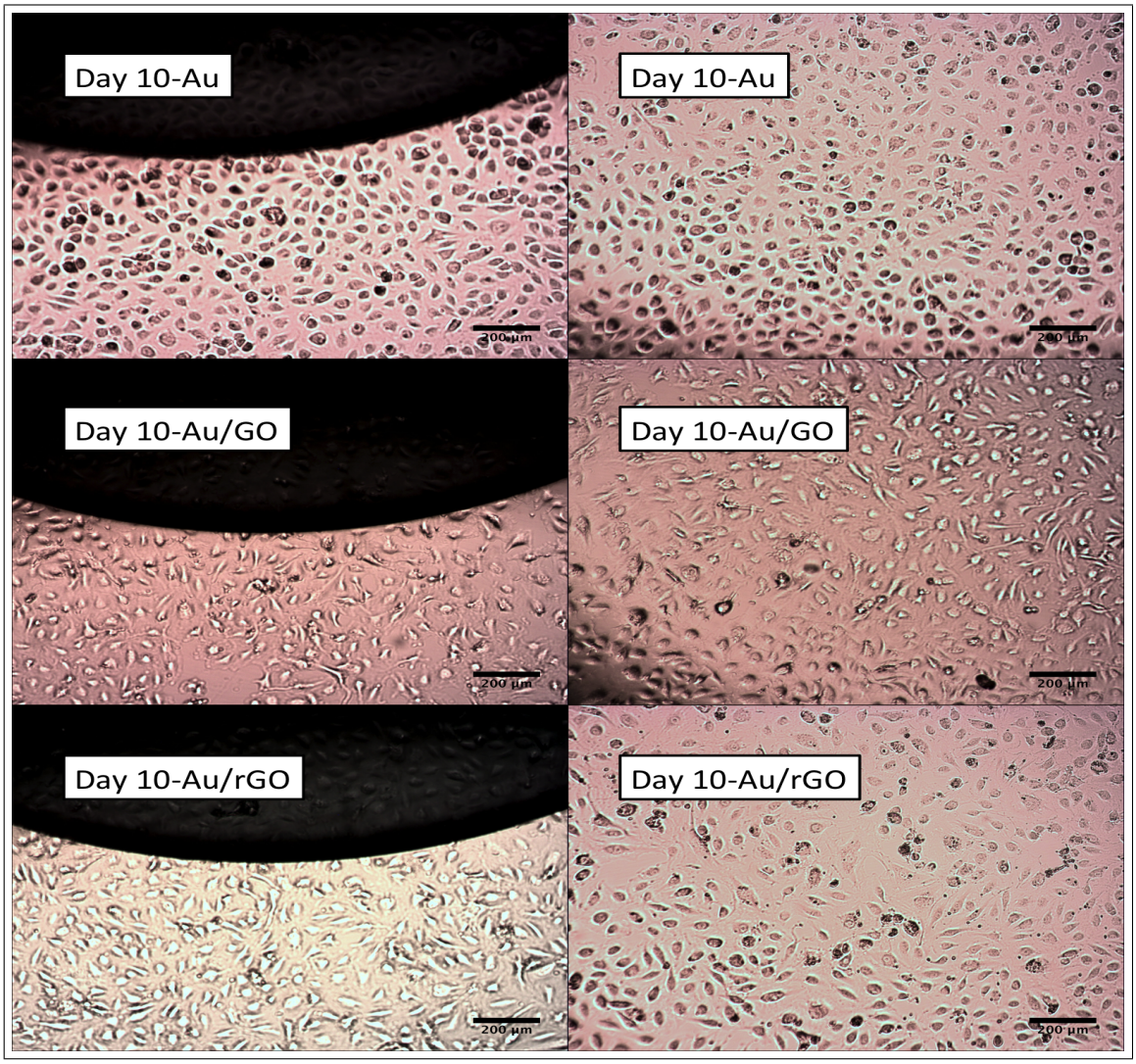

Figure 3.13 Representative optical images taken by Nikon Eclipse LV150 microscope (5X) of HC-tAEC from the Au, Au/GO and Au/rGO surfaces on day 10. The images are from the area between the large counter electrode and the small working electrode (left) and from the large counter electrode (right). Scale bars are 100 μm.

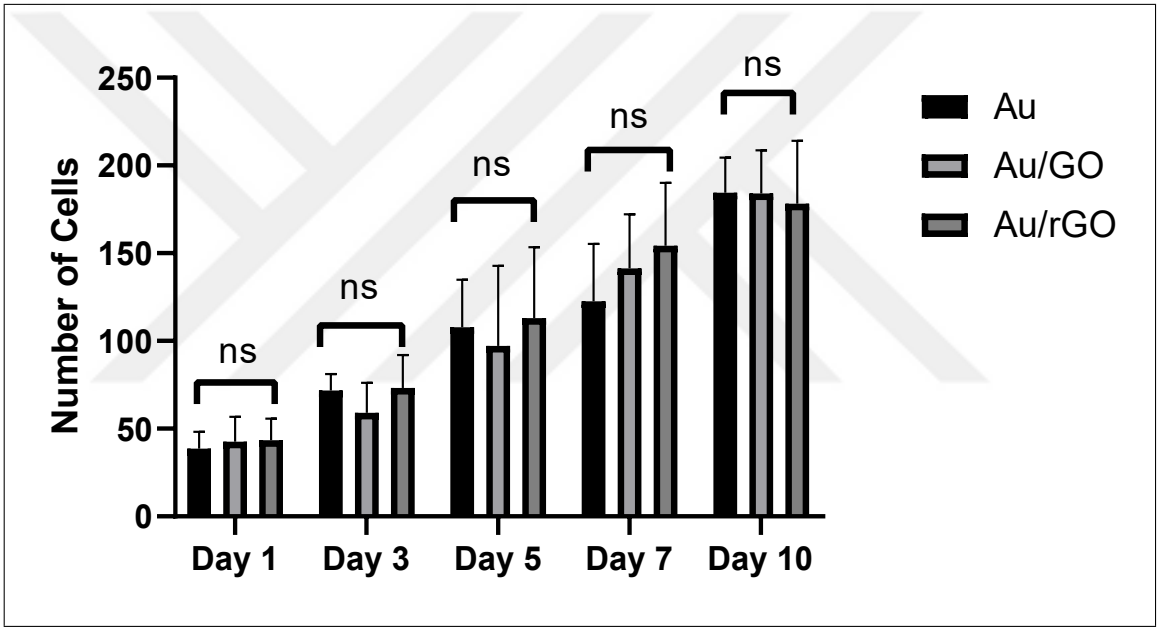

Figure 3.14 Cell counts from 0.01 cm^2 of the smaller electrode surface (n=14). Data show mean ± SD; *p<0.05, ns for non-significant according to the Kruskal-Wallis and Dunn's post hoc test.

3.2.3 Cell Viability Assay

On Day 10, AB assay was performed in order to compare the cell viabilities results on electrode surfaces (Figure 3.15). The test could not be performed on other EIS measurement days because the AB test process, following the EIS measurements, disturb the cells causing the cell detachments due to several PBS washes which must be done during the AB test. Thus, it was preferred to perform the test at the last EIS measurement day, after the EIS measurement. For statistical analysis, non-parametric Kruskal-Wallis, and for multiple comparisons of Au, Au/GO and Au/rGO surfaces, Dunn's test were performed. Test results showed that although the cell viability on Au/GO and Au/rGO surfaces did not significantly differ from each other, Au/rGO surface had significantly higher cell viability rate (p=0.0001) than Au surface.

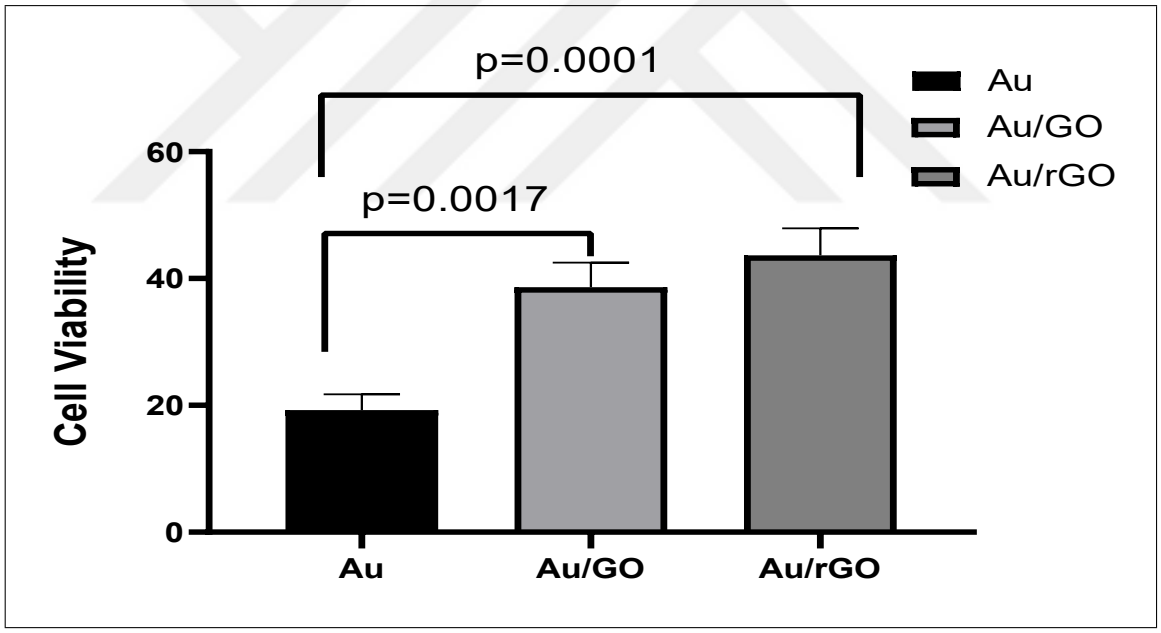

Figure 3.15 AB reduction value for HCAtECs on Au (n=11), Au/GO (n=12) and Au/rGO surface (n=12) on day 10. Bars and error bars show mean ± SD; According to the Kruskal-wallis test and Dunn's test for multiple comparisons, significant difference between Au and Au/GO surface (p=0.0017), significant difference between Au and Au/rGO surface for cell viability (p=0.0001). ns: no significant difference between other groups.

3.2.4 AO/PI Staining

To verify the existence of dead cells on the surfaces, AO/PI staining was performed. 5X10^3 HCAtECs were seeded on the Au, Au/GO, Au/rGO surfaces and the tissue culture well plates. The staining was performed on day 3. The stained cells on the surfaces are shown in Figure 3.16. The green stained cells are the alive cells and the red coloured cells are the dead cells. The alive and dead cells were counted through optical images obtained from at least 3 different locations of the images. The ratio of the living cell number to the sum of alive and dead cells is calculated by the formula: (Live Cells/(Live Cells + Dead Cells)*100, and shown in Figure 3.17.

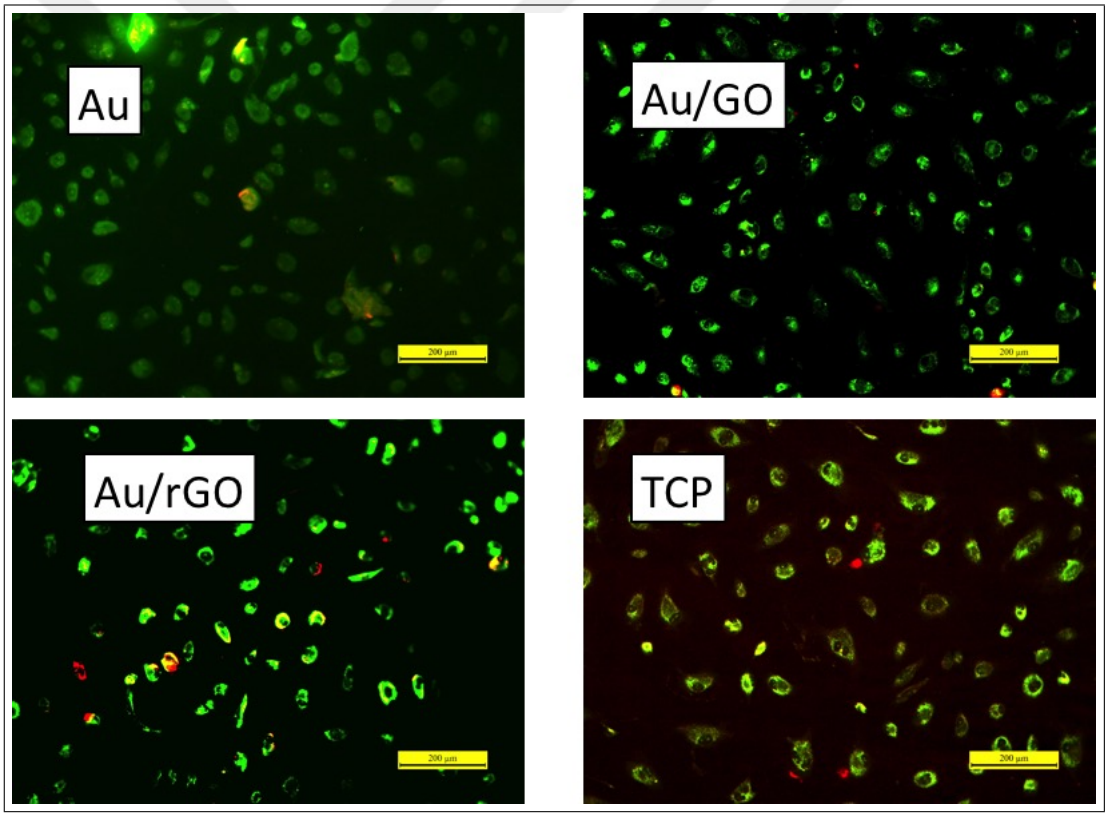

Figure 3.16 Acridine (AO)/Propidium (PI) stained HCAtECs on Au, Au/GO, Au/rGO surfaces and TCP on day 3. The images were obtained by DMIL, Leica florescent microscope. Alive cells are in green and dead cells are in red. Scale bar is 200 μm.

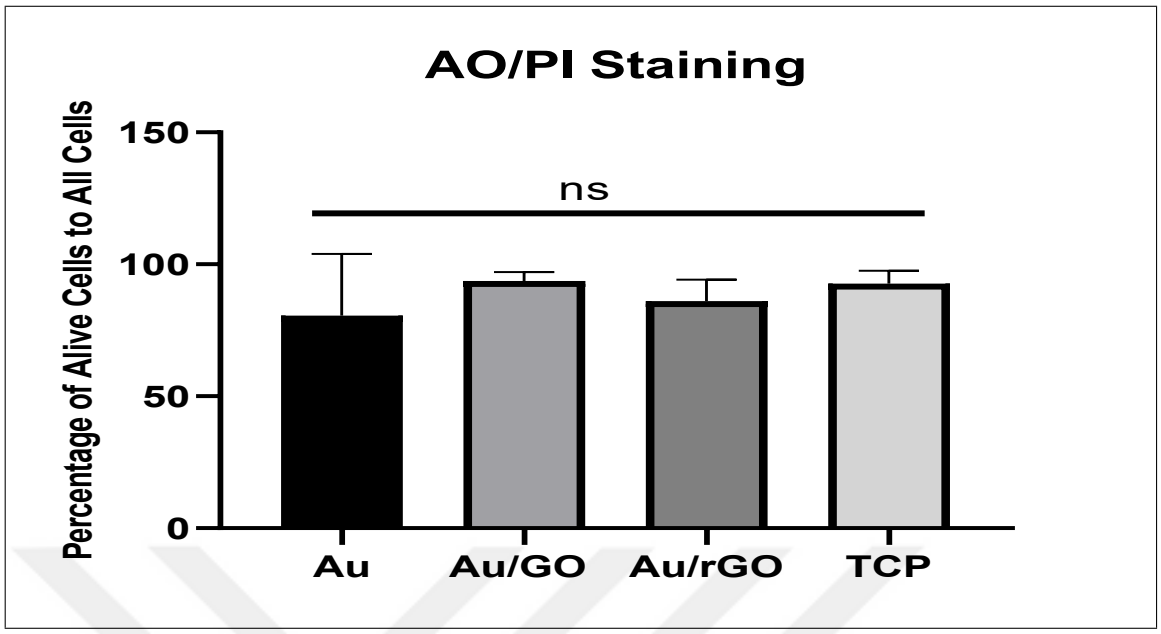

Figure 3.17 The percentage of alive HCAtECs to all HCAtECs calculated through cell counts of the AO/PI stained HCAtECs on day 3 (n=2).

3.2.5 Fluorescent staining for nuclei and F-actin visualization of HCtAECs

In order to confirm cell confluency and reveal cell morphology DAPI and F-action staining were performed. In Figure 3.18 the actin filaments (green) and cell nuclei (blue) were visualized. The morphology and the confluency of the cells seems to be similar to each other for Au, Au/GO and Au/rGO surfaces.

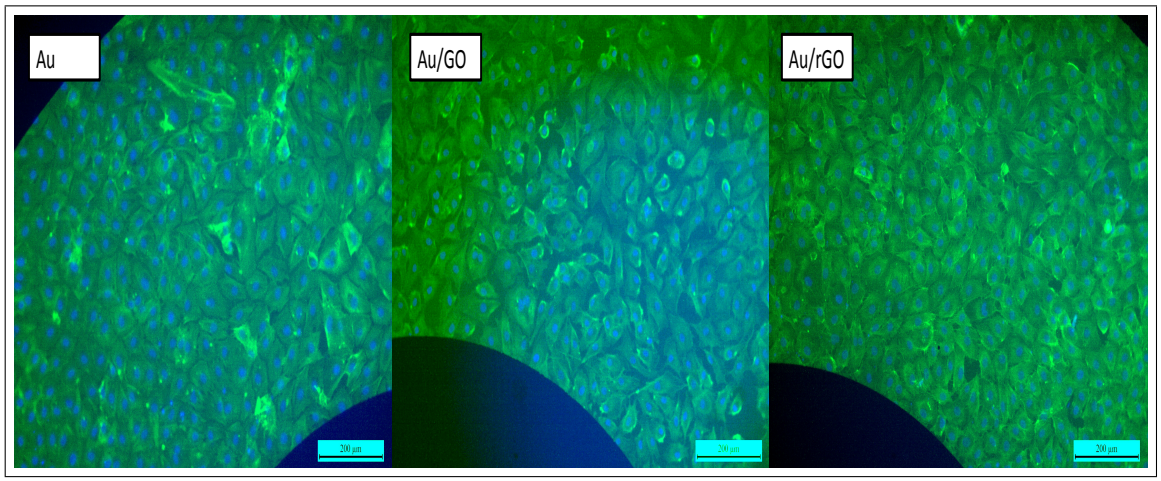

Figure 3.18 DAPI and F-actin staining for HCAtECs on Au, Au/GO and Au/rGO surfaces. The nuclei (blue) stained by DAPI and the filaments (green) by F-actin. Scale bar represents 200 μm.

3.3 Discussion

In this chapter, the methodology and results for the electrical, optical and biochemical analysis for the proliferation of the HCtAECs seeded on Au, Au/GO and Au/rGO electrodes were presented. The electrical analyses were performed by EIS; optical analyses were performed through optical images; for biochemical cell viability analyses, Alamar Blue assay was performed. Immunostaining of the cells such as F-actin, DAPI were performed for assuring cell morphology on the surfaces. AO/PI staining were performed with the aim of quantifying cell death rates on the Au, Au/GO and Au/rGO surfaces. In order to distinguish the cell proliferation rates and cell viability between surfaces, statistical analysis were performed for electrical measurements, cell counts, cell viability assay and AO/PI staining. EIS results showed that, as previous studies suggested, cell adhesion and cell proliferation on the electrode surfaces cause the increase in measured Z by blocking the current flow [92, 116, 117]. This increase in impedance with cell proliferation from day 1 to day 10 was observed in all three Au, Au/GO and Au/rGO surfaces. The magnitude of the phase angle decreased as the frequency increased for medium only (No Cell), day 1, day 3, day 5, day 7, day 9 and day 10. At higher frequencies, the membranes start to permit current flow because the capacitive reactance decreases as the signal frequency increases. The electrical contribution of cell proliferation on phase angle was that, as the cell proliferated on the electrode surfaces, the magnitude of phase angle decreased in the 100 Hz-1kHz range whereas it increased between frequencies 1 kHz-1 MHz (Figure 3.5). Since the cell membrane acts as a capacitor, as the cell number increases on the electrodes, it can be said that the number of capacitors on the current pathway increases. At lower frequencies up to 1 kHz, the current had difficulty for passing through these capacitor; thus increasing the number of cells, phase angle magnitude decreased. The increase in phase angle magnitude at higher frequencies with cell proliferation may be due to the decrease in inter-cellular gap. The decrease in gaps between cells hinders current flow through these pathways, resulting increase in measured impedance. The resistance of the cell mono-layer increases, dominating the signal. Likewise, the calculated capacitive reactance from measured Z and Θ was getting larger in magnitude with increasing cell number at all frequency range (Figure 3.4).

Statistical analysis were performed for frequencies 4 kHz, 5 kHZ, 20 kHz, 40 kHz, 100 kHz, 200 kHz, 350 kHz and 1 MHz. Between these frequencies, only at 4 kHz, 5 kHz and 1 MHz frequencies, significant difference between the impedance change rates with respect to medium only ΔZ_{NoCell} (%), i.e, normalized impedance with respect to cell culture medium, were detected. The rate of impedance change on day 1 was larger for Au surface than the AU/GO surface at 4 kHz (p=0.0316). The reason of this difference may stem from the cell adhesion properties of the surfaces. Au surface may be more available for cell adherence than the Au/GO surface. However the impedance change rate with respect to cell medium also vanished on day 3 at these frequencies. On day 3, there was no significant difference in ΔZ_{NoCell} (%) between the surfaces. However, later on day 5, ΔZ_{NoCell} (%) became larger in Au electrode than Au/GO electrode at 4 kHz (p=0.212), 5 kHz (p=0.225), and at 1 MHz (p=0.0405) . For other selected frequencies, there was no statistically significant difference between the surfaces for all measurement days. Statistical tests for impedance change rates with respect to Day 1 (ΔZ_{Day1} (%)) were also performed. Although the analysis of impedance with respect to cell culturing day other than the cell medium is uncommon, the calculations of commercial ECIS analyzer for cell monitoring includes normalization functions with respect to any chosen day for cell culture period. In order to eliminate the possible variations in the cell seeding process, ΔZ_{Day1} (%) was tested for statistical analyses. The frequencies chosen for tests were same in those of ΔZ_{NoCell} (%). At 4 kHZ and 5 kHz there were not any detectable difference between surfaces. On day 3, the value of for Au/rGO was significantly larger than that of Au at 40 kHz (p=0.0194), at 100 kHz (p=0.0080), at 200 kHz (p=0.0036), at 350 kHz (p=0.0020) and at 1 MHz (p=0.006). This means that, on day 3, for frequencies above 40 kHz, the impedance change from day 1 was larger for cells proliferating on rGO compared to those of the gold surfaces. On day 3, the Au/GO surface had also statistically significant larger nominal values for ΔZ_{Day1} (%) than that of the Au surface at 350 kHz (p=0.0267) and at 1 MHz (0.0066). It can be said that at the first measurement day when the cell adhesion occurred recently, gold surface had larger impedance increase than the graphene related material. However GO and rGO increased the number of cells more rapidly. In other words, in the possibility of Au surface had superior adhesion property than the GO and rGO, the latter ones increased the number of cells faster after the

adhesion. On day 5, at all of the selected frequencies, besides 4 kHz and 5 kHz, ΔZ_{Day1} (%) of Au/rGO was significantly larger than that of Au/GO. This behaviour continued on day 7 at frequencies 350 kHz and 1 MHz. This showed that Au/rGO surface had larger impedance contribution with proliferating adherent cells. These differences vanished on Day 10. The corrected phase angle (Θ') was larger in Au than Au/rGO at 4 kHz at all experimental days and at 5 kHz at all experimental days but day 9. Au surface had also significantly larger Θ' value than Au/GO until day 9. This tendency continued at 20 kHz, 40 kHz and 100 kHz. Frequencies over 100 kHz, at 200 kHz, 350 kHz and 1 Mz Θ' value became similar for all surfaces at all experimental days, except that at day 10 Au/rGO had larger Θ' value than that of Au/GO. Although at frequencies of 4 kHz and 5 kHz, Θ' was smaller in Au/rGO than that of Au/GO; this changed oppositely at frequencies above 20 kHz.

In order to compare impedance rate of change with respect to cell proliferation days, ΔZ_{NoCell} (%) was analyzed in terms of its magnitude. From Day 1 to Day 10, the mean value of ΔZ_{NoCell} (%) increased at all measured and analyzed frequencies. ΔZ_{Day1} (%) increased from 3.06 % (day 1) to 11.64 (day 10) % on the Au electrode surface; from 2.44 % (Day 1) to 10.51 % (Day 10) on the Au/GO electrode surface, from 1.70 % (Day 1) to 10.59 % (Day 10) on Au/rGO surface at 350 kHz. The rate of increase in impedance change from day 1 to day 10 was nearly five-fold for all electrode surfaces. At 4 kHz, ΔZ_{NoCell} (%) increased from 13.10 % (day 1) to 47.12 % for Au, from 8.06 % to 31.42 for Au/GO, 10.04 % to 40.71 % for Au/rGO. The normalized impedance value with respect to cell medium increased to nearly four times on day 10 at 4 kHz. At the last experimental day, when the cells reached confluency (the confluency was also verified by immunostaining Figure 3.18). Impedance change rates form "No Cell" and "Day 1" were not significantly different from each other for all electrode surfaces at day 10. However Au/GO had lowest nominal values (Figures 2.1, 3.1). The impedance phase angle (Θ) had changing trend with frequency. At lower frequencies, phase angle decreased with the cell proliferation day, i.e, as the cell number increased on the electrode surfaces. On the other hand at frequencies above 1 kHz, Θ value increased as the cell number increased (Figure 3.5). This was consistent with previous studies in the literature [4, 94]. Sun et al measured smaller

phase angle value with cells than without cells [4]. Nguyen et al showed that cell apoptosis increased the phase angle at lower frequencies and decreased it at higher frequencies above [94]. Corrected phase angle value (Θ') also increases with increasing cell number on the electrodes. Although there was a critical frequency point that the phase angle response changed, the magnitude of the reactance of the capacitance calculated through measured Z and phase angle value increased with increase in number of cells. This may stem from the capacitive behavior of the biological cells, especially cell-membrane, increasing in number resulted in higher capacitance [117]. Non-faradaic EIS studies in the literature generally utilizes bare gold electrode as sensor. There are very rare examples for graphene and/or graphene related materials integrated in the sensory surface for non-faradaic measurements. In a faradaic EIS, there are examples of graphene-based materials as a biosensor; the increase in sensitivity with GO/poly-L-lysine complex for the detection of leukemia cancer cell line [109], increased sensitivity for protein detection [118]. However, there are a few studies for non-faradaic cell impedance measurements through graphene interfaces. The very few examples showed its applicability. RGO coated gold electrodes were used sensing of human embryonic kidney cells by EIS and the cell adherence was detectable [119]. Chinnadayyala et al coated rGO-Au nanoparticles on Indium Tin Oxide (ITO) electrodes and used the resulting sensor for EIS measurement of HEK293 during cell culture [106]. Their results revealed the bio-compatibility of rGO and the increased measurement range with rGO-Au nano particle complex compared to bare, gold nano particle or rGO deposited on indium tin oxide. The measurement range comparison was interpreted from the saturation level of the normalized impedance. In another interesting and very recent study, a three dimensional graphene interface designed for single cancer cell detection. The three dimensional graphene interface was more sensitive than the two dimensional gold interface [112].

In this thesis, rather than the detection of single cell, electrical measurements were performed to obtain cell proliferation rates. Thus the availability of graphene derivatives for cell proliferation monitoring was checked, rather than the lowest detection limit. The results revealed that graphene derivatives did not negatively affect the electrical measurement quality. All electrode surfaces in the study; Au, Au/GO and

Au/rGO were available for electrically monitoring HCtAEC proliferation. In addition to the lack of negative affect, rGO, having larger nominal impedance values than GO.

As mentioned in chapter 1, there are contradictory results in the literature about the toxicity of graphene related materials. It was said in chapter 1 that the interference of graphene with cells and the concentration level of graphene molecules determine the toxicity. The other factors can be listed as flake size, treatment time and type of cell line. Recently, Gies et al declared that although the effect of flake size on toxicity of graphene was unclear, suspension cells showed lower cell viability results compared to the adherent cells [120]. Comparing the toxicity of GO and rgO, Das et al found that rGO was less toxic than the GO to human umbilical vascular endothelial cells [73]. In this thesis, the bio-compatibility of graphene coatings for HCtAECs was tested for the first time.

Although there were electrically detected differences in surfaces, according to cell count analysis there was no detectable significant difference between surfaces. Cell count analysis was performed through the optical cell images (Figure 3.14) starting from day 1 to day 10. In electrical response, the signal consists of not only cell number but also cell-to-cell distance, cell-substrate gap, the permeability of the cell membrane, the size of the cells. Thus the cell number contribution is not the only signal that is monitored in electrical impedance. This fact may be the reason that although cell numbers were similar to each other for all surfaces, the electrical characteristics of the cells differed from each other.

For cell viability analysis, AB assay was performed. The AB reagent reduction level indicates the cell viability, the higher the value means the higher cell viability rate. The cell viability rate was significantly lower in Au electrode than Au/rGO electrode. Although WCA results of Au surfaces were similar to Au/rGO surfaces, the cell viability rate was not similar to each other for these two surface. On the other hand, Au/GO surface being more hydrophilic than Au/rGO; their cell viability results were similar to each other. It can be concluded that rather than the surface hydrophobicity, graphene functional groups maintained cell viability. Results support

the previous findings that the functional mechanism of graphene derivatives may be the cause of significant enhancement of cell viability [72,121]. In immunostaining by DAPI and F-action on day 10, showed that cell confluency had been reached at all surfaces. The fine structures of the filaments for each surface type were visualized [122]. There seems to be a slightly increased gap at Au/GO surface compared to Au and Au/rGO (Figure 3.18). AO/PI staining on day 3 showed that the graphene coatings did not show toxicity to HCAtECs since the number of dead cells at all surfaces were similar to tissue culture plate (Figure 3.16).

4. CONCLUSION AND FUTURE WORK

In this study, EIS technique was utilized in cell behaviour monitoring. Photolithography and plasma enhanced chemical vapor deposition techniques were utilized in order to produce surface gold electrodes. The gold surfaces were coated with GO by the self assembly method. rGO on gold surfaces were obtained through hydrazine vapor reduction. Surface characterizations were performed visually by SEM, electrically by EIS. Surface hyrophobicity and hydrophilicity were measured through water contact angle measurements. The results of characterization methods showed that the surface coatings were achieved.

HCtAEC cell proliferation on Au, Au/GO and Au/rGO surfaces was monitored through EIS, optical images, AB assay and immunostaining. The results showed the availability and applicability of graphene derivatives for HCtAEC proliferation. RGO had the highest AB reduction value of 43.65 ± 8.79 %. Since rGO coatings accelerated endothelialization and provide potential for enhancing carotid stent bio-compatibility, the thesis suggests that rGO can be utilized for coating carotid artery stent endothelialization.

As further work, more detailed electrical modeling of data should be performed with diversity of biological assays. The paralleling of the electrical data with biological assays would increase the model for interpreting the functional mechanisms. In addition to that, micro-fluidic platforms should be integrated to the system in order to mimic the real arterial structure. The implementation of EIS sensor on stent surface and monitoring the stent biocompatibility are the further aspects of the study.

To precisely control negative or positive effects of graphene derivatives to endothelial cells, varying the concentration levels of graphene in coating processes should be done.

APPENDIX A. EXAMINING GRAPHENE FLAKES FOR PROCESSES BY SEM

To clean the surfaces from graphene flakes ultrasonication and O_2 plasma treatment were performed. The parameters for O_2 plasma was; radio frequency power of 200 watt, O_2 flow rate was 100 cm^3/min, process pressure of 300 mTorr and duration was 60 seconds. Ultrasonication was performed for 5 min in ultrasonic bath. GO flakes remained intact after ultrasonication. However O_2 plasma application removed all of the flakes (Figure A.1). Additionally, the stability of the flakes after cell culture study was checked. Neither the UV irradiation nor the cell seeding and proliferation caused visible damage of the flakes (Figure A.2).

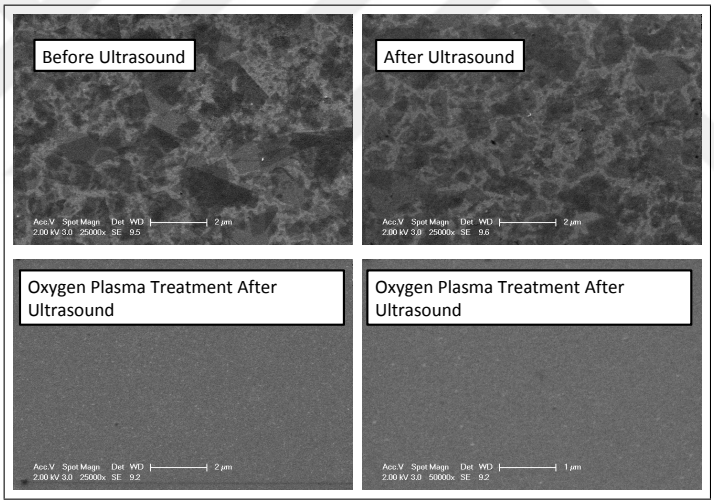

Figure A.1 Treatment of graphene on gold surfaces by ultrasonication and oxygen plasma treatment.

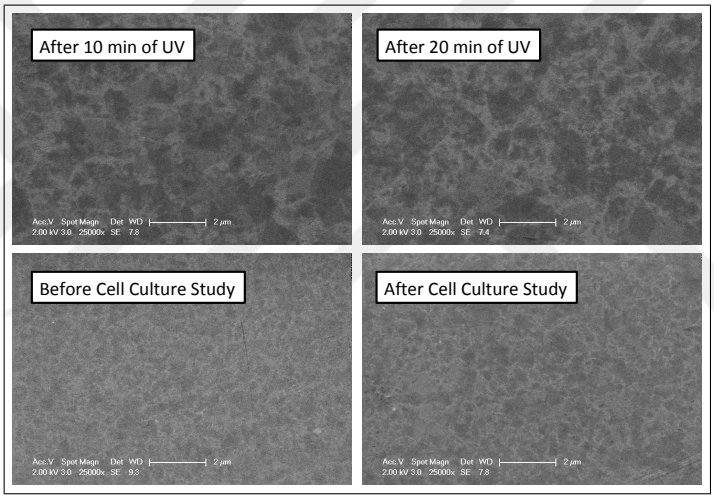

Figure A.2 Graphene before and after sterilization for 10 min of UV light (up). Graphene before and after the cell culture seeding (bottom).

REFERENCES

1. Anatomy, "Blood vessels- the cardiovascular system." `https://sites.google.com/site/theheartanatomyproject2012/blood-vessels`, Last accessed on 2020-07-05.

2. Cell Applications, "Human Endothelial Cells." `https://www.cellapplications.com`, Last accessed on 2020-05-15.

3. Castro Neto, A. H., F. Guinea, N. M. Peres, K. S. Novoselov, and A. K. Geim, "The electronic properties of graphene," *Reviews of Modern Physics*, Vol. 81, no. 1, pp. 109–162, 2009.

4. Sun, T., E. J. Swindle, J. E. Collins, J. A. Holloway, D. E. Davies, and H. Morgan, "On-chip epithelial barrier function assays using electrical impedance spectroscopy," *Lab on a Chip*, Vol. 10, no. 12, pp. 1611–1617, 2010.

5. Cho, S., and H. Thielecke, "Electrical characterization of human mesenchymal stem cell growth on microelectrode," *Microelectronic Engineering*, Vol. 85, no. 5-6, pp. 1272–1274, 2008.

6. Wegener, J., M. Sieber, and H. J. Galla, "Impedance analysis of epithelial and endothelial cell monolayers cultured on gold surfaces," *Journal of Biochemical and Biophysical Methods*, Vol. 32, no. 3, pp. 151–170, 1996.

7. Goda, N., N. Kataoka, and J. Shimizu, "Evaluation micromotion of vascular endothelial cells with estrogen in electrical cell-substrate impedance sensing (ECIS) method using a mathematical model cell-to-cell distance," in *Proceedings of the 3rd Annual International IEEE EMBS Special Topic*, no. May, pp. 211–214, 2005.

8. Wang, L., H. Wang, L. Wang, K. Mitchelson, Z. Yu, and J. Cheng, "Analysis of the sensitivity and frequency characteristics of coplanar electrical cell-substrate impedance sensors," *Biosensors and Bioelectronics*, Vol. 24, no. 1, pp. 14–21, 2008.

9. Zhang, F., T. Jin, Q. Hu, and P. He, "Distinguishing skin cancer cells and normal cells using electrical impedance spectroscopy," *Journal of Electroanalytical Chemistry*, Vol. 823, no. 2017, pp. 531–536, 2018.

10. Hong, J. L., K. C. Lan, and L. S. Jang, "Electrical characteristics analysis of various cancer cells using a microfluidic device based on single-cell impedance measurement," *Sensors and Actuators, B: Chemical*, Vol. 173, pp. 927–934, 2012.

11. Simsek, F., O. M. Can, B. Garipcan, Ö. Kocatürk, and Y. Ülgen, "Characterization of carotid endothelial cell proliferation on Au , Au / GO , and Au / rGO surfaces by electrical impedance spectroscopy," *Medical & Biological Engineering & Computing*, 2020.

12. Lee, J. S., J. C. Yoon, and J. H. Jang, "A route towards superhydrophobic graphene surfaces: Surface-treated reduced graphene oxide spheres," *Journal of Materials Chemistry A*, Vol. 1, no. 25, pp. 7312–7315, 2013.

13. Kakinoki, S., K. Takasaki, A. Mahara, T. Ehashi, Y. Hirano, and T. Yamaoka, "Direct surface modification of metallic biomaterials via tyrosine oxidation aiming to accelerate the re-endothelialization of vascular stents," *Journal of Biomedical Materials Research - Part A*, Vol. 106, no. 2, pp. 491–499, 2018.

14. Mendis, S., Puska, P., Norrving, B., *Global Atlas On Cardiovascular Disease Prevention And Control*, Geneva: World Health Organization, first ed., 2011.

15. T.C. Sağlık Bakanlığı, "Türkiye Kalp ve Damar Hastalıklarını Önleme ve Kontrol Programı Birincil , İkincil ve Üçüncül Korumaya Yönelik Stratejik Plan ve Eylem Planı," tech. rep., T.C. Sağlık Bakanlığı, Temel Sağlık Hizmetleri Genel Müdürlüğü, Ankara, 2010.

16. Holland, I., C. McCormick, and P. Connolly, "Towards non-invasive characterisation of coronary stent re-endothelialisation â An in-vitro, electrical impedance study," *PLoS ONE*, Vol. 13, no. 11, pp. 1–17, 2018.

17. Félétou M, *The Endothelium - NCBI Bookshelf*, CA: Morgan & Claypool Life Sciences, 2011.

18. Thakali, K. M., J. J. Galligan, G. D. Fink, and S. W. Watts, *Arterial and Venous Function in Hypertension*, Elsevier Inc., first edition ed., 2007.

19. Brown, B. A., H. Williams, and S. J. George, *Evidence for the Involvement of Matrix-Degrading Metalloproteinases (MMPs) in Atherosclerosis*, Vol. 147, Elsevier Inc., 1 ed., 2017.

20. Zaromitidou, M., G. Siasos, N. Papageorgiou, E. Oikonomou, and D. Tousoulis, *Atherosclerosis and coronary artery disease: From basics to genetics*, Elsevier Inc., 2016.

21. Rajendran, P., T. Rengarajan, J. Thangavel, Y. Nishigaki, D. Sakthisekaran, G. Sethi, and I. Nishigaki, "The vascular endothelium and human diseases," *International Journal of Biological Sciences*, Vol. 9, pp. 1057–1069, Nov 2013.

22. Aird, W. C., "Endothelium," *Consultative Hemostasis and Thrombosis: Third Edition*, pp. 33–41, 2013.

23. Gimbrone, M. A., and G. García-Cardeña, "Endothelial Cell Dysfunction and the Pathobiology of Atherosclerosis," *Circulation Research*, Vol. 118, no. 4, pp. 620–636, 2016.

24. Sun, H. J., Z. Y. Wu, X. W. Nie, and J. S. Bian, "Role of endothelial dysfunction in cardiovascular diseases: The link between inflammation and hydrogen sulfide," *Frontiers in Pharmacology*, Vol. 10, no. Jan, pp. 1–15, 2020.

25. Davis, N. E., "Atherosclerosis- An Inflammatory Process," *Journal of Insurance Medicine*, Vol. 37, pp. 72–75, 2005.

26. Rebagay, G., and S. Bangalore, "Biodegradable Polymers and Stents: the Next Generation?," *Current Cardiovascular Risk Reports*, Vol. 13, Aug 2019.

27. Tan, C. H., N. Muhamad, and M. M. Abdullah, "Surface Topographical Modification of Coronary Stent: A Review," *IOP Conference Series: Materials Science and Engineering*, Vol. 209, no. 1, 2017.

28. Shahryari, A., F. Azari, H. Vali, and S. Omanovic, "The response of fibrinogen, platelets, endothelial and smooth muscle cells to an electrochemically modified SS316LS surface: Towards the enhanced biocompatibility of coronary stents," *Acta Biomaterialia*, Vol. 6, no. 2, pp. 695–701, 2010.

29. Cheng, H.-Y., W.-T. Hsiao, L.-H. Lin, Y.-J. Hsu, A. W. Sinrang, and K.-L. Ou, "Effects of antibacterial nanostructured composite films on vascular stents: Hemodynamic behaviors, microstructural characteristics, and biomechanical properties.," *Journal of Biomedical Materials Research. Part A*, mar 2014.

30. O'Brien, B., J. Stinson, and W. Carroll, "Initial exploration of Ti-Ta, Ti-Ta-Ir and Ti-Ir alloys: Candidate materials for coronary stents.," *Acta Biomaterialia*, Vol. 4, pp. 1553–9, Sep 2008.

31. Morton, A. C., D. Crossman, and J. Gunn, "The influence of physical stent parameters upon restenosis," *Pathologie Biologie*, Vol. 52, pp. 196–205, 2004.

32. He, D., W. Liu, and T. Zhang, "The Development of Carotid Stent Material," *Interventional Neurology*, Vol. 3, no. 2, pp. 67–77, 2014.

33. Qi, P., S. Chen, T. Liu, J. Chen, Z. Yang, Y. Weng, J. Chen, J. Wang, F. Manfred, and N. Huang, "New strategies for developing cardiovascular stent surfaces with novel functions," *Biointerphases*, Vol. 9, no. 029017, pp. 1–14, 2014.

34. Ali, M., M. Elsherif, A. E. Salih, A. Ul-Hamid, M. A. Hussein, S. Park, A. K. Yetisen, and H. Butt, "Surface modification and cytotoxicity of Mg-based bio-alloys: An overview of recent advances," *Journal of Alloys and Compounds*, Vol. 825, p. 154140, jun 2020.

35. Bedair, T. M., M. A. ElNaggar, Y. K. Joung, and D. K. Han, "Recent advances to accelerate re-endothelialization for vascular stents," *Journal of Tissue Engineering*, Vol. 8, 2016.

36. Lee, S. J., H. H. Jo, K. S. Lim, D. Lim, S. Lee, J. H. Lee, W. D. Kim, M. H. Jeong, J. Y. Lim, I. K. Kwon, Y. Jung, J. K. Park, and S. A. Park, "Heparin coating on 3D printed poly (l-lactic acid) biodegradable cardiovascular stent via mild surface modification approach for coronary artery implantation," *Chemical Engineering Journal*, Vol. 378, p. 122116, Dec 2019.

37. Kuczyńska-Zemła, D., E. Kijeńska-Gawrońska, M. Pisarek, P. Borowicz, W. Swieszkowski, and H. Garbacz, "Effect of laser functionalization of titanium on bioactivity and biological response," *Applied Surface Science*, p. 146492, Apr 2020.

38. Chen, C., Y. Xiong, W. Jiang, Y. Wang, Z. Wang, and Y. Chen, "Experimental and Numerical Simulation of Biodegradable Stents with Different Strut Geometries," *Cardiovascular Engineering and Technology*, Vol. 11, pp. 36–46, feb 2020.

39. Simon, C., J. C. Palmaz, and E. A. Sprague, "Influence of topography on endothelialization of stents: Clues for new designs," *Journal of Long-Term Effects of Medical Implants*, Vol. 10, no. 1-2, pp. 143–151, 2000.

40. Park, S. Y., J. B. Choi, and S. Kim, "Measurement of cell-substrate impedance and characterization of cancer cell growth kinetics with mathematical model," *International Journal of Precision Engineering and Manufacturing*, Vol. 16, no. 8, pp. 1859–1866, 2015.

41. Cardenas, L., J. MacLeod, J. Lipton-Duffin, D. G. Seifu, F. Popescu, M. Siaj, D. Mantovani, and F. Rosei, "Reduced graphene oxide growth on 316L stainless steel for medical applications.," *Nanoscale*, Vol. 6, pp. 8664–70, Aug 2014.

42. Ge, S., Y. Xi, R. Du, Y. Ren, Z. Xu, Y. Tan, Y. Wang, T. Yin, and G. Wang, "Inhibition of in-stent restenosis after graphene oxide double-layer drug coating with good biocompatibility," *Regenerative Biomaterials*, pp. 1–11, mar 2019.

43. Podila, R., T. Moore, F. Alexis, and A. M. Rao, "Graphene coatings for enhanced hemocompatibility of nitinol stents," *RSC Adv.*, Vol. 3, no. 6, pp. 1660–1665, 2013.

44. Chung, D. D., "Review: Graphite," *Journal of Materials Science*, Vol. 37, no. 8, pp. 1475–1489, 2002.

45. Bai, L., Y. Zhang, W. Tong, L. Sun, H. Huang, Q. An, N. Tian, and P. K. Chu, "Graphene for Energy Storage and Conversion: Synthesis and Interdisciplinary Applications," *Electrochemical Energy Reviews*, pp. 1–36, Apr 2019.

46. Banerjee, J., K. Dutta, and D. Rana, "Carbon Nanomaterials in Renewable Energy Production and Storage Applications," pp. 51–104, Springer, Cham, 2019.

47. Dheer, L., S. Bhattacharjee, S. C. Lee, and U. V. Waghmare, "Van der Waals heterostructures of 1H-MoS2 and N-substituted graphene for catalysis of hydrogen evolution reaction," *Materials Research Express*, Vol. 6, no. 12, pp. 2–9, 2019.

48. Jeon, I.-Y., M. J. Ju, J. Xu, H.-J. Choi, J.-M. Seo, M.-J. Kim, I. T. Choi, H. M. Kim, J. C. Kim, J.-J. Lee, H. K. Liu, H. K. Kim, S. Dou, L. Dai, and J.-B. Baek, "Edge-Fluorinated Graphene Nanoplatelets as High Performance Electrodes for Dye-Sensitized Solar Cells and Lithium Ion Batteries," *Advanced Functional Materials*, Vol. 25, pp. 1170–1179, feb 2015.

49. Messina, R., and P. Ben-Abdallah, "Graphene-based photovoltaic cells for near-field thermal energy conversion," *Scientific Reports*, Vol. 3, pp. 1–5, mar 2013.

50. Wu, Q., G. Zhao, C. Feng, C. Wang, and Z. Wang, "Preparation of a graphene-based magnetic nanocomposite for the extraction of carbamate pesticides from environmental water samples," *Journal of Chromatography A*, Vol. 1218, pp. 7936–7942, Nov 2011.

51. Song, S., H. Shen, Y. Wang, X. Chu, J. Xie, N. Zhou, and J. Shen, "Biomedical application of graphene: From drug delivery, tumor therapy, to theranostics," *Colloids and Surfaces B: Biointerfaces*, Vol. 185, no. Nov, p. 110596, 2019.

52. Depan, D., J. Shah, and R. D. Misra, "Controlled release of drug from folate-decorated and graphene mediated drug delivery system: Synthesis, loading efficiency, and drug release response," *Materials Science and Engineering C*, Vol. 31, pp. 1305–1312, oct 2011.

53. Wu, X., S. Tan, Y. Xing, Q. Pu, M. Wu, and J. X. Zhao, "Graphene oxide as an efficient antimicrobial nanomaterial for eradicating multi-drug resistant bacteria in vitro and in vivo," *Colloids and Surfaces B: Biointerfaces*, Vol. 157, pp. 1–9, Sep 2017.

54. Chen, Y. W., Y. L. Su, S. H. Hu, and S. Y. Chen, "Functionalized graphene nanocomposites for enhancing photothermal therapy in tumor treatment," *Advanced Drug Delivery Reviews*, Vol. 105, pp. 190–204, oct 2016.

55. Zhou, H., C. Cheng, H. Qin, L. Ma, C. He, S. Nie, X. Zhang, Q. Fu, and C. Zhao, "Self-assembled 3D biocompatible and bioactive layer at the macro-interface via graphene-based supermolecules," *Polymer Chemistry*, Vol. 5, pp. 3563–3575, jun 2014.

56. Pan, C. J., L. Q. Pang, F. Gao, Y. N. Wang, T. Liu, W. Ye, and Y. H. Hou, "Anti-coagulation and endothelial cell behaviors of heparin-loaded graphene oxide coating on titanium surface," *Materials Science and Engineering C*, Vol. 63, pp. 333–340, 2016.

57. Toda, K., R. Furue, and S. Hayami, "Recent progress in applications of graphene oxide for gas sensing: A review," *Elsevier B.V.*, 2015.

58. Compton, O. C., and S. T. Nguyen, "Graphene Oxide , Highly Reduced Graphene Oxide , and Graphene : Versatile Building Blocks for Carbon-Based Materials," *Small*, Vol. 6, no. 6, pp. 711–723, 2010.

59. Smith, A. T., A. M. LaChance, S. Zeng, B. Liu, and L. Sun, "Synthesis, properties, and applications of graphene oxide/reduced graphene oxide and their nanocomposites," *Nano Materials Science*, Vol. 1, no. 1, pp. 31–47, 2019.

60. Karlický, F., K. Kumara Ramanatha Datta, M. Otyepka, and R. Zboril, "Halogenated graphenes: Rapidly growing family of graphene derivatives," *ACS Nano*, Vol. 7, no. 8, pp. 6434–6464, 2013.

61. Huang, X., X. Qi, F. Boey, and H. Zhang, "Graphene-based composites," *Chemical Society Reviews*, Vol. 41, no. 2, pp. 666–686, 2012.

62. Choi, W., and C. G. Rocha, "Tailoring the Physical Properties of Graphene," *Graphene*, pp. 16–41, 2018.

63. Bhuyan, M. S. A., M. N. Uddin, M. M. Islam, F. A. Bipasha, and S. S. Hossain, "Synthesis of graphene," *International Nano Letters*, Vol. 6, no. 2, pp. 65–83, 2016.

64. Edwards, R. S., and K. S. Coleman, "Graphene synthesis: Relationship to applications," *Nanoscale*, Vol. 5, no. 1, pp. 38–51, 2013.

65. K. S. Novoselov, A. K. Geim, S. V. Morozov, D. Jiang, Y. Zhang, S. V. Dubonos, I. V. G., and A. A. Firsov, "Electric Field Effect in Atomically Thin Carbon Films," *Science*, Vol. 306, no. 5696, pp. 666–669, 2004.

66. Choi, W., I. Lahiri, R. Seelaboyina, and Y. S. Kang, "Synthesis of graphene and its applications: A review," *Critical Reviews in Solid State and Materials Sciences*, Vol. 35, no. 1, pp. 52–71, 2010.

67. Terrones, M., "Nanotubes unzipped," *Nature*, Vol. 458, pp. 845–846, Apr 2009.

68. Santiago, E. V., S. H. López, M. A. Camacho López, D. R. Contreras, R. Farías-Mancilla, S. G. Flores-Gallardo, C. A. Hernández-Escobar, and E. A. Zaragoza-Contreras, "Optical properties of carbon nanostructures 136 produced by laser irradiation on chemically modified multi-walled carbon nanotubes," *Optics and Laser Technology*, Vol. 84, pp. 53–58, oct 2016.

69. Jiao, L., L. Zhang, X. Wang, G. Diankov, and H. Dai, "Narrow graphene nanoribbons from carbon nanotubes," *Nature*, Vol. 458, pp. 877–880, Apr 2009.

70. Guy, O. J., and K. A. D. Walker, "Graphene Functionalization for Biosensor Applications," in *Silicon Carbide Biotechnology: A Biocompatible Semiconductor for Advanced Biomedical Devices and Applications: Second Edition*, pp. 85–141, Elsevier Inc., mar 2016.

71. Robinson, J. T., F. K. Perkins, E. S. Snow, Z. Wei, and P. E. Sheehan, "Reduced graphene oxide molecular sensors," *Nano Letters*, Vol. 8, no. 10, pp. 3137–3140, 2008.

72. Yun, Y. J., S.-J. Park, J. Seo, Y.-H. Song, D. H. Ha, H.-M. Chung, Y. Jun, and S.-H. Moon, "Cellular organization of three germ layer cells on different types of noncovalent functionalized graphene substrates," *Materials Science and Engineering: C*, Vol. 103, p. 109729, oct 2019.

73. Das, S., S. Singh, V. Singh, D. Joung, J. M. Dowding, D. Reid, J. Anderson, L. Zhai, S. I. Khondaker, W. T. Self, and S. Seal, "Oxygenated functional group density on graphene oxide: Its effect on cell toxicity," *Particle and Particle Systems Characterization*, Vol. 30, no. 2, pp. 148–157, 2013.

74. Lim, M. H., I. C. Jeung, J. Jeong, S. J. Yoon, S. H. Lee, J. Park, Y. S. Kang, H. Lee, Y. J. Park, H. G. Lee, S. J. Lee, B. S. Han, N. W. Song, S. C. Lee, J. S. Kim, K. H. Bae, and J. K. Min, "Graphene oxide induces apoptotic cell death in endothelial cells by activating autophagy via calcium-dependent phosphorylation of c-Jun N-terminal kinases," *Acta Biomaterialia*, Vol. 46, pp. 191–203, 2016.

75. Sasidharan, A., S. Siddharth, P. Chandran, S. Nair, and M. Koyakutty, "Cellular and molecular mechanistic insight in to the DNA damaging potential of few-layer graphene in human primary endothelial cells," *Nanomedicine: Nanotechnology, Biology, and Medicine*, 2016.

76. Cibecchini, G., M. Veronesi, T. Catelani, T. Bandiera, D. Guarnieri, and P. P. Pompa, "Antiangiogenic Effect of Graphene Oxide in Primary Human Endothelial Cells," *ACS Applied Materials & Interfaces*, 2020.

77. Rosas-Hernandez, H., C. Escudero-Lourdes, M. A. Ramirez-Lee, E. Cuevas, S. M. Lantz, S. Z. Imam, W. Majeed, S. E. Bourdo, M. G. Paule, A. S. Biris, and S. F. Ali, "Cytotoxicity profile of pristine graphene on brain microvascular endothelial cells," *Journal of Applied Toxicology*, Vol. 39, no. 7, pp. 966–973, 2019.

78. Price, D., *MEMS And Electrical Impedance Spectroscopy (EIS) For Non-Invasive Measurement Of Cells*, no. 1, Woodhead Publishing Limited, 2012.

79. Xu, Y., X. Xie, Y. Duan, L. Wang, Z. Cheng, and J. Cheng, "A review of impedance measurements of whole cells," *Biosensors and Bioelectronics*, Vol. 77, no. October, pp. 824–836, 2016.

80. Coulter, W. H., "High speed automatic blood cell counter and size analyzer," *Proc Natl Electron Conf*, pp. 1034–1040, 1956.

81. Giaever, I., and C. R. Keese, "Monitoring fibroblast behavior in tissue culture with an applied electric field," *Proceedings of the National Academy of Sciences of the United States of America*, Vol. 81, no. 12, pp. 3761–3764, 1984.

82. Ding, L., D. Du, X. Zhang, and H. Ju, "Trends in Cell-Based Electrochemical Biosensors," *Current Medicinal Chemistry*, Vol. 15, no. 30, pp. 3160–3170, 2008.

83. Dorledo de Faria, R. A., L. G. Dias Heneine, T. Matencio, and Y. Messaddeq, "Faradaic and non-faradaic electrochemical impedance spectroscopy as transduction techniques for sensing applications," *International Journal of Biosensors & Bioelectronics*, Vol. 5, no. 1, pp. 29–31, 2019.

84. Biesheuvel, P. M., and J. E. Dykstra, "The difference between Faradaic and Nonfaradaic processes in Electrochemistry," *Arvix*, pp. 1–10, 2018.

85. Velasco, V., *Repository Microfluidic platform for impedance characterization of endothelial cells under fluid shear stress .* PhD thesis, University of Louisville, 2016.

86. Vetelino, J., and A. Reghu, *Introduction to Sensors*, Bosa Roca, United States: Taylor & Francis Group, 2010.

87. Kanoun, O., *Impedance Spectroscopy:Advanced Applications:Battery Research, Bioimpedance, System Design*, Berlin, Germany: De Gruyter, Inc., 2018.

88. Khalil, S. F., M. S. Mohktar, and F. Ibrahim, "The theory and fundamentals of bioimpedance analysis in clinical status monitoring and diagnosis of diseases," *Sensors (Switzerland)*, Vol. 14, pp. 10895–10928, jun 2014.

89. Amini, M., J. Hisdal, and H. Kalvøy, "Applications of bioimpedance measurement techniques in tissue engineering," *Journal of Electrical Bioimpedance*, Vol. 9, no. 1, pp. 142–158, 2018.

90. Schwan, H. P., "Electrical properties of tissue and cell suspensions.," *Advances in biological and medical physics*, Vol. 5, pp. 147–209, 1957.

91. Grimnes, S., and Ø. G. Martinsen, "Alpha-dispersion in human tissue," *Journal of Physics: Conference Series*, Vol. 224, no. 1, pp. 1–4, 2010.

92. Giaever, I., and C. R. Keese, "Micromotion of mammalian cells measured electrically.," *Proceedings of the National Academy of Sciences of the United States of America*, Vol. 88, no. 17, pp. 7896–7900, 1991.

93. Qiu, Y., R. Liao, and X. Zhang, "Real-time monitoring primary cardiomyocyte adhesion based on electrochemical impedance spectroscopy and electrical cell-substrate impedance sensing," *Analytical Chemistry*, Vol. 80, no. 4, pp. 990–996, 2008.

94. Anh-Nguyen, T., B. Tiberius, U. Pliquett, and G. A. Urban, "An impedance biosensor for monitoring cancer cell attachment, spreading and drug-induced apoptosis," *Sensors and Actuators, A: Physical*, Vol. 241, pp. 231–237, 2015.

95. Rahman, A. R. A., C. M. Lo, and S. Bhansali, "A detailed model for high-frequency impedance characterization of ovarian cancer epithelial cell layer using ECIS electrodes," *IEEE Transactions on Biomedical Engineering*, Vol. 56, no. 2, pp. 485–492, 2009.

96. Boler, M., "Chapter 18," in *Introduction to Classical and New Testament Greek*, Vol. 17, pp. 145–152, 2020.

97. King, D. E., "Oxidation of gold by ultraviolet light and ozone at 25 °C," *Journal of Vacuum Science & Technology A: Vacuum, Surfaces, and Films*, Vol. 13, no. 3, pp. 1247–1253, 1995.

98. Ron, H., S. Matlis, and I. Rubinstein, "Self-assembled monolayers on oxidized metals. 2. Gold surface oxidative pretreatment, monolayer properties, and depression formation," *Langmuir*, Vol. 14, no. 5, pp. 1116–1121, 1998.

99. Woodward, J. T., M. L. Walker, C. W. Meuse, D. J. Vanderah, G. E. Poirier, and A. L. Plant, "Effect of an oxidized gold substrate on alkanethiol self-assembly," *Langmuir*, Vol. 16, no. 12, pp. 5347–5353, 2000.

100. Slaughter, G. E., and R. Hobson, "An impedimetric biosensor based on PC 12 cells for the monitoring of exogenous agents.," *Biosensors & bioelectronics*, Vol. 24, pp. 1153–8, Jan 2009.

101. Xu, C., R.-s. Yuan, and X. Wang, "Selective reduction of graphene oxide," *New Carbon Materials*, Vol. 29, no. 1, pp. 61–66, 2014.

102. Zou, Z., J. Kai, M. J. Rust, J. Han, and C. H. Ahn, "Functionalized nano interdigitated electrodes arrays on polymer with integrated microfluidics for direct bio-affinity sensing using impedimetric measurement," *Sensors and Actuators A: Physical*, Vol. 136, pp. 518–526, may 2007.

103. Yu, H. Z., J. W. Zhao, Y. Q. Wang, S. M. Cai, and Z. F. Liu, "Fabricating an azobenzene self-assembled monolayer via step-by-step surface modification of a cysteamine monolayer on gold," *Journal of Electroanalytical Chemistry*, Vol. 438, no. 1-2, pp. 221–224, 1997.

104. Xu, Q., H. Cheng, J. Lehr, A. V. Patil, and J. J. Davis, "Graphene Oxide Interfaces in Serum Based Autoantibody Quantification," *Analytical Chemistry*, Vol. 87, pp. 346–350, 2015.

105. Rezaei, B., E. Havakeshian, and A. A. Ensafi, "Stainless steel modified with an aminosilane layer and gold nanoparticles as a novel disposable substrate for impedimetric immunosensors," *Biosensors and Bioelectronics*, Vol. 48, pp. 61–66, 2013.

106. Chinnadayyala, S. R., J. Park, M. A. Abbasi, and S. Cho, "Label-free electrochemical impedimetric immunosensor for sensitive detection of IgM rheumatoid factor in human serum," *Biosensors and Bioelectronics*, Vol. 143, no. Aug, p. 111642, 2019.

107. Zong, X., N. Kong, J. Liu, W. Yang, M. Cao, and J. J. Gooding, "The Influence of Graphene on the Electrical Communication Through Organic Layers on Graphite and Gold Electrodes," *Electroanalysis*, Vol. 26, pp. 84–92, Jan 2014.

108. Lanche, R., L. E. Delle, M. Weil, X. T. Vu, V. Pachauri, W. M. Munief, P. Wagner, and S. Ingebrandt, "Routine fabrication of reduced graphene oxide microarray devices via all solution processing," *Physica Status Solidi (A) Applications and Materials Science*, Vol. 210, no. 5, pp. 968–974, 2013.

109. Zhang, D., Y. Zhang, L. Zheng, Y. Zhan, and L. He, "Graphene oxide/poly-L-lysine assembled layer for adhesion and electrochemical impedance detection of leukemia K562 cancer cells.," *Biosensors & bioelectronics*, Vol. 42, pp. 112–8, Apr 2013.

110. Lai, Y. T., Y. S. Chu, J. C. Lo, Y. H. Hung, and C. M. Lo, "Effects of electrode diameter on the detection sensitivity and frequency characteristics of electric cell-substrate impedance sensing," *Sensors and Actuators, B: Chemical*, Vol. 288, no. October 2018, pp. 707–715, 2019.

111. Pradhan, R., M. Mandal, A. Mitra, and S. Das, "Monitoring cellular activities of cancer cells using impedance sensing devices," *Sensors and Actuators, B: Chemical*, Vol. 193, pp. 478–483, 2014.

112. Wang, X., A. Liu, Y. Xing, H. Duan, W. Xu, Q. Zhou, H. Wu, C. Chen, and B. Chen, "Three-dimensional graphene biointerface with extremely high sensitivity to single cancer cell monitoring," *Biosensors and Bioelectronics*, Vol. 105, no. 928, pp. 22–28, 2018.

113. Cell Applications, "HCtAEC | Human Carotid Artery Endothelial Cells | Quality Primary Cells | Cell Applications." https://www.cellapplications.com/human-carotid-artery-endothelial-cells-hctaec, Last accessed on 2020-05-15.

114. Thermo Fisher Scientific, "Actin Staining Protocol." https://www.thermofisher.com/tr/en/home/references/protocols/cell-and-tissue-analysis/microscopy-protocol/actin-staining-protocol.html, Last accessed on 2020-02-13.

115. Thermo Fisher Scientific, "Dapi Staining Protocol." https://www.thermofisher.com/tr/en/home/references/protocols/cell-and-tissue-analysis/protocols/dapi-imaging-protocol.html, Last accessed on 2020-02-13.

116. Wegener, J., C. R. Keese, and I. Giaever, "Electric cell-substrate impedance sensing (ECIS) as a noninvasive means to monitor the kinetics of cell spreading to artificial surfaces.," *Experimental Cell Research*, Vol. 259, no. 1, pp. 158–166, 2000.

117. Giaever, I., and C. R. Keese, "A morphological biosensor for mammalian cells," *Nature*, Vol. 366, pp. 591–592, 1993.

118. Kim, K. S., Y. M. Um, J.-R. Jang, W.-S. Choe, and P. J. Yoo, "Highly sensitive reduced graphene oxide impedance sensor harnessing π-stacking interaction mediated direct deposition of protein probes.," *ACS applied materials & interfaces*, Vol. 5, pp. 3591–8, may 2013.

119. Lanche, R., V. Pachauri, D. Koppenhöfer, P. Wagner, and S. Ingebrandt, "Reduced graphene oxide-based sensing platform for electric cell-substrate impedance sensing," *Physica Status Solidi (a)*, Vol. 211, pp. 1404–1409, jun 2014.

120. Gies, V., and S. Zou, "Systematic toxicity investigation of graphene oxide: Evaluation of assay selection, cell type, exposure period and flake size," *Toxicology Research*, Vol. 7, no. 1, pp. 93–101, 2018.

121. Arima, Y., and H. Iwata, "Effect of wettability and surface functional groups on protein adsorption and cell adhesion using well-defined mixed self-assembled monolayers," *Biomaterials*, Vol. 28, no. 20, pp. 3074–3082, 2007.

122. Paszek, E., J. Czyz, O. Woźnicka, D. Jakubiak, J. Wojnarowicz, W. Łojkowski, and E. Stepień, "Zinc oxide nanoparticles impair the integrity of human umbilical vein endothelial cell monolayer in vitro," *Journal of Biomedical Nanotechnology*, Vol. 8, pp. 957–967, dec.